

AD 748862

A CENTER OF COMPETENCE IN SOLID STATE MATERIALS AND DEVICES

by

Fredrik A. Lindholm, Eugene R. Chenette, Robert W. Gould,
Lorry L. Hench, Sheng S. Li, Aldert van der Ziel



Electrical Engineering Department
College of Engineering
University of Florida
Gainesville, Florida 32601

Contract No. F 19628-68-C-0058

Project No. 8687

Scientific Report No. 9
10 April 1972

Contract Monitor
Andrew C. Yang
Solid State Sciences Laboratory

Approved for public release; distribution unlimited.

Reproduced by
NATIONAL TECHNICAL
INFORMATION SERVICE
U S Department of Commerce
Springfield VA 22151

Sponsored by

Advanced Research Projects Agency
ARPA Order No. 1060

Monitored by

AIR FORCE CAMBRIDGE RESEARCH LABORATORIES
AIR FORCE SYSTEMS COMMAND
UNITED STATES AIR FORCE
BEDFORD, MASSACHUSETTS 01730



**BEST
AVAILABLE COPY**

Program Code No. ID10
 Effective Date of Contract 11 September 1967
 Contract Expiration Date 31 August 1972
 Principal Investigator and Phone No. Dr. Fredrik A. Lindholm/904 392-0904
 Project Scientist and phone no. Dr. Andrew C. Yang/617 861-2225

| | |
|---|---|
| ACCESSION for | |
| NTIS <input checked="" type="checkbox"/> SECRET | White Section <input checked="" type="checkbox"/> |
| DOC <input checked="" type="checkbox"/> SECRET | Buff Section <input type="checkbox"/> |
| UNANNOUNCED | <input type="checkbox"/> |
| JUSTIFICATION | |
| by | |
| DISTRIBUTION/AVAILABILITY CODES | |
| DISC: <input type="checkbox"/> SECRET <input type="checkbox"/> SECRET | |
| A | |

Qualified requestors may obtain additional copies from the
 Defense Documentation Center. All others should apply to the
 National Technical Information Service.

DOCUMENT CONTROL DATA - R&D

(Security classification of title, body of abstract and indexing annotation must be entered when the overall report is classified)

1. ORIGINATING ACTIVITY (Corporate author)

University of Florida
Engineering and Industrial Experiment Station
Gainesville, Florida 32601

2a. REPORT SECURITY CLASSIFICATION
Unclassified

2b. GROUP

3. REPORT TITLE

A CENTER OF COMPETENCE IN SOLID STATE MATERIALS AND DEVICES

4. DESCRIPTIVE NOTES (Type of report and inclusive dates)

Scientific Interim

5. AUTHOR(S) (First name, middle initial, last name)

Fredrik A. Lindholm Larry L. Hench
Eugene R. Chenette Sheng S. Li
Robert W. Gould Aldert van der Ziel

6. REPORT DATE

10 April 1972

7a. TOTAL NO. OF PAGES

184

7b. NO. OF REFS

134

8a. CONTRACT OR GRANT NO.

F 19628-68-C-0058 ARPA Order No. 1060

9a. ORIGINATOR'S REPORT NUMBER(S)

Scientific Report No. 9

9b. OTHER REPORT NO(S) (Any other numbers that may be assigned this report)

AFCRL-72- 0336

b. PROJECT, TASK, WORK UNIT NOS.

8687 n/a n/a

c. DOD ELEMENT

61101D

d. DOD SUBELEMENT

n/a

10. DISTRIBUTION STATEMENT

1 A - Approved for public release; distribution unlimited

11. SUPPLEMENTARY NOTES

This research was supported by
Advanced Research Projects Agency

12. SPONSORING MILITARY ACTIVITY

Air Force Cambridge Research
Laboratories (LQ)
L.G. Hanscom Field
Bedford, Massachusetts 01730

13. ABSTRACT

The increase in terminal currents and noise observed at high drain bias in MOS field-effect transistors is explained by quantitative models that give predictions in good agreement with experiment. We describe the fabrication and resulting properties of a new type of Schottky barrier photodiode. An explanation is proposed for the fall-off in quantum yield observed in metal-semiconductor photodiodes for excitation wavelengths in the near UV region of the spectrum. New results are given for the electron and hole capture rates associated with the defect centers produced by nickel in germanium. The results of basic optical and electrical measurements are reported for amorphous semiconductor As_2Se_3 , Sb_2Se_3 films fabricated by evaporation. Monochromated Guinier-deWolff and Guinier-Lenné x-ray powder cameras and a scanning microdensitometer are combined into a data system for studying solid state reaction kinetics. The changes in the short range ordered structure of an Ni_3Fe alloy are determined for a series of anneals between 0 and 40 hours at 480°C .

Security Classification

| 14. | KEY WORDS | LINK A | | LINK B | | LINK C | |
|-----|---|--------|----|--------|----|--------|----|
| | | ROLE | WT | ROLE | WT | ROLE | WT |
| | silicon noise photodetectors semiconductor devices amorphous semiconductors | | | | | | |

A CENTER OF COMPETENCE IN SOLID STATE MATERIALS AND DEVICES

by

Fredrik A. Lindholm, Eugene R. Chenette, Robert W. Gauld,
Larry L. Hench, Sheng S. Li, Aldert van der Ziel

Electrical Engineering Department
College of Engineering
University of Florida
Gainesville, Florida 32601

Contract Na. F 19628-68-C-0058

Project Na. 8687

Scientific Report Na. 9
10 April 1972

Contract Monitor
Andrew C. Yang
Solid State Sciences Laboratory

Approved for public release; distribution unlimited.

Sponsored by

Advanced Research Projects Agency
ARPA Order No. 1060

Monitored by

AIR FORCE CAMBRIDGE RESEARCH LABORATORIES
AIR FORCE SYSTEMS COMMAND
UNITED STATES AIR FORCE
BEDFORD, MASSACHUSETTS 01730

Program Code No. 1D10
Effective Date of Contract 11 September 1967
Contract Expiration Date 31 August 1972
Principal Investigator and Phone No. Dr. Fredrik A. Lindholm/904 392-0904
Project Scientist and phone no. Dr. Andrew C. Yang/617 861-2225

Qualified requestors may obtain additional copies from the
Defense Documentation Center. All others should apply to the
National Technical Information Service.

ABSTRACT

The increase in terminal currents and noise observed at high drain bias in MOS field-effect transistors is explained by quantitative models that give predictions in good agreement with experiment. We describe the fabrication and resulting properties of a new type of Schottky barrier photodiode. An explanation is proposed for the fall-off in quantum yield observed in metal-semiconductor photodiodes for excitation wavelengths in the near UV region of the spectrum. New results are given for the electron and hole capture rates associated with the defect centers produced by nickel in germanium. The results of basic optical and electrical measurements are reported for amorphous semiconductor $\text{As}_2\text{Se}_3\text{Sb}_2\text{Se}_3$ films fabricated by evaporation. Monochromated Guinier-deWolff and Guinier-Lenné x-ray powder cameras and a scanning microdensitometer are combined into a data system for studying solid state reaction kinetics. The changes in the short range ordered structure of an Ni_3Fe alloy are determined for a series of anneals between 0 and 40 hours at 480°C .

SUMMARY

This report, for the ninth semi-annual period of contract support, describes technical findings in two main subject areas: semiconductors and semiconductor devices; and measurement techniques.

SEMICONDUCTORS AND SEMICONDUCTOR DEVICES:

The increase in terminal currents and noise observed at high drain bias suggests the presence of avalanche multiplication near the drain of MOS field-effect transistors. Quantitative models are developed that predict values of noise and terminal currents in good agreement with experiment. The results demonstrate that surface scattering strongly affects the ionization rates and that one type of carrier predominates in the avalanche process.

We describe the fabrication and properties of a new type of Schottky barrier photodiode. The novelty in structure consists in the mask for metallization which forms a grating of gold film contacting the n-type silicon substrate. In spectral response, quantum yield, speed and noise, the device shows better performance than that reported for previous silicon Schottky barrier diodes.

An explanation is proposed for the fall-off in quantum yield observed in metal-semiconductor photodiodes for excitation wavelengths in the near UV region of the spectrum. Calculations based on supposing the existence of an inversion region bounding the metal-semiconductor interface agree well with experimental observations.

New results, believed to be more accurate than values reported previously, are given for the electron and hole capture rates associated with the defect centers produced by nickel in germanium. In contrast with previous studies, we deduce the rates using the photomagnetolectric and photoconductive effects, taking careful account of the effects of excess carrier trapping. Moreover, we ensure sensitive control of the compensation ratio of the nickel and the shallow impurity densities.

The results of basic optical and electrical measurements are reported for amorphous semiconductor $\text{As}_2\text{Se}_3\text{Sb}_2\text{Se}_3$ films fabricated by evaporation. Transmittance and absorption studies made in the 0.7 to 16 micron range provide information about the refractive index, the static relative dielectric constant, the relaxation time, the mobility and the thermal coefficient of

energy. Measurement of the electrical conductivity as a function of temperature, applied field, and illumination provides additional basic information about transport processes and trapping levels. From the understanding lent by the combination of these measurements, we propose a plausible energy band configuration.

MEASUREMENT TECHNIQUES:

The combined use of monochromated Guinier-deWolff and Guinier-Lenné x-ray powder cameras and a scanning microdensitometer provides a powerful tool for studying solid state reaction kinetics. Application of the room-temperature and high-temperature cameras to both interface-controlled and diffusion-controlled kinetics is discussed. Additionally, we describe requirements for quantitative sample preparation, a graphical analysis method and high temperature data refinement. An experimental comparison of detection limits with other x-ray methods in qualitative and quantitative uses of the Guinier cameras demonstrates approximately a factor of 30 advantage for the Guinier cameras in certain applications.

The changes in the short range ordered structure of an Ni_3Fe alloy containing 74 a/o Ni, 26 a/o Fe are determined for a series of anneals between 0 and 40 hours at 480°C . Three-dimensional short range order parameters are determined by diffuse x-ray scattering analysis from a single crystal sample. Two main conclusions result. The ordered arrangement changes from one dominated by nearest neighbor interactions to one with longer range interactions in the period between 8 and 12 hours at 480°C . The time rates of change of the magnetic coercive force, hardness, and electrical resistivity all are approximately equal.

TABLE OF CONTENTS

| | <u>Page</u> |
|--|-------------|
| I. <u>Introduction</u> | 1 |
| II. <u>Semiconductors and Semiconductor Devices</u> (E. R. Chenette, S. S. Li, F. A. Lindholm and A. van der Ziel) | 3 |
| A. NOISE PERFORMANCE OF METAL-OXIDE-SILICON FIELD EFFECT TRANSISTORS (C. S. Kim, E. R. Chenette, A. van der Ziel) | 3 |
| Introduction | 3 |
| Avalanche Ionization and Related Noise in a Mosfet | 5 |
| Experimental Methods | 21 |
| Device fabrication | 21 |
| Device characterization | 23 |
| Noise measurement | 26 |
| Results and Discussions | 31 |
| Conclusions and Recommendations | 53 |
| Appendix I: Calculation of the Variance of the Multi- plication Factor M | 56 |
| Appendix II: Calculation of i_{sub}^2 and i_{dsub}^* | 63 |
| References | 65 |
| B. A NEW GRATING TYPE Au-NSi SCHOTTKY-BARRIER PHOTODIODE FOR 0.4-1.06 MICRON PHOTODETECTION (S.S. Li and C.T. Wang) | 67 |
| Introduction | 67 |
| Device Fabrication | 67 |
| Measurements and Discussions | 69 |
| I-V characteristic curves | 69 |
| Spectral response and quantum yield | 74 |
| Response time | 74 |
| Noise measurments and noise equivalent power (NEP) | 76 |
| References | 79 |
| C. QUANTUM YIELD OF METAL-SEMICONDUCTOR PHOTODIODES (S. S. Li, F. A. Lindholm and C. T. Wang) | 80 |
| Introduction | 80 |
| Existence of an Inversion Layer in a Metal-n-type Semiconductor Diode | 81 |
| Computation of the Inversion and Depletion Layer Widths for a Au-nSi Schottky Diode | 81 |
| Calculation of the Quantum Yield for a Su-nSi Schottky- Barrier Photodiode | 83 |
| Appendix A: Derivation of the Inversion Layer Width for a Metal-n-Type Semiconductor Diode | 90 |
| Appendix B: Derivation of the Quantum Yield for a Metal-n-Type Semiconductor Photodiode when an Inversion Layer is Present | 92 |
| References | 95 |

II. Cont.

| | |
|---|-----|
| D. DETERMINATION OF ELECTRON AND HOLE CAPTURE RATES IN NICKEL-DOPED GERMANIUM USING PHOTOMAGNETOELECTRIC AND PHOTOCONDUCTIVE METHODS (H. F. Tseng and S. S. Li) | 96 |
| Introduction | 96 |
| Theory | 98 |
| Experimental Details | 102 |
| N-type samples | 103 |
| P-type samples | 109 |
| Discussions and Comparison with Previous Work | 110 |
| Conclusions | 112 |
| References | 113 |
| E. AMORPHOUS SEMICONDUCTOR FILMS (P. K. Chaudhari, E. R. Chenette and Z. van der Ziel) | 114 |
| Part 1: Optical Properties of $\text{As}_2\text{Se}_3\text{'Sb}_2\text{Se}_3$ Films | 114 |
| Introduction | 114 |
| Experimental technique | 116 |
| Theories | 118 |
| Results and discussion | 123 |
| Summary and conclusion | 131 |
| References | 132 |
| Part 2: Electrical Properties of $\text{As}_2\text{Se}_3\text{'Sb}_2\text{Se}_3$ Films | 134 |
| Introduction | 134 |
| Experimental details | 135 |
| Results | 136 |
| Discussion | 140 |
| proposed energy-band diagram | 140 |
| low fields conduction | 140 |
| high field conduction | 144 |
| photoconductivity | 145 |
| Summary and conclusions | 147 |
| References | 150 |

III. Measurement Techniques (R. W. Gould and L. L. Hench) 152

| | |
|---|-----|
| A. QUANTITATIVE USE OF GUINEAR X-RAY CAMERAS IN SOLID STATE REACTION KINETICS (D. E. Clar, G. J. Scott and L. L. Hench) | 152 |
| Introduction | 152 |
| Solid State Reaction Kinetics | 153 |
| Description of Two Guinier Cameras | 154 |
| Quantitative Sample Preparation | 158 |
| Methods of Analysis | 163 |
| High Temperature Modification of the Valensi-Carter Equation | 166 |
| Comparison of Standard X-ray Techniques with the Guinier Camera | 167 |
| Summary | 173 |
| Acknowledgements | 173 |
| References | 174 |

III. Cont.

| | |
|---|-----|
| B. A CORRELATION OF THE SHORT RANGE ORDER IN Ni_3Fe WITH CERTAIN PHYSICAL PROPERTIES OF THIS ALLOY (W. L. Wilson and R. W. Gould) | 175 |
|---|-----|

| | |
|------------------------|-----|
| Introduction | 175 |
| Experimental | 176 |
| Results and Discussion | 179 |
| Conclusions | 181 |
| References | 184 |

| | |
|-----------------------|-----|
| IV. <u>Discussion</u> | 185 |
|-----------------------|-----|

I. Introduction

The original general objective of this research program was to establish at the University of Florida a "Center of Competence in Solid State Materials and Devices" capable of doing research of benefit to the Department of Defense. At this stage, four and one half years following initiation of contract support, ample evidence exists that the University of Florida has indeed become such a center of competence. Among the evidence supporting this conclusion are the technical findings fostered by this contract. These are documented in the eight previous reports in this series¹⁻⁸ and in 109 related papers published in research journals.

During the past year the objectives of the research program have shifted decisively. In accordance with an agreement made with the contract monitor in January 1971, we have focussed the objectives to give greatest emphasis to the following problem areas:

1. The development of new types of detectors with stress given to utilizing the Demer and photomagnetolectric effects in semiconductors and to utilizing new mask geometries for Schottky barrier detectors compatible with conventional silicon technology.
2. The incorporation of the effects of irradiation into the characterization of device behavior; junction field-effect devices are to receive special attention. Emphasis is placed on the development of characterizations enabling computer simulation and design of circuits.
3. Full static and dynamic characterization of bipolar and field-effect devices aiming both toward improved device design and toward improved circuit implementation. The characterization is to deal with operation over a wide range of temperatures, with emphasis on the range between ordinary room temperature and cryogenic temperatures.
4. Noise studies proceeding collaterally with each of the efforts listed above.
5. Radiation studies of amorphous semiconductors.

For the most part, the content of the present report reflects this change in emphasis. Section II, concerning semiconductors and semiconductor devices, describes studies in detectors, field-effect devices, noise, and amorphous semiconductors. Section III, however, which deals with measurement techniques, describes the results of research begun before the implementation of our change in emphasis.

REFERENCES

1. F. A. Lindholm et al, Scientific Report No. 1, Contract #F 19628-68-C-0058, College of Engineering, University of Florida, 10 April 1968.
2. F. A. Lindholm et al, Scientific Report No. 2, Contract #F 19628-68-C-0058, College of Engineering, University of Florida, 10 October 1968.
3. F. A. Lindholm et al, Scientific Report No. 3, Contract #F 19628-68-C-0058, College of Engineering, University of Florida, 10 April 1969.
4. F. A. Lindholm et al, Scientific Report No. 4, Contract #F 19628-68-C-0058, College of Engineering, University of Florida, 10 October 1969.
5. F. A. Lindholm et al, Scientific Report No. 5, Contract #F 19628-68-C-0058, College of Engineering, University of Florida, 10 April 1970.
6. F. A. Lindholm et al, Scientific Report No. 6, Contract #F 19628-68-C-0058, College of Engineering, University of Florida, 10 October 1970.
7. F. A. Lindholm et al, Scientific Report No. 7, Contract #F 19628-68-C-0058, College of Engineering, University of Florida, 10 March 1971.
8. F. A. Lindholm et al, Scientific Report No. 8, Contract #F 19628-68-C-0058, College of Engineering, University of Florida, 10 October 1971.

II. Semiconductors and Semiconductor Devices (E. R. Chenette,
S. S. Li, F. A. Lindholm and A. van der Ziel)

A. NOISE PERFORMANCE OF METAL-OXIDE-SILICON FIELD EFFECT
TRANSISTORS (C. S. Kim, E. R. Chenette, A. van der Ziel)

1. INTRODUCTION

Since the Metal-Oxide-Semiconductor-Field-Effect-Transistor (MOSFET) was first introduced, much work has been done on its basic device characteristics and noise.^{1,2} With the advances in fabrication technology, large scale MOS integrated circuits have become popular and a new memory device, called the charge-coupled MOS device, has been introduced. MOS devices are widely favored over bipolar devices in cryogenic applications and in many high frequency communication circuits. It is probable that research on MOS devices will continue to provide for the development of new and important FET applications.

Avalanche ionization occurring in the channel-to-drain-depletion (CDD)³ region of an FET has recently received considerable attention. This phenomenon was first noticed in the form of the excess gate current in junction gate FET'S operating at low temperatures.⁴ The anomalous noise enhancement observed when operating at low temperatures of far beyond saturation has been credited to this avalanche ionization.^{5,6} Klaassen drew from his experiments the qualitative conclusion that the noise associated with the excess substrate current in a MOSFET resulted from avalanche ionization was a superlinear type of shot noise.⁷ The expression he presented for this noise is

$$\overline{i_{\text{sub}}^2} = 2 q M(I_{\text{sub}}) I_{\text{sub}} \quad (1.1)$$

where $M(I_{\text{sub}})$ is the current-dependent shot noise multiplication and I_{sub} is the average substrate current.

The purpose of the present work is to give a clear physical picture of how this avalanche ionization in the CDD region of a FET occurs. A quantitative model for the noise associated with the avalanche current was developed; it compared favorably with our experimental results.

The study of avalanche mechanism in FET's led to a convenient method of measuring avalanche ionization rates. The previous experimental method on a two-terminal device involved the necessity of distinguishing between two currents of nearly identical magnitudes. This limited the accuracy of the measurement. Furthermore the evaluation of the ionization rate of majority carriers from the data required a proper correction for the contribution to the avalanche current from minority carriers.

These difficulties are eliminated in experiments with the avalanche current in four-terminal devices such as FET's, due to the uniqueness of its avalanche mechanism. The reason is that the minority carriers are collected by the gate (in a JFET) or by the substrate (in a MOSFET); this considerably simplifies the avalanche picture.

The contribution of this work is establishing a clear physical picture of the avalanche ionization mechanism in a MOSFET and substantiating it with noise study.

II. AVALANCHE IONIZATION AND RELATED NOISE IN A MOSFET

The drain terminal current of a MOSFET at the onset of saturation can be expressed in terms of terminal voltages and other device parameters in the following way.⁸

$$I_D = (\mu_{eff} C_{ox} Z/L) \{V_G' V_{DS} - V_{DS}^2 - (4/3) \phi_F V_B [\beta(V_{DS})^{3/2} - \beta(0)^{3/2}]\} \quad (2.1)$$

Here, $\beta(V) = 1 + (V - V_{SUB}) / 2\phi_F$ and

$$V_G' = V_G - \psi_{so} - \phi_{MS}' + V_{ss}$$

Other symbols are defined as follows:

μ_{eff} = effective mobility

C_{ox} = oxide capacitance

L = channel length

Z = channel width

ϕ_F = bulk Fermi potential

ψ_{so} = surface potential at source junction

ϕ_{MS}' = work function difference between metal and semiconductor

V_G = gate terminal voltage

V_{SUB} = substrate terminal voltage

V_{DS} = drain terminal voltage at the onset of saturation

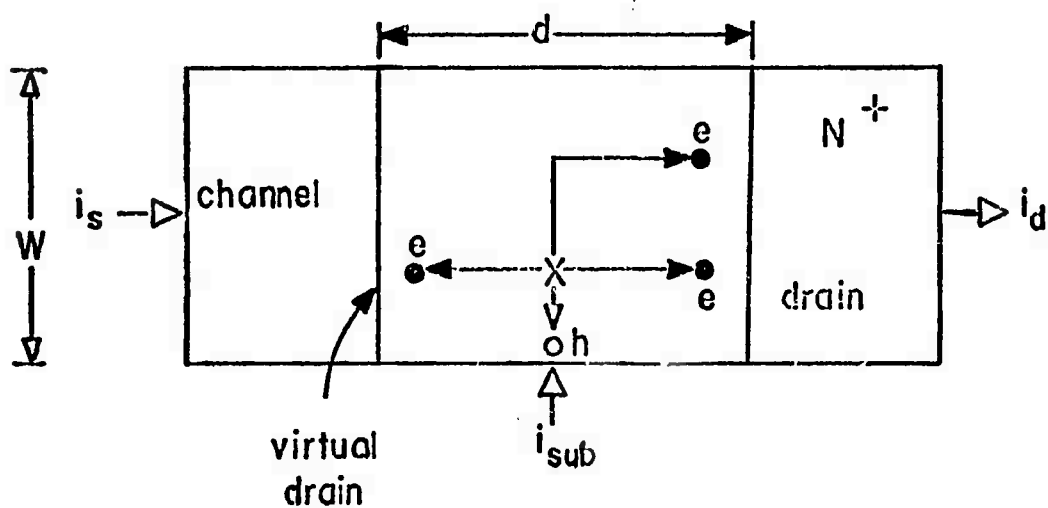
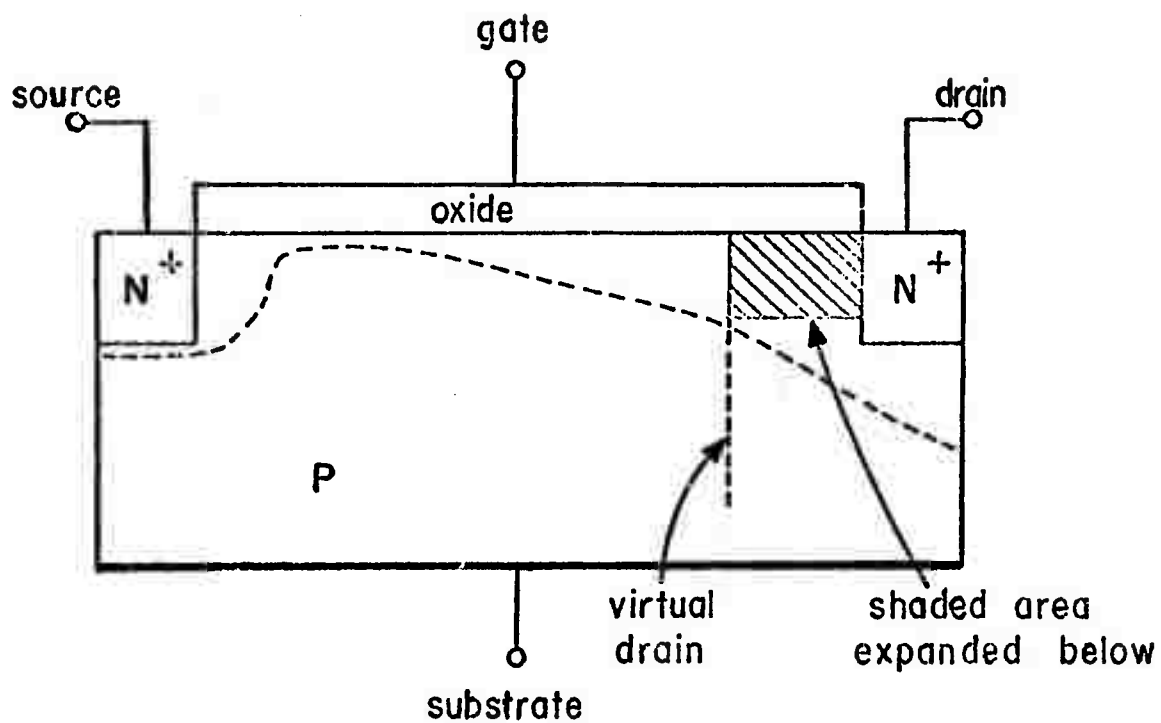
$V_{ss} = Q_{ss}/C_{ox}$ = surface and oxide charge in equivalent voltage.

In deriving the above equation the mobile charge density in the conducting channel is usually assumed to depend only on the component of electric field which is normal to the surface. (Gradual Channel Approximation) This assumption deteriorates in the vicinity of drain junction as the MOSFET is biased beyond saturation, and mobile carriers are depleted from this region.

The FET is usually divided into two regions along the channel in order to describe the saturation characteristics; one extends from the source to the virtual drain where the gradual channel approximation is still valid and the other from the virtual drain to the actual drain where the depletion approximation can be used. Then the channel length and the saturation drain voltage in Eq. (2.1) must be replaced by the length from the source to the virtual drain and the actual channel potential at the virtual drain, respectively, to obtain the saturation drain current.

When the drain is biased well beyond saturation the electric field along the direction of electron flow in the channel-to-drain-depletion (CDD) region becomes sufficiently high to cause avalanche ionization. Avalanche ionization can occur before the depletion region reaches through to the source junction or before the drain-substrate diode breaks down in the reverse direction.

Figure (2.1) shows a sketch of the CDD region of a FET. It is assumed that the drain current is carried in a thin slab near the interface of the oxide and the semiconductor. It is not necessary to consider the effect of the transverse electric field in detail. The transverse electric field does not affect the avalanche process directly; it only serves to remove minority carriers generated when ionizing



i_d = electrons collected at drain terminal

i_{sub} = holes collected at substrate

i_s = electrons entering channel from source terminal.

Figure 2.1--Sketch of CDD Region

collisions occur. This is probably the most important difference between the avalanche process as it occurs in the CDD region of a FET and in the avalanche diode. With this device it is possible to study avalanche multiplication of electrons alone or of holes alone. The simple one-dimensional model of Fig. (2.1) provides a useful description of the processes involved.

Consider an n-channel MOSFET. Here the current is carried by electrons. The channel current from the source region, I_s , enters from the left hand side and passes through the CDD region, w , is smaller than a Debye length for most of the current densities of interest the secondary holes are scattered out of the CDD region. These holes are collected at the substrate terminal as I_{sub} because of the transverse component of the electric field. Both primary and secondary electrons are collected at the drain terminal and cause the drain current I_d .

The sign of the current is taken positive in the direction of electron flow. Obviously we have

$$I_d = I_s + I_{sub} \quad (2.2)$$

The conventional multiplication factor is defined as the ratio of the average total electron current emerging out of the CDD region to the electron current entering it.

$$\bar{M} = \bar{i}_d / \bar{i}_s = I_d / I_s \quad (2.3)$$

The secondary holes do not participate in the avalanche multiplication because the transverse component of the electric field is not

sufficiently high to cause ionizing collisions. If we neglect the thermal generation and recombination of carriers in the CDD region, the current increase in an infinitesimally small region between y and $y+dy$ can be described by the following differential equation.

$$dI(y) = I(y)\alpha(y) dy \quad (2.4)$$

where $\alpha(y)$ is the ionization rate, defined as the number of ionizations per unit length. Solving the above equation with a proper set of boundary conditions we have

$$\begin{aligned} I(y) &= I_s \exp \left(\int_0^y \alpha(y') dy' \right) \\ I_d &= I_s \exp \left(\int_0^d \alpha(y) dy \right) \end{aligned} \quad (2.5)$$

The multiplication factor can thus be written as

$$\bar{M} = \exp \left(\int_0^d \alpha(y) dy \right) \quad (2.6)$$

A first order approximation of the electric field distribution in the CDD region can be obtained from the one-dimensional solution of Poisson's equation.

$$dE(y)/dy = q N_A / K_s \epsilon_0 \quad (2.7)$$

where, q = electron charge

N_A = acceptor impurity density

K_s = dielectric constant of silicon

ϵ_0 = permittivity of free space

The CDD region starts from the virtual drain located at $y = \ell$.

The electric potential at the virtual drain can be approximated by the

drain saturation voltage V_{ds} . The solution of Eq. (2.7) gives

$$E(y) = E_s + a (y - \ell)$$

$$E_d = E_s + a d \approx a d \quad \text{where } E_d \gg E_s \text{ is assumed} \quad (2.8)$$

$$d = L - \ell = a^{-1/2} (V_d - V_{ds})^{1/2}$$

where the boundary values and constant a are defined as

$$\begin{aligned} E(L) &= E_d, \quad E(\ell) = E_s, \quad V(L) = V_d, \quad V(\ell) = V_{ds} \\ a &= q N_A / K_s \epsilon_0 \end{aligned} \quad (2.9)$$

The field dependence of the ionization rate for the case of a small electric field is well approximated by ^{9, 10}

$$\alpha(E) = A \exp (-B/E) \quad (2.10)$$

where A and B are constants determined by the scattering parameters and the threshold energy for the avalanche ionization. In the MOSFET case surface scattering plays a dominant role in decreasing the kinetic energy of the electron gained from the electric field. How this additional mechanism of surface scattering will affect the field dependence of the ionization rate in Eq. (2.10) is not available in the literature.

For a value of \bar{M} close to unity, Eq. (2.6) can be approximated by

$$\bar{M} = \exp \left(\int_0^d \alpha(E) dy \right) \approx 1 + \int_0^d \alpha(E) dy \quad (2.11)$$

Combining Eq. (2.2), (2.3), (2.8), (2.10) and (2.11), the substrate current can be written as

$$\begin{aligned}
I_{\text{sub}} &= I_s (\bar{M} - 1) \\
&= I_s \int_0^L \alpha(E) dy \\
&= I_s \int_0^L A \exp(-B/E) dy \\
&= I_s (A/a) \int_{E_s}^{E_d} \exp(-B/E) dE, \text{ where } dy = a^{-1} dE \\
&= I_s (A/a) \int_{E_d^{-1}}^{E_s^{-1}} \exp(-Bz)/z^2 dz, \text{ where } E = 1/z, dE = -z^{-2} dz \\
&= I_s (A/a) [E_d \exp(-B/E_d) - E_s \exp(-B/E_s) + B E_i(B/E_d) \\
&\quad - B E_i(B/E_s)] \tag{2.12}
\end{aligned}$$

where the symbol $E_i(x)$ refers to the exponential integral defined by

$$E_i(x) = \int_x^\infty \exp(-t)/t dt \text{ with } x > 0 \tag{2.13}$$

If we assume $E_d \gg E_s$, we obtain

$$\begin{aligned}
I_{\text{sub}} &\approx I_s (A/a) E_d \exp(-B/E_d) \\
&= I_s A a^{-1/2} (V_d - V_{ds})^{1/2} \exp[-2B/a^{1/2} (V_d - V_{ds})^{1/2}] \tag{2.14}
\end{aligned}$$

The calculation of the integral in Eq. (2.12) enables us to rewrite Eq. (2.6) as

$$\begin{aligned}
\ln M &= (A/a) [E_d \exp(-B/E_d) - E_s \exp(-B/E_s) + B E_i(B/E_d) \\
&\quad - B E_i(B/E_s)] \\
&= (A/a) [E_d \exp(-B/E_d) + B E_i(B/E_d)] \tag{2.15}
\end{aligned}$$

where $E_d \gg E_s$ is again assumed.

Summarizing the result we have the following expressions for the terminal currents.

$$\begin{aligned}
 I_s &= (\nu_{\text{eff}} C_{\text{ox}}^2 / 1) (V_G' V_{ds} - V_{ds}^2 - (4/3) \phi_F V_B [\beta (V_{ds})^{3/2} - \beta(0)^{3/2}]) \\
 I_{\text{sub}} &= I_s A_s a^{-1/2} (V_d - V_{ds})^{1/2} \exp [-2B / a^{1/2} (V_d - V_{ds})^{1/2}] \\
 I_d &= I_s \{1 + \Delta a^{-1/2} (V_d - V_{ds})^{1/2} \exp [-2B / a^{1/2} (V_d - V_{ds})^{1/2}]\} \quad (2.16)
 \end{aligned}$$

The multiplication noise for the case of avalanche diodes has been well formulated by many authors.^{11, 12} The avalanche multiplication noise in MOSFET's has to be treated differently from that in p-n junctions for two main reasons. First, only one type of current carrier (electrons in n-channel, holes in p-channel devices) is active in the multiplication process. Secondly, the current entering the multiplication region does not exhibit full shot noise. This is obvious in the sense that the channel noise in FET's in its limiting form is thermal noise proportional to the channel conductance.

The multiplication process is a random process. Therefore, when one electron entering the multiplication region (in this case, the CDD region) causes M electrons to emerge out of it, M is a random integer. Since each electron goes through an independent random process we can write for the total number of electrons collected,

$$n_d = \sum_{i=1}^{n_s} M_i \quad (2.17)$$

where n_s and M_i are both fluctuating quantities in the time domain.

In calculating $\overline{n_d}$, the average number of electrons collected at the drain terminal, we first set up a subensemble of unit time elements

during which the same number of n_s primaries enter the multiplication region. We take the average over this subensemble, i.e.,

$$\overline{n_d^s} = n_s \overline{M} \quad (2.18)$$

Then we set up the entire ensemble consisting of all these subensembles, and take the average, i.e.,

$$\overline{n_d} = \overline{\overline{n_d^s}} = \overline{n_s \overline{M}} = \overline{n_s} \overline{M} \quad (2.19)$$

Applying the same concept involved in Eq. (2.18) and (2.19), we can calculate the variance of n_d as follows:

$$n_d^2 = \left(\sum_{i=1}^{n_s} M_i \right) \left(\sum_{j=1}^{n_s} M_j \right) = \sum_{i=1}^{n_s} \sum_{j=1}^{n_s} M_i M_j \quad (2.20)$$

In Eq. (2.20) the double summation results in $n_s (n_s - 1)$ terms with different i, j and in n_s terms with same i, j . Hence,

$$\begin{aligned} \overline{n_d^2}^s &= n_s (n_s - 1) \overline{M_i M_j} + n_s \overline{M_i^2} \\ &= n_s (n_s - 1) \overline{(M_i)^2} + n_s \overline{M_i^2} \\ &= n_s \text{Var } M + n_s^2 \overline{(M)}^2 \end{aligned} \quad (2.21)$$

Therefore,

$$\overline{n_d^2} = \overline{n_s} \text{Var } M + \overline{n_s^2} \overline{(M)}^2$$

and,

$$\begin{aligned} \text{Var } n_d &= \overline{n_s} \text{Var } M + \overline{n_s^2} \overline{(M)}^2 - (\overline{n_s})^2 \overline{(M)}^2 \\ &= \text{Var } n_s \overline{(M)}^2 + \overline{n_s} \text{Var } M \end{aligned} \quad (2.22)$$

The derivation of Eq. (2.22) from Eq. (2.17) actually furnishes proof of the so-called Burgess' Variance Theorem. According to another theorem (van der Ziel, Noise; Sources, Characterization, Measurement, Prentice-Hall, Inc., Englewood Cliffs, N. J., 1970, p. 15) the low frequency spectrum of the random variable n_d is

$$S_{n_d}(0) = 2 \text{ Var } n_d \quad (2.23)$$

Combining Eq. (2.22) and (2.23), the noise spectrum of the drain current i_d will be

$$\begin{aligned} S_{i_d}(0) &= q^2 2 \text{ Var } n_d \\ &= 2 q^2 (\bar{M})^2 \text{ Var } n_s + N_s \text{ Var } M \end{aligned} \quad (2.24)$$

We can represent these noises by their corresponding equivalent noise diode currents, $I_{eq} = S(0)/2q$.

$$I_{eqs} = S_{i_s}(0)/2q = q \text{ Var } n_s \quad (2.25)$$

$$I_{eqd} = S_{i_d}(0)/2q = I_{eqs} (\bar{M})^2 + I_s \text{ Var } M \quad (2.26)$$

where $I_s = q N_s$. Note that $I_{eqs} \neq 2 q I_s$. In other words, the electron current entering the multiplication region does not show full shot noise as in the case of the avalanche diode; instead it shows the low-field channel noise of the FET.

The next step is to calculate the variance of M . Let us assume that the multiplication process is a random process with its probability density obeying Poisson's law. This assumption should be valid since the individual ionizing events are independent. We can write the probability that an electron entering the multiplication region will produce

m ionization events as

$$P_m = \frac{u^m}{m!} \exp(-u) \quad (2.27)$$

where $u = \bar{m} = \bar{\alpha} d$, is the average number of ionization events and $\bar{\alpha}$ is the average ionization rate of an electron per unit distance.

If we define $P(M)$ as the probability of M electrons emerging at the drain terminal due to one electron entering the multiplication region, we have

$$P(1) = P_0 = \exp(-u) \quad (2.28)$$

In other words $P(1)$ is the probability that an electron will pass through the multiplication region without going through an ionizing collision.

When one electron goes through one ionizing collision during its path through the multiplication region, two electrons will emerge out of the drain terminal and one hole will emerge out at the substrate terminal. Now $P(2)$ has to be calculated by counting the probability of having one ionizing collision at a certain point along the path times the probability of both primary and secondary electrons traveling the rest of the path without having any ionizing collision and then by summing this product over the probability distribution of having the initial ionization at different points along the path. Following this line of reasoning we can get the general expression of $P(M)$ as

$$P(M) = C_M \exp(-Mu) [\exp(u) - 1]^{M-1} \quad (2.29)$$

where C_M is a constant coefficient.

Obviously,

$$\sum_{M=1}^{\infty} P(M) = 1 \quad (2.30)$$

and,

$$\frac{\partial}{\partial \mu} \left[\sum_{M=1}^{\infty} P(M) \right] = \sum_{M=1}^{\infty} \frac{\partial}{\partial \mu} P(M) = 0 \quad (2.31)$$

Combining Eq. (2.29), (2.30) and (2.31), yields

$$\bar{M} = \exp(u)$$

$$\overline{M^2} = 2 \overline{(M)^2} - \bar{M}$$

$$\text{Var } M = \overline{M^2} - (\bar{M})^2 = \bar{M} (\bar{M} - 1) \quad (2.32)$$

The detailed derivations of Eqs. (2.29) and (2.32) are presented in the appendix. Eq. (2.32) was already given by Tager.¹¹

Substituting Eq. (2.32) into Eq. (2.26) and using $I_{\text{sub}} = I_s (\bar{M} - 1)$, we get,

$$I_{\text{eqd}} = I_{\text{eqs}} (\bar{M})^2 + I_{\text{sub}} \bar{M} \quad (2.33)$$

In the appendix the detailed calculation of the noise in the substrate terminal current and the correlated part in the drain noise and the substrate noise is carried out. The result is

$$I_{\text{eqsub}} = I_{\text{eqs}} (\bar{M} - 1)^2 + I_{\text{sub}} \bar{M} \quad (2.34)$$

$$I_{\text{eqd,sub}} = I_{\text{eqs}} \bar{M}(\bar{M} - 1) + I_{\text{sub}} \bar{M} \quad (2.35)$$

The above derivation was based on a corpuscular picture of the avalanche noise process. The same result can be obtained by a more collective approach. Rewriting Eq. (2.4), including the time dependence

and solving it we have

$$i(y, t) = i(0, t) \exp \left(\int_0^y \alpha(y', t) dy' \right) \quad (2.36)$$

$$i_d = i_s \exp \left(\int_0^d \alpha(y, t) dy \right) = i_s M(t) \quad (2.37)$$

Since there is no physical reason for spatial correlation in the fluctuation of the avalanche ionization,

$$\overline{di(y, t), di(y', t)^*} = 0 \quad (2.38)$$

If we assume that the avalanche ionization in the infinitesimally small subregion is a pure random process, we can expect that each incremental current, di , will show full shot noise with a white spectrum.

$$\overline{di(y, t)^2} = dS_i df = 2 q dI(y) df \quad (2.39)$$

Substituting Eq. (2.4) and (2.5) into the above equation we have

$$dS_i(y) = 2 q I_s \alpha(y) \exp \left[\int_0^y \alpha(y') dy' \right] dy \quad (2.40)$$

This shot noise current is amplified through successive avalanche multiplications while flowing the rest of the distance, $d-y$, toward the drain terminal. It appears at the drain terminal as,

$$\begin{aligned} dS_i(d) &= dS_i(y) \exp \left[2 \int_y^d \alpha(y') dy' \right] \\ &= 2qI_s \alpha(y) \exp \left[2 \int_y^d \alpha(y') dy' \right] \exp \left[\int_0^y \alpha(y'') dy'' \right] dy \end{aligned} \quad (2.41)$$

Summing over all these infinitesimal shot noise generators, we have

$$\begin{aligned}
S_i &= \int_0^d dS_i(d) \\
&= 2qI_s \left\{ \exp \left[\int_0^d \alpha(y') dy' \right] \right\}^2 \int_0^d \exp \left[-\int_0^y \alpha(y'') dy'' \right] \alpha(y) dy \\
&= 2qI_s (\bar{M})^2 \int_0^{\ln M} \exp(-z) dz \\
&= 2qI_s (\bar{M})^2 (1 - 1/\bar{M}) \\
&= 2qI_s \bar{M} (\bar{M} - 1)
\end{aligned} \tag{2.42}$$

where $z = \int_0^y \alpha(y') dy'$, and $dz = \alpha(y) dy$.

This only gives the additional noise due to the fluctuation in the avalanche multiplication. In other words we have only considered the fluctuation of the exponential part of Eq. (2.37). The fluctuation of i_s was not considered. If we add the noise of i_s we obtain

$$S_{i_d} = S_{i_d} (\bar{M})^2 + 2qI_s \bar{M} (\bar{M} - 1) \tag{2.43}$$

In a similar way we can derive Eqs. (2.34) and (2.35).

It is not surprising that both approaches give identical results, for both are based on the assumption that the multiplication process is a random process obeying Poisson's law which, in turn, implies shot noise.

Eqs. (2.33), (2.34) and (2.35) summarize the noise behavior of the multiplication process in FET's in a simple form. We can make some interesting observations while studying these equations.

First, the noise in the primary current is amplified during the multiplication process, whether the noise is flicker noise or thermal noise. At low frequencies the flicker noise predominates and the noise at the drain is an amplified thermal noise.

The noise resulting only from the fluctuation in the multiplication is a shot noise with a white spectrum. The magnitude of this noise is $I_{\text{sub}} \bar{M}$, where both I_{sub} and \bar{M} are sensitive functions of drain voltage. At high frequencies this component of noise predominates and the amplified thermal noise is usually buried below this noise level when there are appreciable multiplication currents.

Finally, the multiplication noise in FET's is in general smaller in magnitude than that of an avalanche diode. The reason is due to the difference pointed out earlier i.e., only one type of carrier is active in the multiplication process and the primary current does not display full shot noise.

When both types of carriers go through multiplication the fluctuation of M is much greater. If the ionization rates are assumed to be equal for both electrons and holes, the variance of M in the avalanche diode is ¹¹

$$\text{Var } M = (\bar{M})^2 (\bar{M} - 1) \quad (2.44)$$

If the channel current entering the multiplication region shows full shot noise,

$$I_{\text{eqs}} = I_s \quad (2.45)$$

Then substituting Eq. (2.44) and (2.45) into (2.33) gives

$$\begin{aligned} I_{\text{eqd}} &= I_s (\bar{M})^2 + I_s (\bar{M})^2 (\bar{M} - 1) \\ &= I_s (\bar{M})^3 \end{aligned} \quad (2.46)$$

Eq. (2.46) is identical to the formula for multiplication noise in avalanche diodes based on equal ionization rates for electrons and holes obtained by others. For example, one can obtain Eq. (2.46) by substituting $k=1$ into the formula presented by McIntyre.¹² Here k is the ratio of hole ionization rate to electron ionization rate.

III. EXPERIMENTAL METHODS

A. Device Fabrication

Both n-channel and p-channel si-MOSFET's were fabricated on a 1 ohm-cm substrate with (1,0,0,) orientation. Fig. (3.1) shows the geometry of the devices. Devices with channel lengths of 1, 2 and 4 mils were made on the same wafer. The gate was allowed to overlap about one tenth of a mil on each side toward the source and the drain.

The wafer was stripped of the oxide after diffusion of the source and the drain. The gate oxide was regrown by placing the wafer first in dry oxygen for 30 minutes, then in wet oxygen for 15 minutes; and finally returning it to a dry oxygen environment for one hour. It was then placed in a nitrogen furnace at 900° C for annealing. After etching away the first few hundred Ångströms of oxide from the top, the wafer was boiled in hot hydrochloric acid. It was thoroughly rinsed and placed in a phosphorus diffusion furnace for about ten minutes to grow a phosphor-silicate glass layer.

The back side of the substrate was also doped heavily to form a degenerate layer which provides a good ohmic contact. Gold was used to mount individual chips on the header.

$r_1 = 14$ mils
 $r_2 = 12$ mils
 $r_3 = 11$ mils
 $r_4 = 6.5$ mils

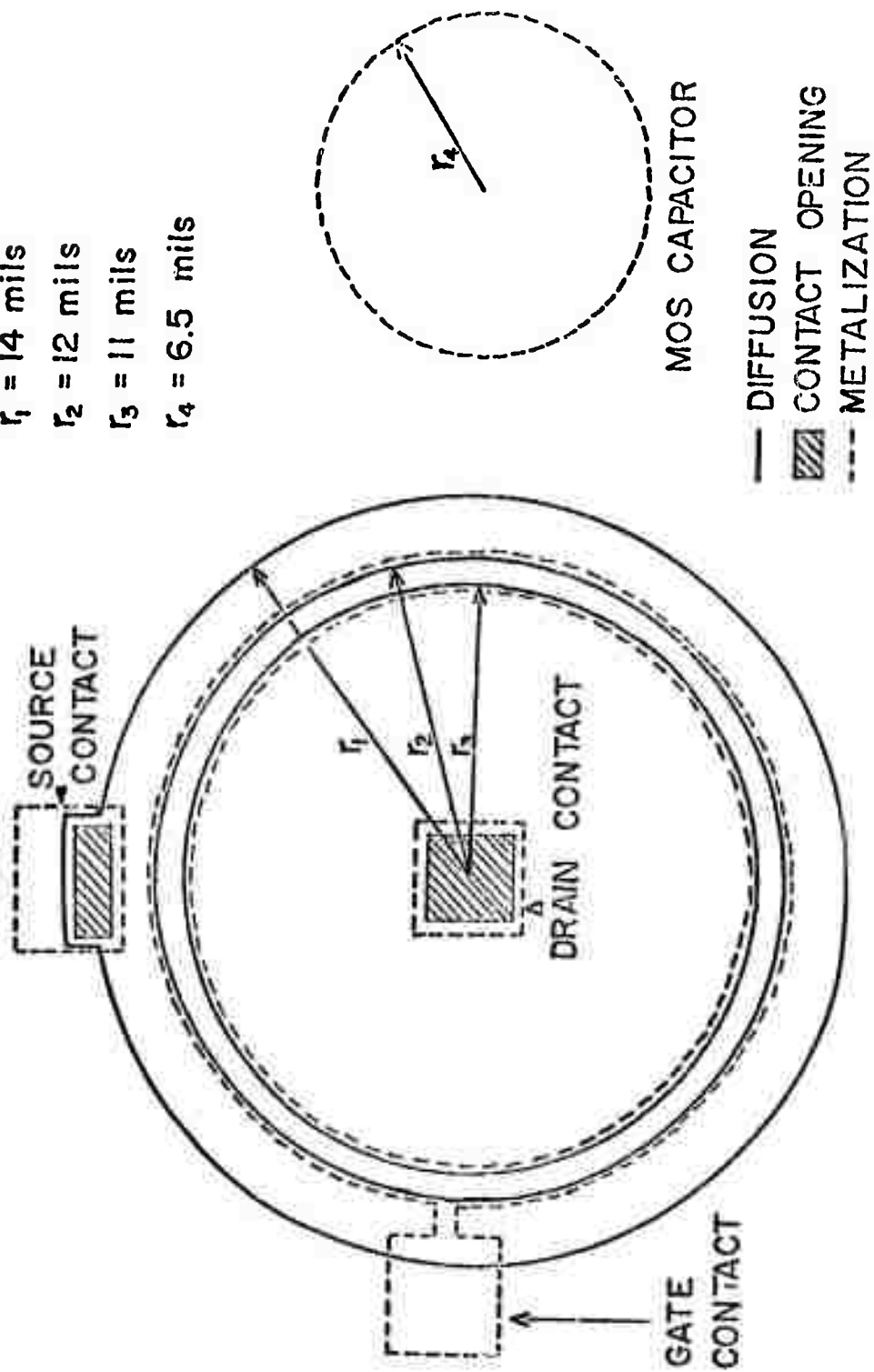


Figure 3.1--Device Layout

B. Device Characterization

The capacitance versus bias voltage measurements on the MOS capacitors which were fabricated close to each device site were performed to determine the oxide thickness, flat band voltage and bulk doping.¹³ Fig (3.2) shows a typical C-V (Capacitance vs. Bias Voltage) curve measured at 1 MHz. The high frequency capacitance minimum gives information on the density of the bulk impurity which contributes to the depletion layer capacitance, the minimum capacitance being the series combination of the oxide capacitance and the depletion layer capacitance.

The channel conductance was plotted on an x-y recorder as a function of the drain bias with the Wayne Derr Model B-641 Autobalance Bridge operating at 1,592 Hz. According to the elementary gradual channel solution these quantities show a linear relationship described by the following equation.

$$g_d = (\mu_{\text{eff}} C_{\text{ox}} Z/L) (V_G' - V_d) \quad (3.1)$$

where the symbols are as defined in Chapter II.

The channel conductance plotted as a function of drain bias exhibits a good linear relationship as shown in Fig. (3.3). The effective gate voltage V_G' lumps the effect of bulk charge, oxide charge and the interface surface states. The effect of the substrate bias voltage is also taken care of by the effective gate voltage. The effective gate voltage was determined by fitting a straight line to the experimental plot and finding the intersection points on the horizontal scale. V_G' thus obtained is equivalent to the drain saturation voltage V_{ds} .

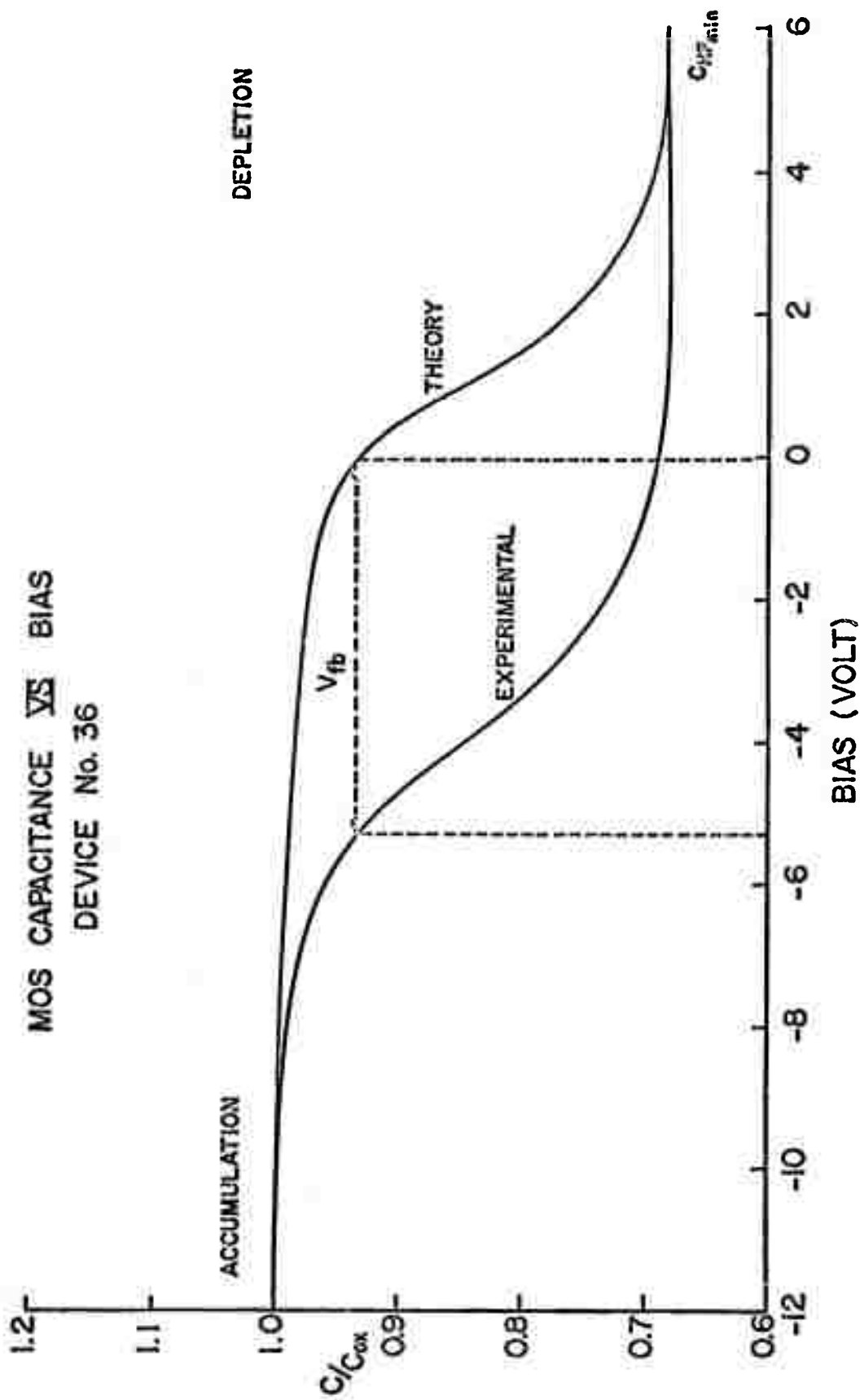


Figure 3.2--Typical C-V Curve

DRAIN CONDUCTANCE Y_D VS DRAIN VOLTAGE

DEVICE No. 38-L

$V_{sub} = -2.0$ volts

$V_G = +8.0$ volts

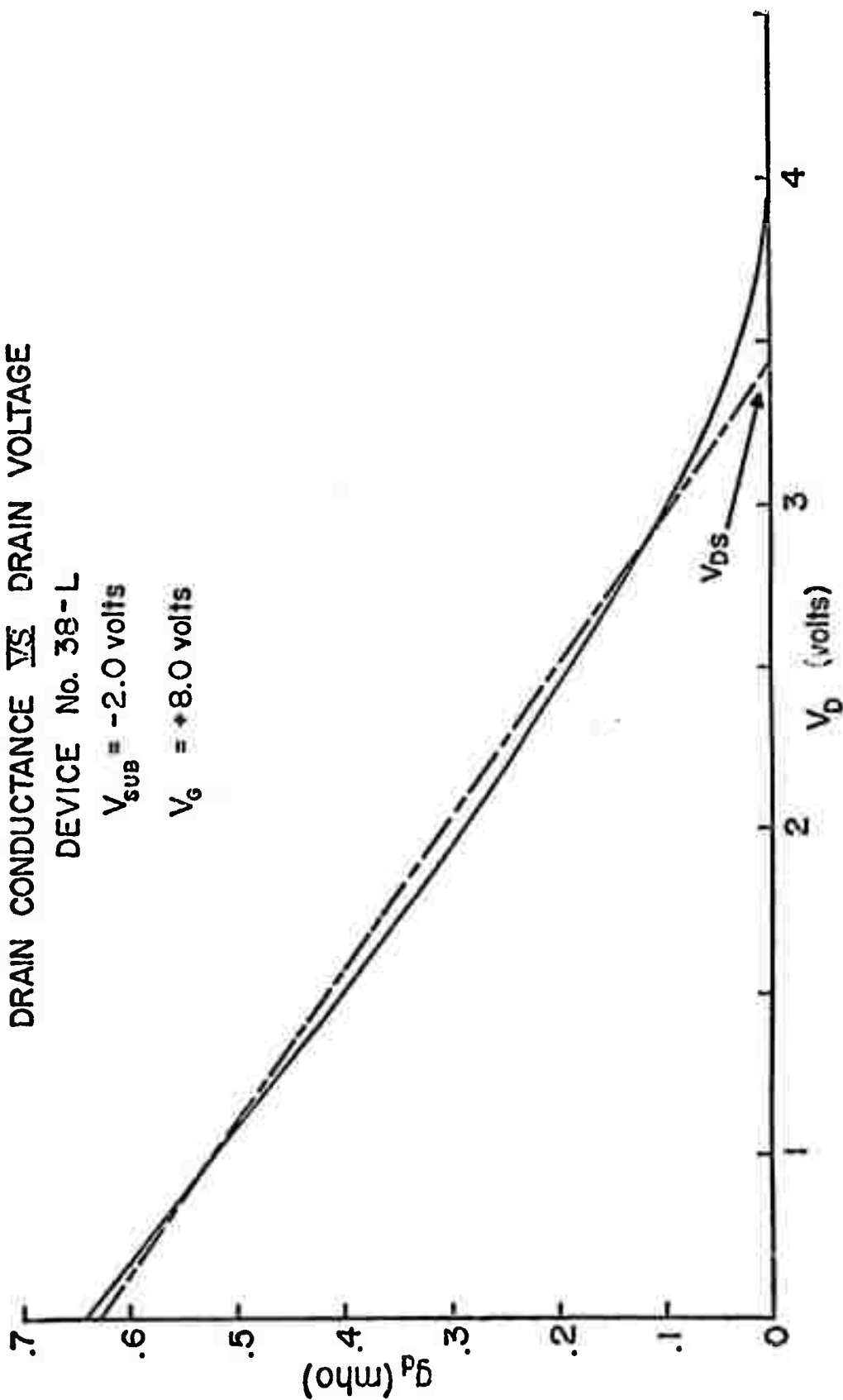


Figure 3.3--Typical Drain Conductance vs. Drain Voltage Curve

The slope of this line which corresponds to the factor $\mu_{\text{eff}} C_{\text{ox}} Z/L$ can be used to determine the effective mobility by substituting the other parameters.

Finally the terminal currents (source, drain and substrate currents) were simultaneously recorded as a function of the drain bias on an x-y recorder. The bias was varied from zero to where the effect of avalanche ionization in the CDD region appears obvious. The substrate current was separately monitored with a nanoampere meter. The average value of the multiplication factor \bar{M} was determined from this measurement using the following relation.

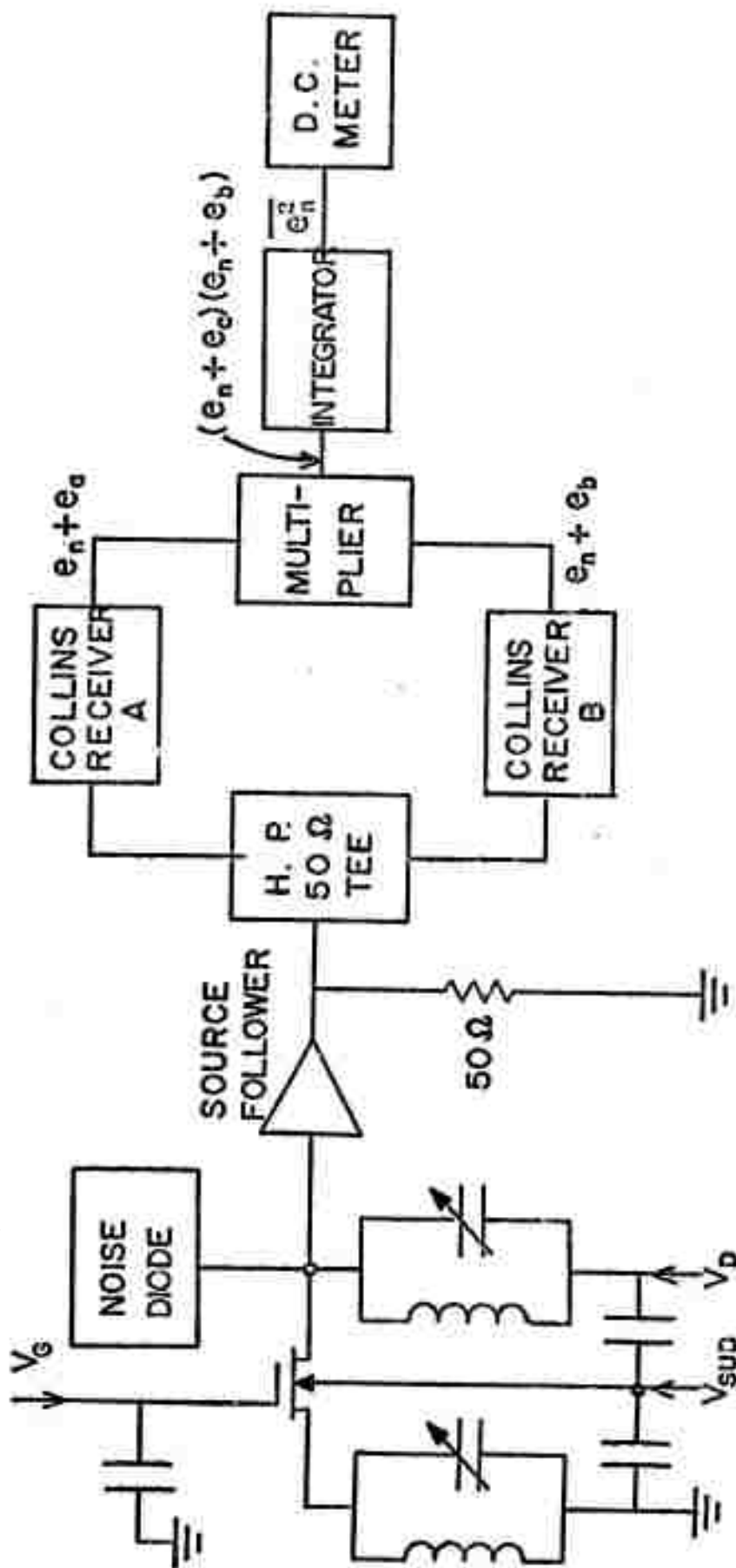
$$\bar{M} = I_d / I_s = (I_s + I_{\text{sub}}) / I_s = 1 + I_{\text{sub}} / I_s \quad (3.2)$$

C. Noise Measurement

The low frequency portions of the noise current spectra were measured with the G. R. 1921 Real Time Spectrum Analyzer and the 310 A H. P. spectrum analyzer. The calibration was achieved by a G. R. Random Noise Generator whose spectral intensity was determined by graphically integrating the output voltage spectrum over the entire frequency range.

The high frequency portion of the noise spectrum was measured by the Hanbury Brown--Twiss type correlation circuit recommended by Chen and van der Ziel.¹⁴ The system consists of two modified Collins Communication Receivers and Cross Correlator circuit built by Kalter.¹⁵ The system set-up is described in Fig. (3.4) The effective noise band-width is determined by the intermediate frequency filter of the receivers.

The noise current source was transformed into a noise voltage source through the source follower. The multiplier and integrator circuit



CROSS CORRELATION SYSTEM BLOCK DIAGRAM

Figure 3.4--Cross Correlation System Set-up

performs the following calculation.

$$\begin{aligned} \overline{(e_n + e_a) G_a (e_n + e_b) G_b} &= G_a G_b (\overline{e_n^2} + \overline{e_n e_a^*} + \overline{e_n e_b^*} + \overline{e_a e_b^*}) \\ &= G_a G_b \overline{e_n^2} \end{aligned}$$

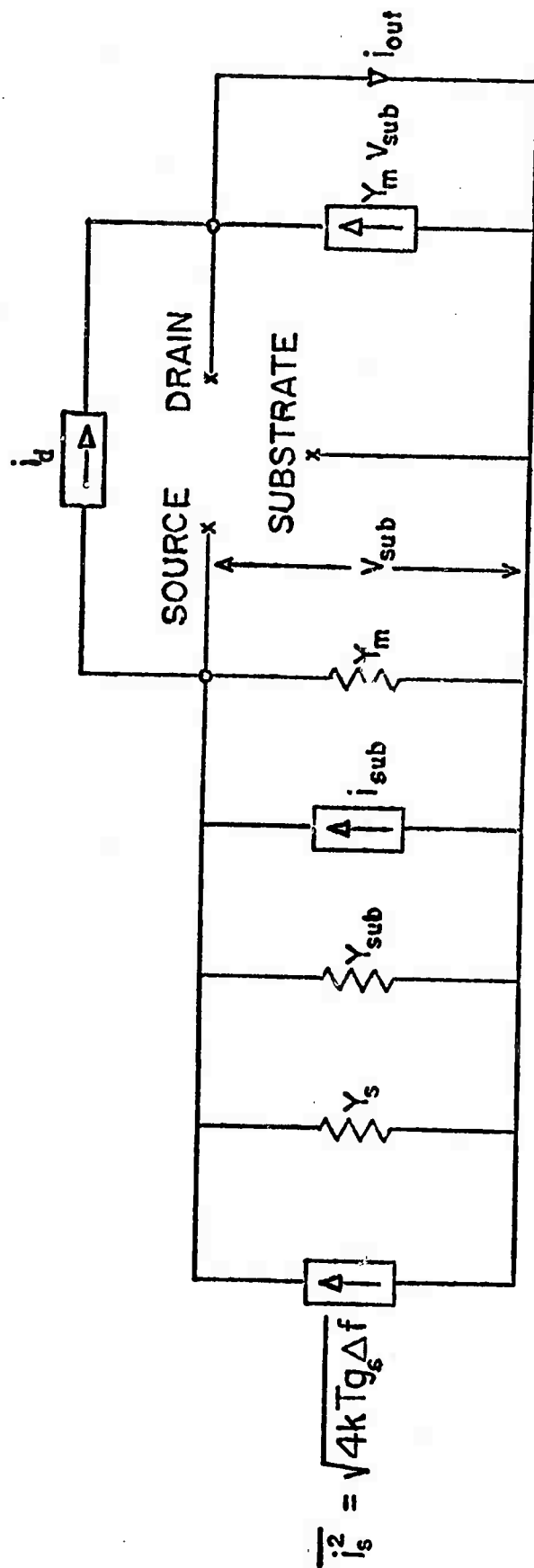
Here $\overline{e_n e_a^*} = \overline{e_n e_b^*} = \overline{e_a e_b^*} = 0$, because the amplifier noise of one channel is not correlated with that of the other channel and the device noise is not correlated with the amplifier noise. The output of the integration circuit therefore responds only to the device noise. It was possible to detect noise currents down to $I_{eq} = 2 \mu$ amp expressed in terms of equivalent saturated diode current, when a high-Q tuned circuit was used as a load for the device.

The device was connected in common substrate (in analogy to common gate) configuration with the gate and substrate a.c. short-circuited to ground. Fig. (3.5) shows the noise equivalent circuit.

If we neglect the thermal leakage current in the reverse biased source to substrate diode and in the drain to substrate diode, the substrate current results only from the multiplication process. Therefore the substrate current noise is fully correlated with the drain noise current. The short-circuited output noise current is given by

$$\begin{aligned} \overline{i_{out}^2} &= \frac{Y_m^2}{|Y_s + Y_{sub} + Y_m|^2} [4kT g_s \Delta f \\ &\quad + \frac{\overline{i_d^2}}{|Y_m|^2} |Y_s + Y_{sub} + \frac{i_{sub} Y_m}{i_d}|^2] \end{aligned} \quad (3.3)$$

Since the transconductance associated with the substrate terminal is much greater than the admittance of the high-Q tuned circuit at the source terminal or the admittance of the source-substrate diode biased



$$V_{sub} = \frac{i_s + i_{sub}}{Y_s + Y_{sub} + Y_m}$$

NOISE EQUIVALENT CIRCUIT OF COMMON SUBSTRATE CONFIGURATION

Figure 3.5--Equivalent Noise Circuit of Common Substrate Configuration

in the reverse direction, we can impose a condition,

$$Y_m \gg Y_s, \quad Y_m \gg Y_{sub} \quad (3.4)$$

This condition reduces Eq. (3.3) to

$$\begin{aligned} \overline{i_{out}^2} &= 4kT g_s \Delta f + \overline{i_{sub}^2} \\ &= 4kT g_s \Delta f + \overline{i_s^2} (\bar{M} - 1)^2 + 2q I_{sub} \bar{M} \Delta f \end{aligned} \quad (3.5)$$

When the source terminal is a.c. short-circuited, the magnitude of the output noise is simply

$$\begin{aligned} \overline{i_{out}^2} &= \overline{i_d^2} \\ &= \overline{i_s^2} (\bar{M})^2 + 2q I_{sub} \bar{M} \Delta f \end{aligned} \quad (3.6)$$

The drain current noise was also measured with all the other terminals a.c. short circuited to ground. The same measurement was done for substrate current noise with all the other terminals a.c. short-circuited to ground.

IV RESULTS AND DISCUSSIONS

The basic device parameters were determined by use of the experimental methods described in the previous chapter and are presented in Table I. The parameter N_{ss} , which lumps the surface states and the fixed charges in the oxide, is higher than is common for commercial devices.

A typical set of the terminal currents measured as a function of drain bias is shown in Fig. (4.1). The increase of drain current and substrate current which occurs well below the drain-substrate diode reverse breakdown voltage is evidence of the presence of avalanche multiplication. The sum of the source and the substrate terminal currents equals the drain terminal current throughout the drain bias range investigated. Furthermore, the source terminal current remains insensitive to drain bias compared to drain and substrate terminal currents. These facts provide firm support for the idea that only electrons are active in the multiplication process and that the secondary holes are not collected at the source. The possibility of reach-through can be eliminated because of the difference in the dependence of source and drain terminal currents on drain voltage.

Fig. (4.2) shows a plot of the log of the substrate current versus $(V_d - V_{ds})^{-1/2}$. It shows a good linear relationship in agreement with Eq. (2.16). This supports the assumption that the first order field approximation obtained from the one-dimensional solution of Poisson's

TABLE I

DEVICE PARAMETERS

| Device # | 32-L | 36-R | 38-L | 17-L | 18-L |
|---|------------------------|------------------------|------------------------|------------------------|-------------------------|
| Channel | N | N | N | P | P |
| Oxide Thickness | 3800 Å | 3800 Å | 4350 Å | 3500 Å | 3550 Å |
| Channel Length | 1 mil | 2 mil | 4 mil | 0.9 mil | 0.9 mil |
| Channel Width | 84.3 mil | 81.6 mil | 75.4 mil | 50 mil | 50 mil |
| Bulk Doping (cm ⁻³) | 3.7 x 10 ¹⁵ | 4.0 x 10 ¹⁵ | 4.1 x 10 ¹⁵ | 7.0 x 10 ¹⁶ | 6.6 x 10 ¹⁵ |
| Effective Gate Voltage | 1.1 V | 1.8 V | 2.8 V | 2.6 V | 2.75 V |
| Mobility (cm ² /V - sec) | 730 | 740 | 690 | 135 | 220 |
| Flat Band Voltage | 6.3 V | 5.3 V | 6.3 V | 4.5 V | 4.2 V |
| N _{ss} = Q _{ss} /q (cm ⁻²) | 2.0 x 10 ¹¹ | 2.3 x 10 ¹¹ | 2.6 x 10 ¹¹ | 2.0 x 10 ¹¹ | 1.95 x 10 ¹¹ |
| g _{do} | 1.38 m mho | 1.04 m mho | 0.642 m mho | 0.610 m mho | 0.835 m mho |
| $I_{EQ0} = \frac{2kT}{q} \frac{2}{3} g_{do}$ | 46 μA | 34 μA | 22 μA | 20 μA | 27 μA |

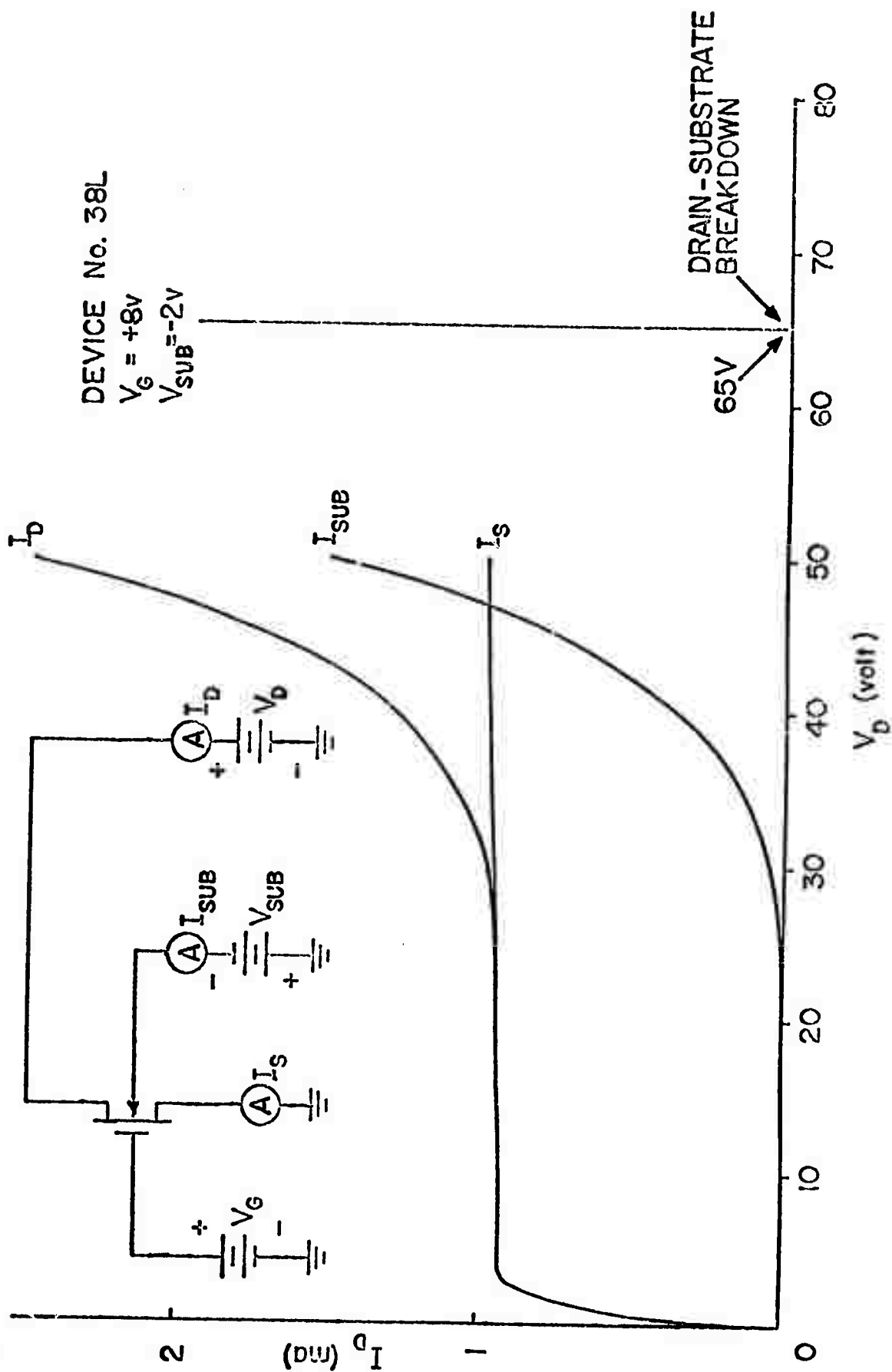


Figure 4.1--Typical Terminal Currents

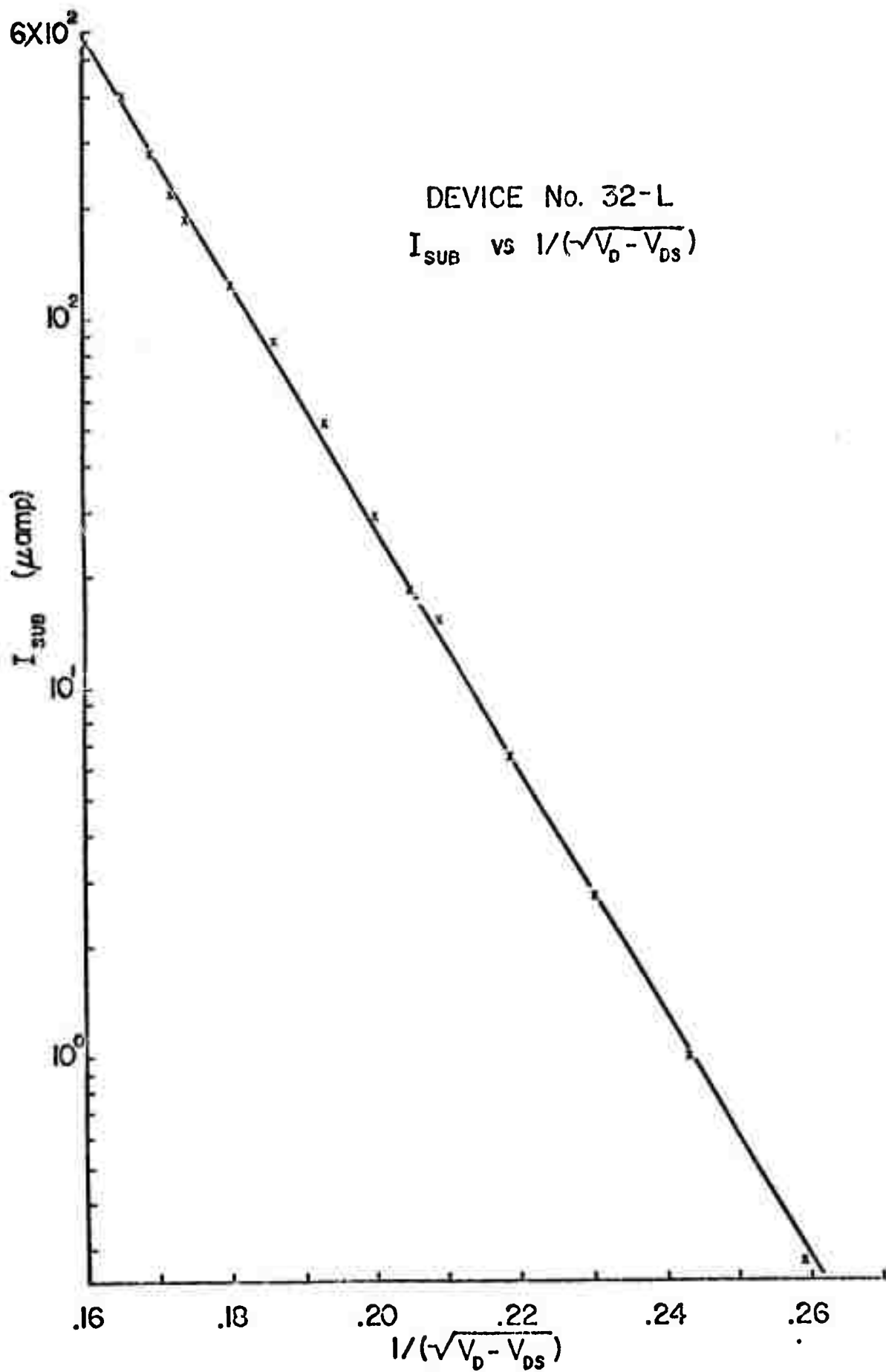


Figure 4.2--Substrate Current vs. $(V_D - V_{DS})^{-1/2}$

equation is adequate to estimate the magnitude of electric field in the CCD region for the study of avalanche phenomenon. It also supports the idea that the field dependence of the ionization rate in Eq. (2.10) is a good approximation even when surface scattering is involved. Eq. (2.10) was derived for the case where optical phonon scattering is mainly responsible for reducing the carrier energy obtained from the electric field. However, it seems to hold equally well when surface scattering is present.

The value of the average multiplication factor \bar{M} was determined from the ratio of the experimental values of the terminal currents as given in Eq. (2.3). The electric field at the drain junction, E_d , was determined with the help of Eq. (2.8) using appropriate device parameters. These data are plotted and presented in Figs. (4.3), (4.4) and (4.5). A semi-logarithmic scale is used so that these plots are really $\log_{10} (\ln \bar{M})$ versus E_d^{-1} .

The values of \bar{M} given by Eq. (2.15) were compared with these data. A computer program was used to determine the parameters A and B of Eq. (2.15) such that it will give least sum of square error between the two sets of values of \bar{M} . The points marked as "theoretical" are the results of that computer program.

Table II shows the values of the parameters A and B as determined from the procedure described above for both n- and p-channel devices. These values of A and B are used in Eq. (2.10) to calculate the ionization rates $\alpha(E)$ which are shown in Fig. (4.6).

It should be noted that the values of A and B obtained here differ considerably from those presented in the literature for avalanche ionization in bulk silicon.^{16, 17} To make clear the nature of this

TABLE II

IONIZATION RATE PARAMETERS

| Device # | 36-R | 36-L | 38-L | 32-L | 17-L | 18-L |
|--|--------------------|--------------------|--------------------|--------------------|-----------------------|--------------------|
| Channel | N | N | N | N | P | P |
| Channel Length | 2 mil | 4 mil | 4 mil | 1 mil | 1 mil | 1 mil |
| Effective Mobility ($\text{cm}^2/\text{V sec}$) | 740 | 611 | 687 | 732 | 135 | 220 |
| A (cm^{-1}) | 8.72×10^7 | 1.77×10^8 | 2.28×10^8 | 1.15×10^8 | 9.27×10^{10} | 1.55×10^9 |
| B (V/cm) | 2.53×10^6 | 2.68×10^6 | 2.54×10^6 | 2.46×10^6 | 1.04×10^7 | 6.04×10^6 |

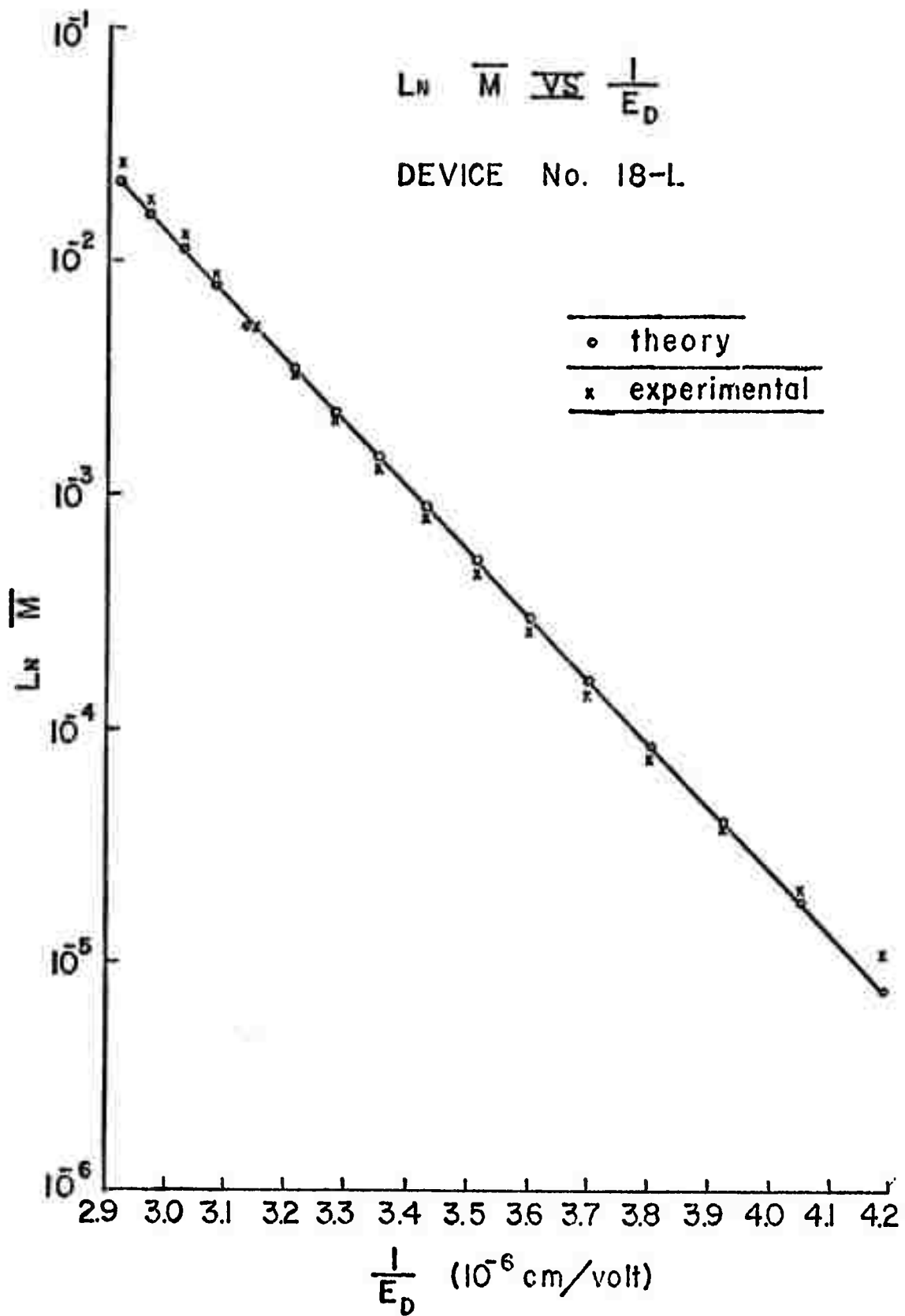


Figure 4.3-- $\ln \bar{M}$ vs. E_d^{-1} for Device 36-R

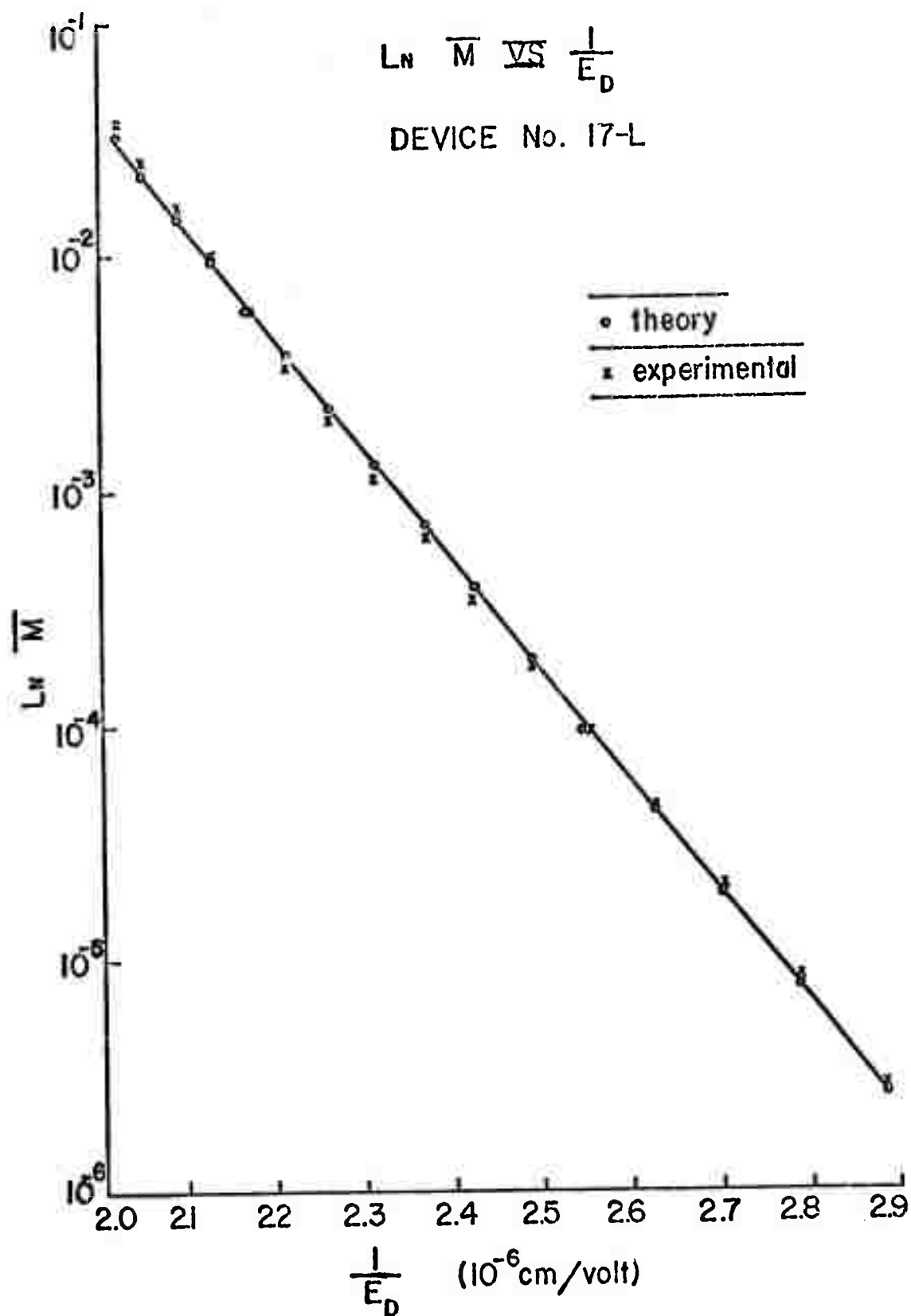


Figure 4.4-- $\ln \bar{M}$ vs. E_D^{-1} for Device 17-L

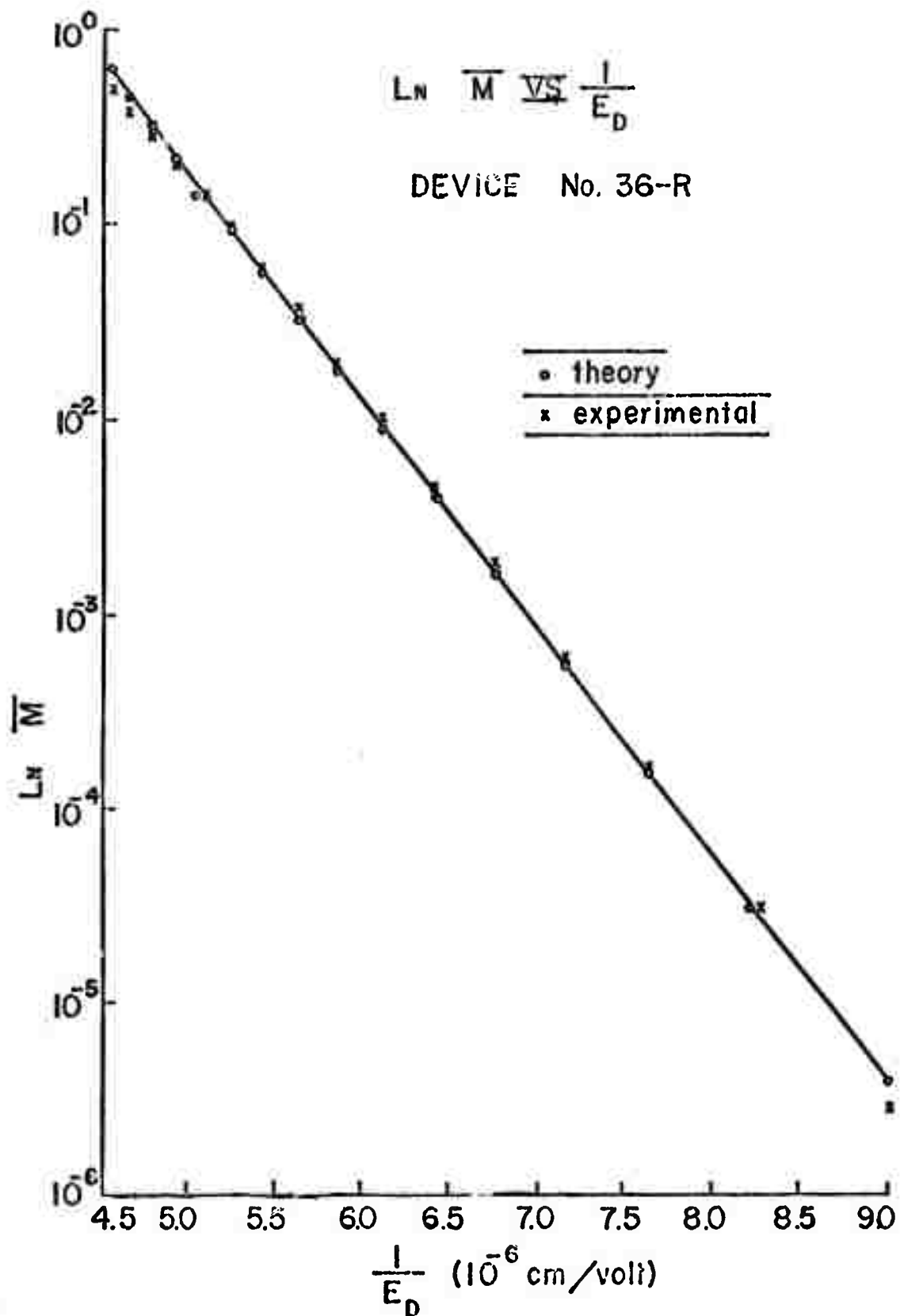


Figure 4.5-- $\ln \bar{M}$ vs. E_d^{-1} for Device 18-L

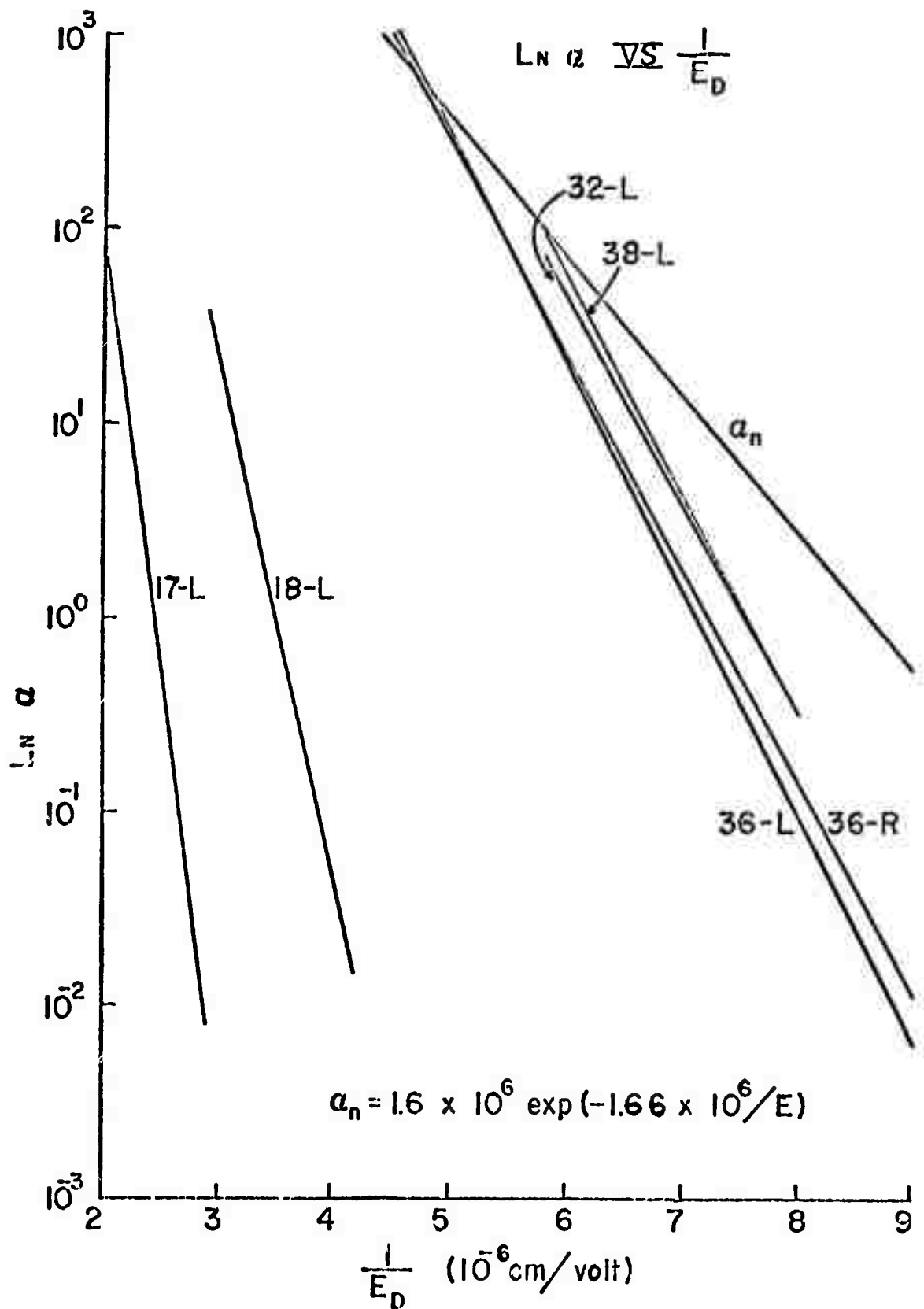


Figure 4.6--Ionization Rates vs. Electric Field

difference, Fig. (4.6) also shows a plot of the expression

$$\alpha(E) = 1.6 \times 10^6 \exp(-1.66 \times 10^6 / E) \quad (4.1)$$

which is accepted to be valid for electrons in bulk silicon.

That these differences exist is not surprising when one remembers that surface scattering is absent in the case of bulk silicon. Fig. (4.7) shows a plot of $\log B$ versus $\log \mu_{\text{eff}}$ for the devices of Table II. This plot suggests a strong correlation between the two quantities. The slope corresponding to

$$B \propto \mu_{\text{eff}}^{-1} \quad (4.2)$$

is also shown for comparison.

This result is reasonable since the lower the effective mobility, the higher the electric field required for the kinetic energy of electrons to exceed the threshold energy of avalanche ionization.

Drain current noise was measured at three different drain bias values. Typical spectra are shown in Figs. (4.8) and (4.9). The theoretical limiting value of the thermal noise, given by $(2/3) 4kT g_{\text{do}}$, is shown in the lower right corner. At a drain voltage of 5 volts there was negligible substrate current, which implied the absence of the avalanche multiplication. As is common in MOSFET's the flat portion of the spectrum at $V_d = 5$ volts is above the limiting value of $I_{\text{eqo}} = (2/3) 4kT g_{\text{do}}$. The excess noise may be due to one or more of the following causes:

- a) the effect of ionized bulk impurities,^{18, 19}
- b) white noise of non-thermal origin operating in the channel,²⁰ or
- c) hot electron effect.²¹

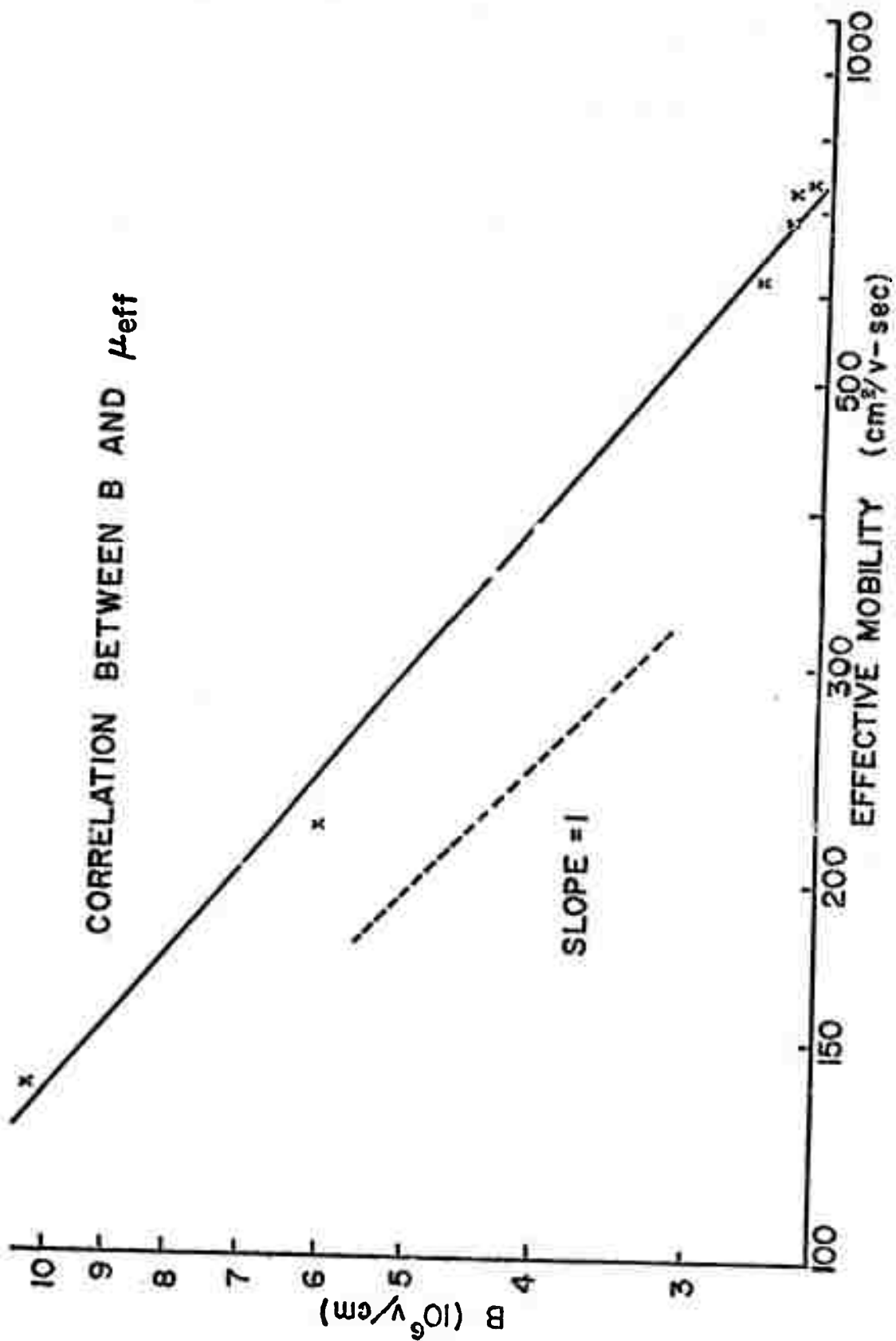


Figure 4.7--Correlation Between Effective Mobility and Parameter B

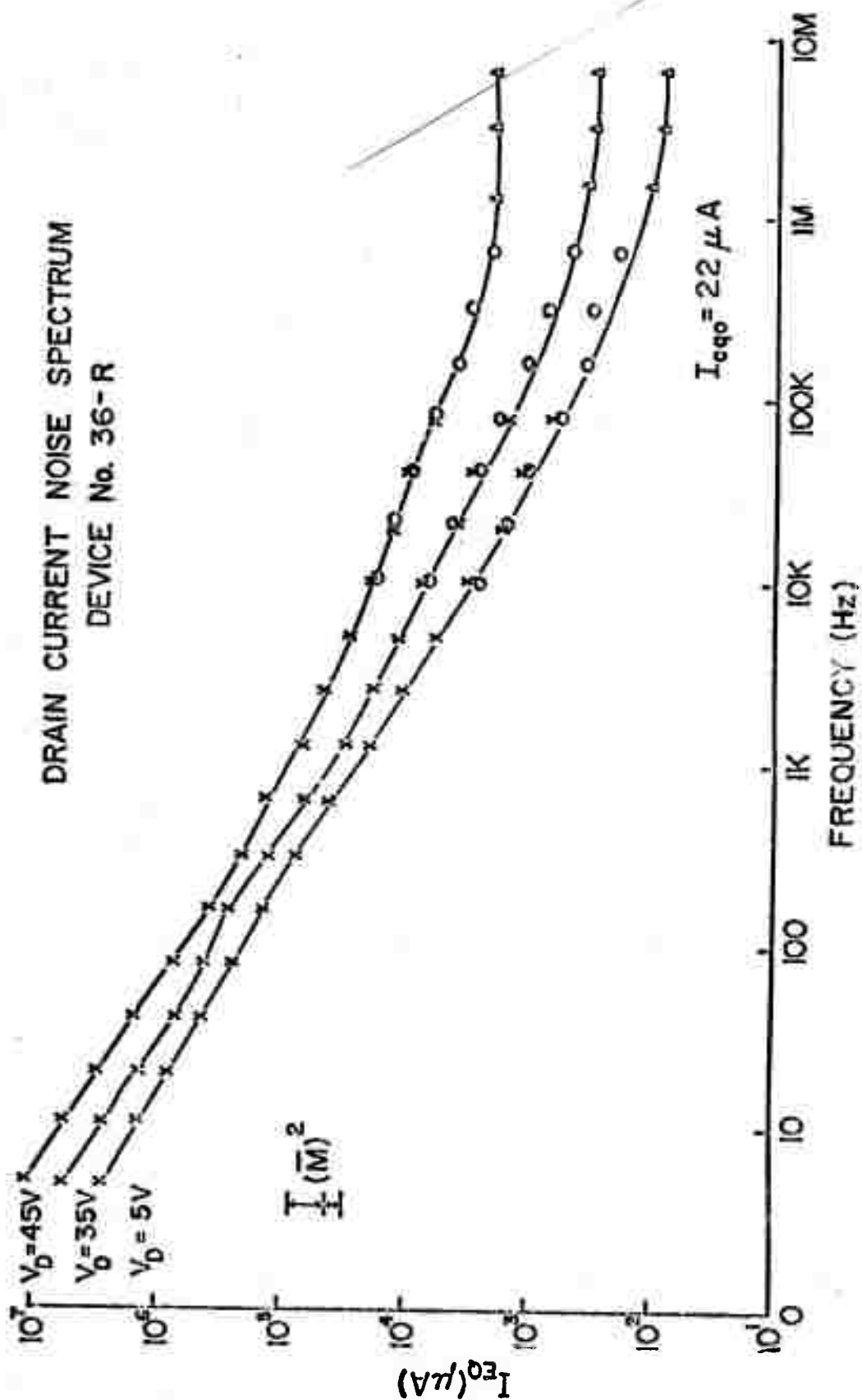


Figure 4.8--Noise Spectra for Device 36-R

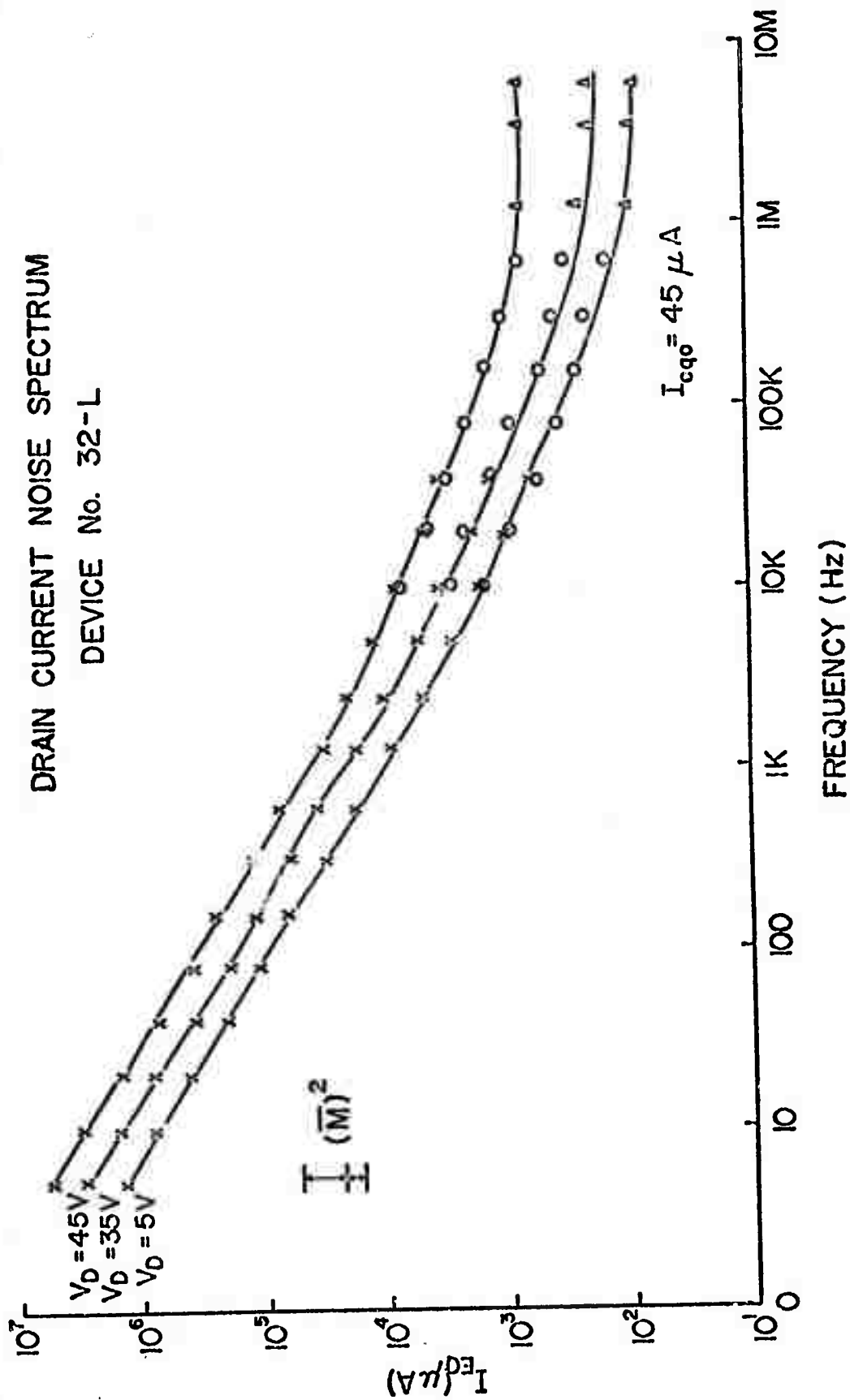


Figure 4.9--Noise Spectra for Device 32-L

In the upper left hand corner of these figures the factor of $(\bar{M})^2$ is shown. \bar{M} was determined from terminal currents as described earlier. It is seen that the $1/f$ spectrum at different drain voltages varies by the factor $(\bar{M})^2$. However the high frequency spectrum tends to vary as $I_{\text{sub}} \bar{M}$. This is in agreement with Eq. (2.33) which is presented again below.

$$I_{\text{eqd}}(f) = I_{\text{eqs}}(f) (\bar{M})^2 + I_{\text{sub}} \bar{M} \quad (4.3)$$

At the lower frequency end of the spectrum the thermal noise component of I_{eqs} is buried underneath the flicker noise component, and the first term of Eq. (2.33) predominates. Therefore the drain current noise in the flicker region of the spectrum can be approximated as $I_{\text{eqs}} (\bar{M})^2$. At the high frequency end of the spectrum I_{eqs} consists mainly of the thermal noise component. If high drain bias makes the substrate current larger than I_{eqs} in the thermal noise region, the second term predominates.

These points appear to be more obvious when the drain current noise at different frequencies is measured as a function of drain bias. Fig. (4.10) shows the results of the measurement on device # 36-R. In this figure the variation of $(\bar{M})^2$ and of $I_{\text{sub}} \bar{M}$ with drain bias are also plotted for comparison. The low frequency noise follows the shape of the $(\bar{M})^2$ variation whereas the high frequency noise varies as the $I_{\text{sub}} \bar{M}$ curve. This is an evidence that Eq. (4.3) properly describes the drain current noise when avalanche ionization is present in the CDD region of a MOSFET.

Further evidence of the validity of the noise model is presented by the data of Figs. (4.11) and (4.12) which show both drain noise and

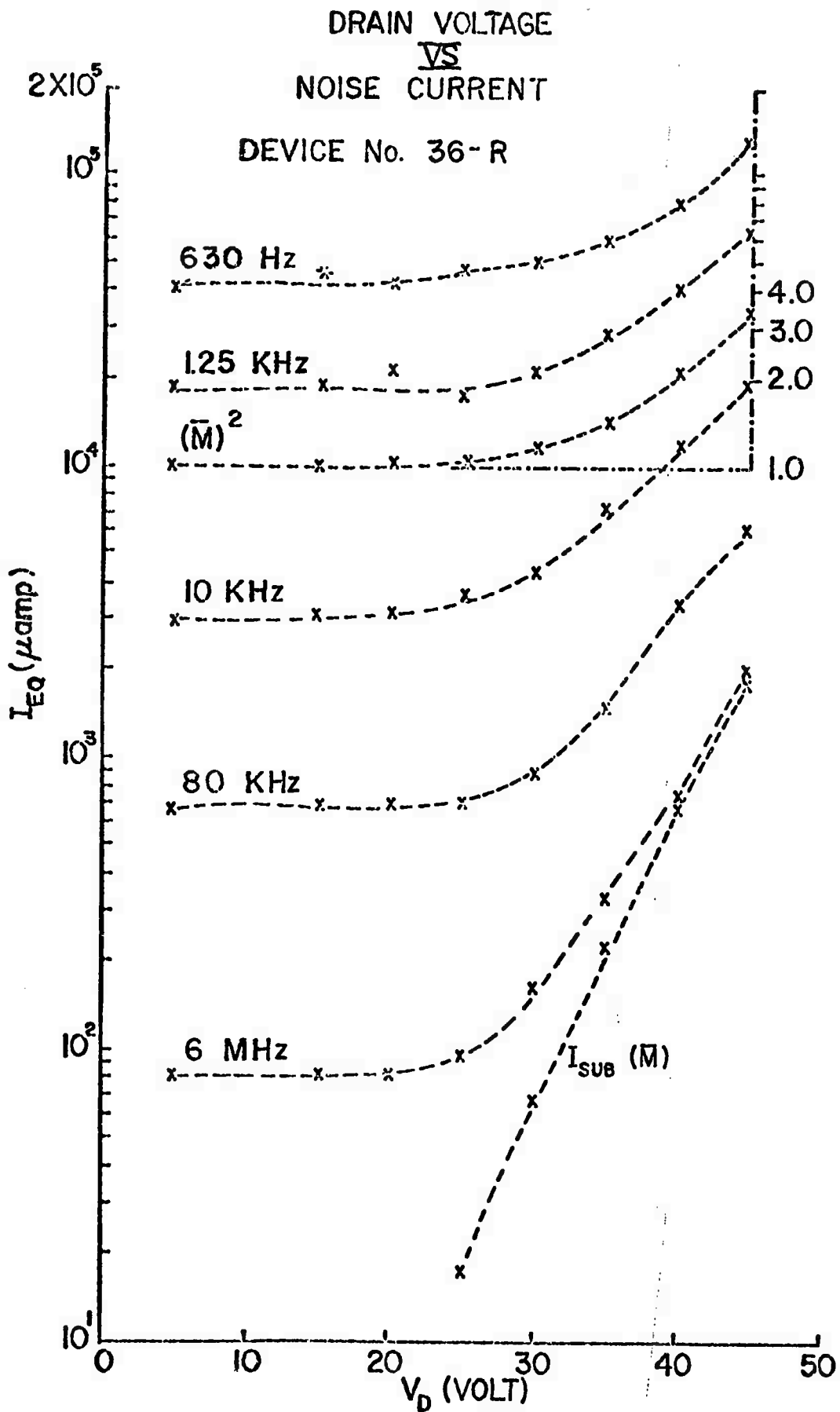


Figure 4.10--Noise vs. Drain Bias at Different Frequencies

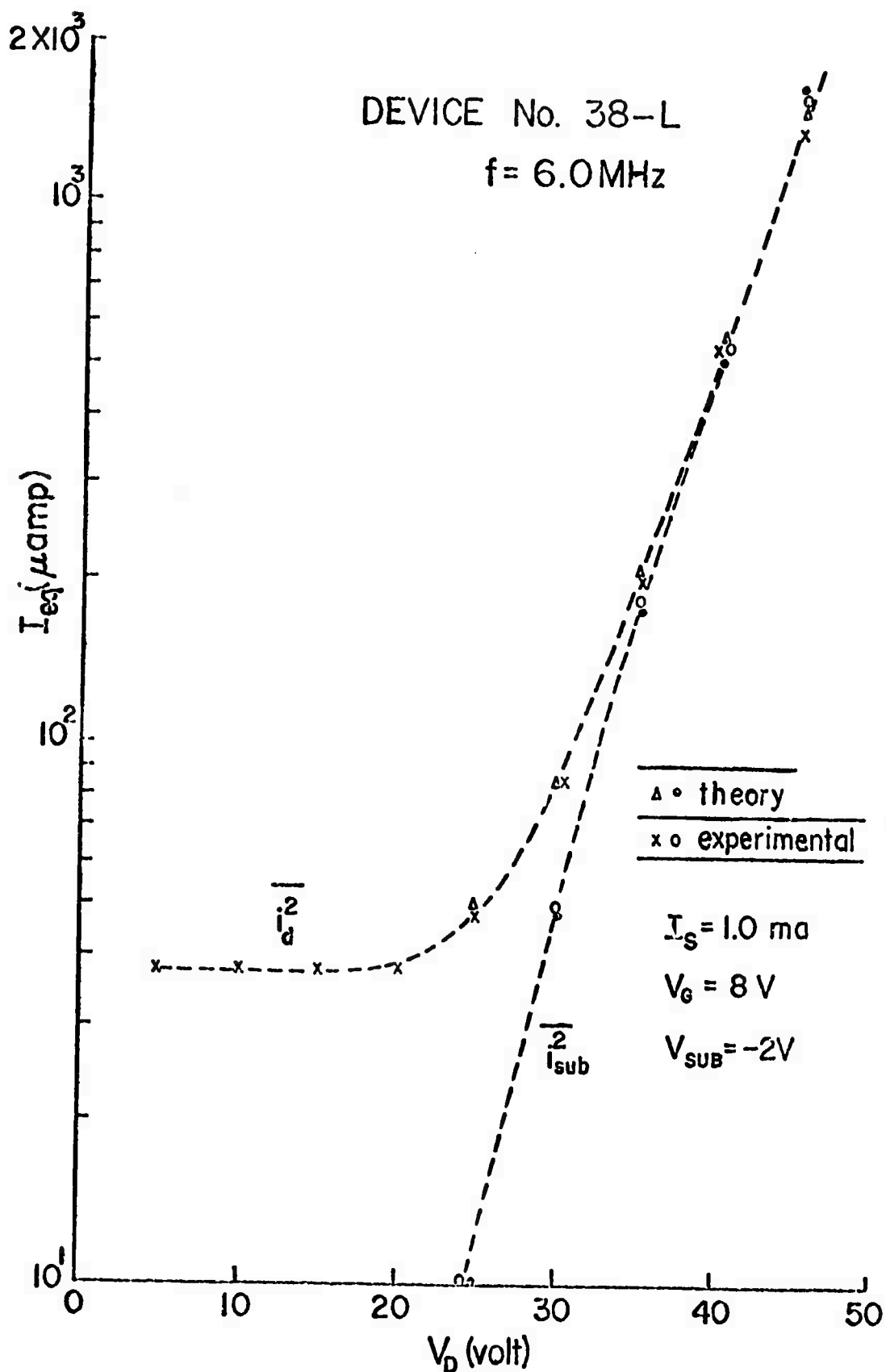


Figure 4.11--Noise vs. Drain Bias at 6 MHz, Device 38-L

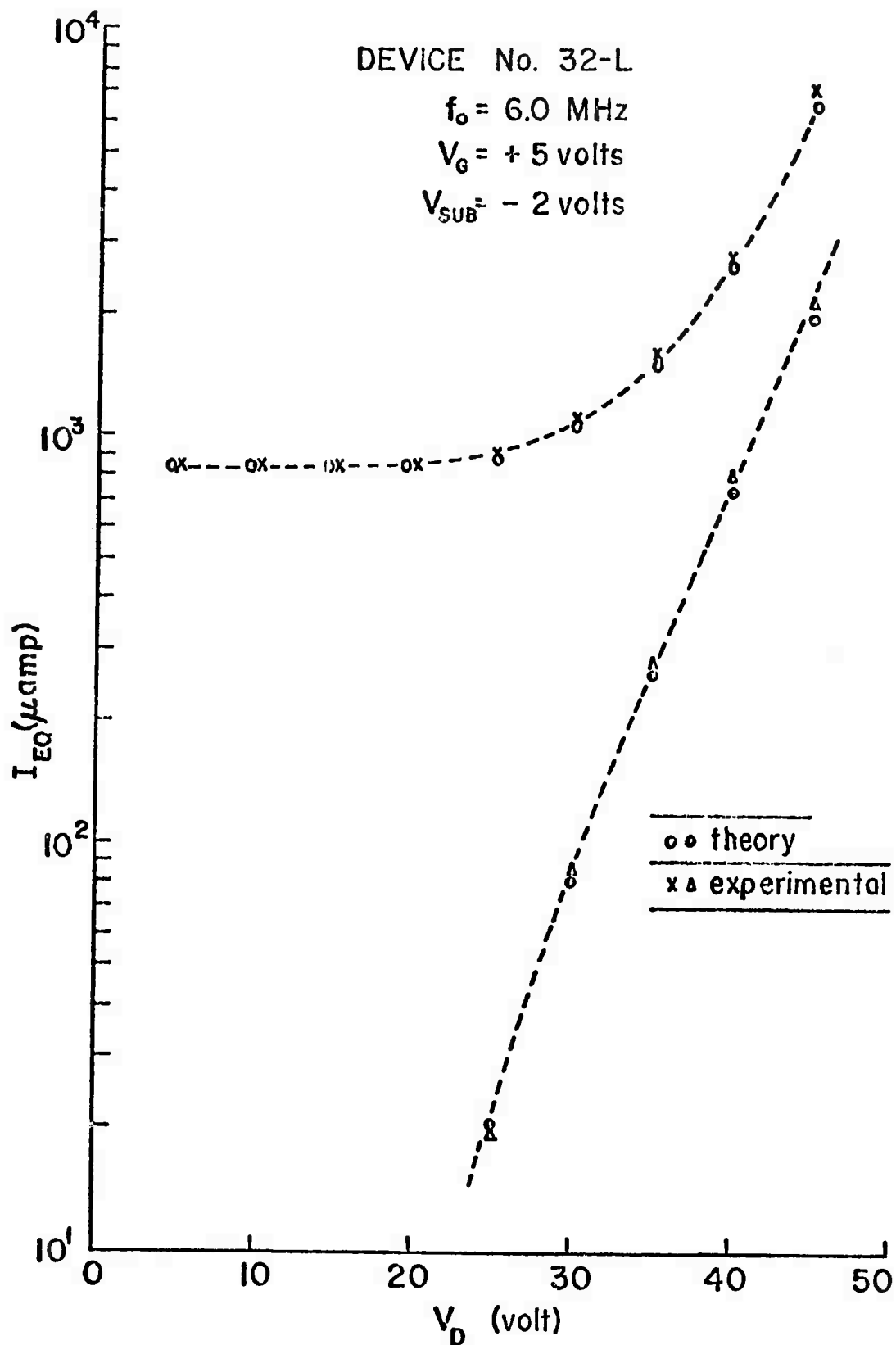


Figure 4.12--Noise vs. Drain Bias at 6 MHz, Device 32-L

substrate noise currents as a function of drain bias. At high drain bias voltages these two noise currents approach the same value of $I_{\text{sub}} \bar{M}$. Theoretical values of i_d^2 and i_{sub}^2 obtained from Eqs. (2.33) and (2.34) are shown on all these figures to emphasize the excellent agreement with experiment.

The noise measurements were repeated with the FET in common substrate connection with the gate a.c. grounded and a high-impedance in the source lead. Fig.(4.13) shows the data in the same way as Figs.(4.11) and (4.12). Again there is good agreement with them. As discussed in Chapter III this is experimental proof that the substrate current noise and the drain current noise are fully correlated in avalanche multiplication.

In general the quantitative model derived in Chapter II describes the avalanche multiplication noise in FET's with good accuracy. However, there are certain possibilities which might cause discrepancies. These possibilities are listed below.

a) At high current densities it is possible that a certain portion of the secondary holes are not scattered out of the CDD region but are collected back at the source terminal. The rise of the source terminal current at the far end of the drain bias in Device # 35-L might indicate this possibility. See Fig. (4.14). Other units did not show this.

b) As the CDD region is driven into higher fields it becomes possible that the field induced localized breakdown around chemical impurity sites and local defect sites will contribute to extra low frequency noise. We have no conclusive evidence for this mechanism.

The accuracy of Eqs. (2.33) and (2.34) verified experimentally does, together with the facts established from the d.c. terminal current

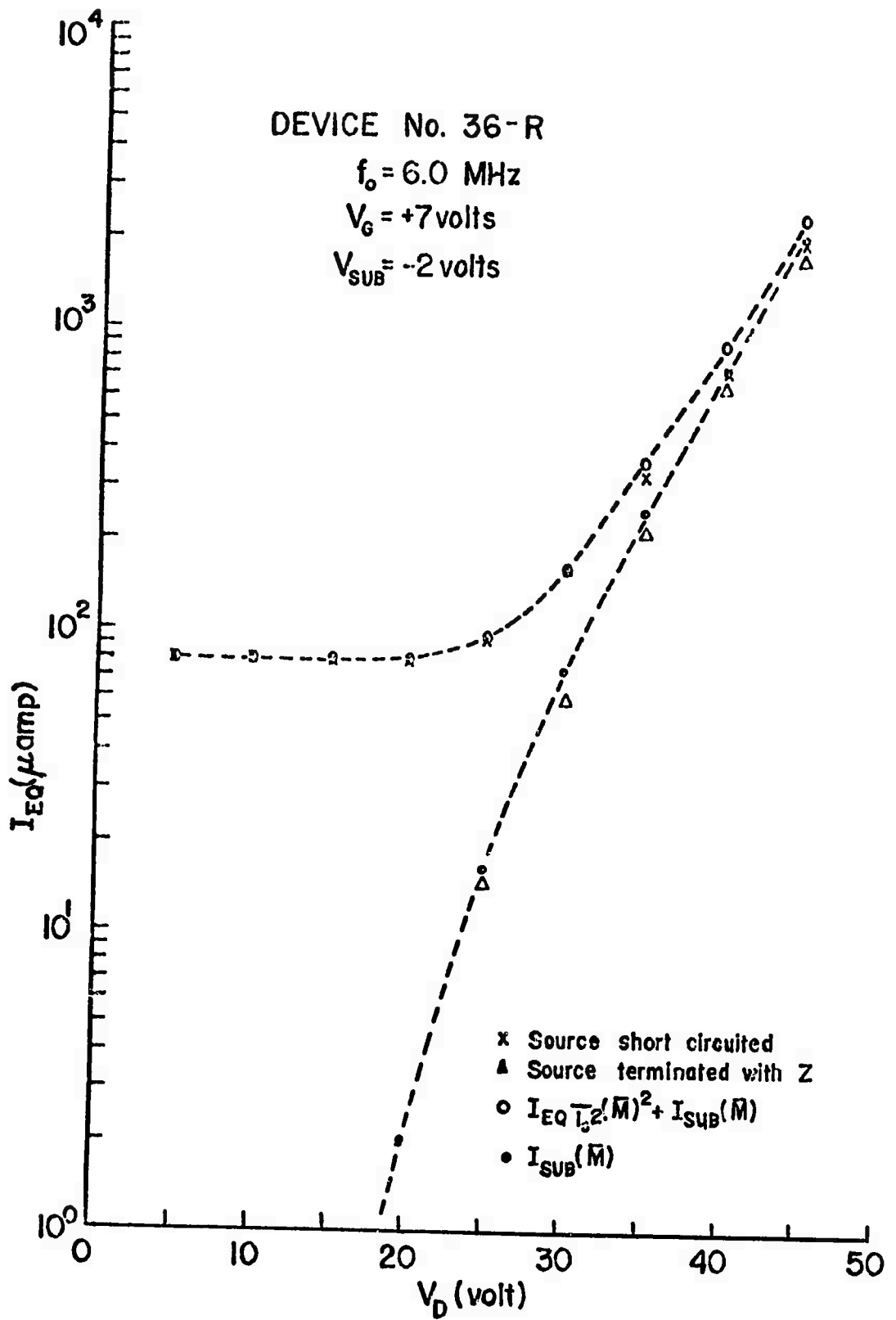


Figure 4.13--Noise vs. Drain Bias at 6 MHz, Device 36-R

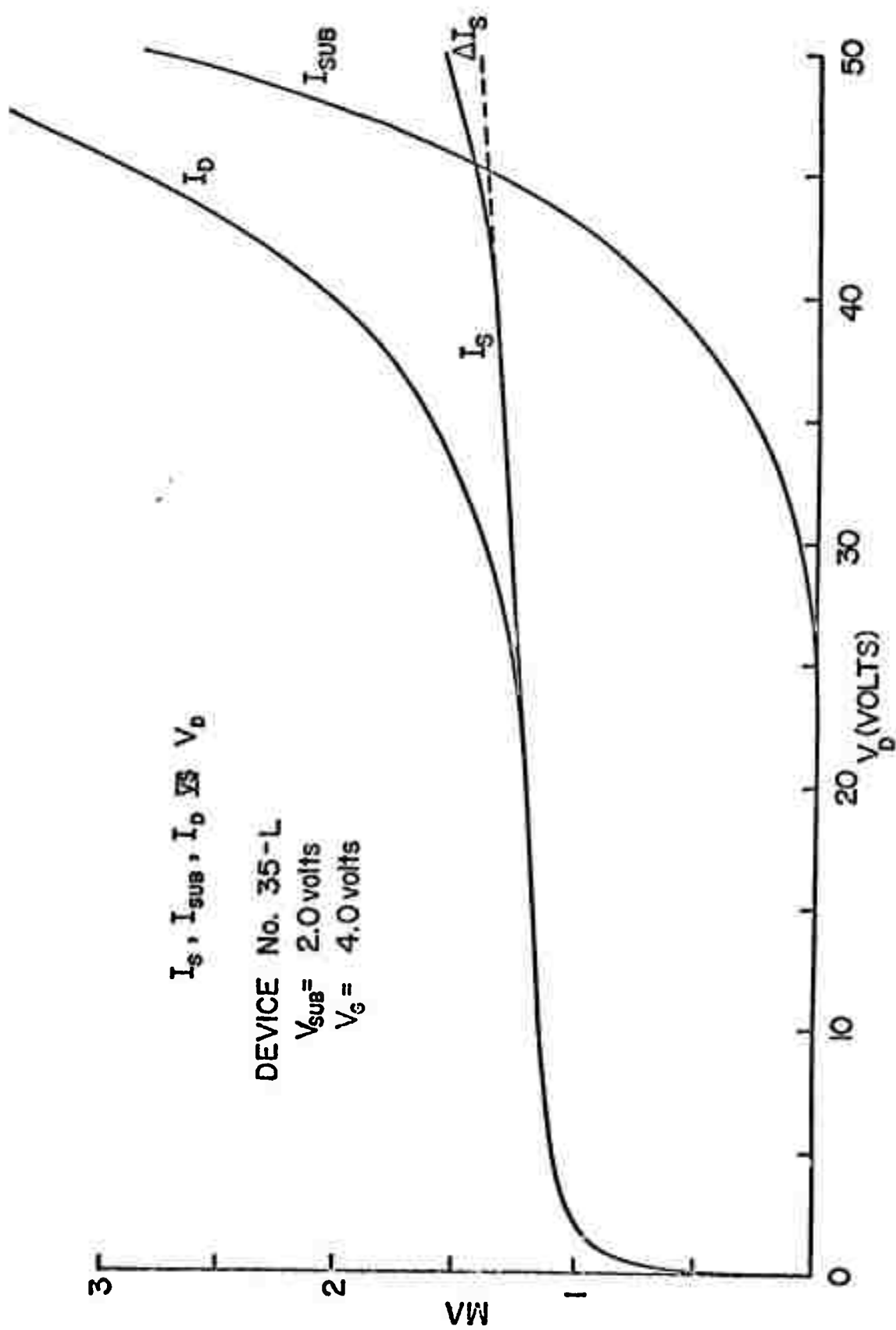


Figure 4.14---Terminal Currents vs. Drain Bias, Device 35-L

measurements, prove that only one type of carrier is active in the avalanche multiplication process. If both types of carriers had gone through the avalanche multiplication, the noise resulting from the random fluctuation of avalanche multiplication should have been much larger than the magnitudes predicted by these equations.

V CONCLUSIONS AND RECOMMENDATIONS

In this work, a detailed study of the avalanche multiplication phenomena in the CDD region of an MOSFET has been carried out. The present chapter summarizes the important results obtained and discusses several areas which deserve further study.

Experiments were performed on both n-channel and p-channel silicon MOSFET's fabricated for this study. The experimental results were compared with the theoretical study on the avalanche current and associated noise. The following conclusions are drawn.

- 1) Experimental evidence is established for the presence of avalanche ionization in the CDD region of a MOSFET, when the drain is biased far beyond saturation.

- 2) Only one type of current carrier (electrons in n-channel devices and holes in p-channel devices) is active in the avalanche multiplication process in FET's. The minority carriers generated from the avalanche multiplication are removed from the CDD region and collected at the substrate terminal. Both the terminal current measurement and noise measurement substantiate this fact.

- 3) The noise magnitude associated with the avalanche multiplication in MOSFET's can be described with accuracy by the following two equations derived.

$$I_{eqd} = I_{eqs} (\bar{M})^2 + I_{sub} \bar{M} \quad (5.1)$$

$$I_{eqsub} = I_{eqs} (\bar{M} - 1)^2 + I_{sub} \bar{M} \quad (5.2)$$

4) The first order approximation for the electric field intensity in the CDD region obtained from the one-dimensional solution of Poisson's equation provides sufficiently accurate estimation of field intensity for the study of avalanche phenomena.

5) The field dependence of ionization rates in MOSFET's is accurately described by

$$\alpha(E) = A \exp (-B/E)$$

where A and B are constants for the following range of electric field investigated.

electron: 1.0×10^5 volt/cm to 3.0×10^5 volt/cm

hole: 2.0×10^5 volt/cm to 5.0×10^5 volt/cm

The value of parameters A and B determined differs somewhat from the bulk silicon case and shows a strong correlation with surface scattering.

1) Eqs. (5.1) and (5.2) should also be valid expressions for the avalanche current noise in Junction FET's. The substrate current and noise have to be replaced by the gate current and noise, respectively. These equations deserve an experimental verification for Junction FET case.

2) At low temperatures the avalanche multiplication phenomenon is expected to be more appreciable. The extension of present work to low temperatures would add to present knowledge.

3) In Chapter IV the correlation between the parameter B and the effective mobility was discussed. A further study leading to a quantitative relationship between the parameters A, B and other device parameters is recommended. As a matter of fact if this quantitative relation can be obtained, the avalanche current measurement will provide a new method of measuring the effective mobility. Previous measurements of effective mobility were mostly done by measuring the channel conductance.

4) Expecting that at low temperatures or in a short channel device the avalanche multiplication noise will be significant, a study of a circuit which will minimize this noise deserves immediate attention. As discussed in the chapter on experimental method the common substrate configuration can be less noisy than common source configuration.

APPENDIX I

CALCULATION OF THE VARIANCE OF THE MULTIPLICATION FACTOR M

Assume that the ionization events are independent events whose occurrence is equally probable at any point along the path of length d . Then the probability of having m ionization events along the path d is given by Poisson's distribution;

$$P_m = \frac{u^m}{m!} \exp(-u) \quad (A-1.1)$$

where $u = \bar{\alpha}d$ is the average number of ionization events and $\bar{\alpha}$ is the average ionization rate per unit length. Obviously the probability of having no ionization events along any fixed length l is given by

$$P_0(l) = \exp(-\bar{\alpha}l) \quad (A-1.2)$$

The probability density of path length between two successive ionization events has an exponential distribution as a corollary of Poisson's law. Hence, the probability of having an ionization event at a point between y and $y + dy$ (assuming the last ionization event at $y=0$) can be written as

$$f(y) dy = \bar{\alpha} \exp(-\bar{\alpha}y) dy \quad (A-1.3)$$

Defining $P(M)$ as the probability of M particles emerging at the drain terminal, we have

$$P(1) = P_0(d) = \exp(-\mu) \quad (A-1.4)$$

Suppose only one ionization event occurs at $y = y'$. Refer to Fig. (A-1). Then from Eq. (A-1.3) the probability of the particular ionization event being located at y' is

$$f(y') = \bar{\alpha} \exp (-\bar{\alpha} y') \quad (\text{A-1.5})$$

Therefore the probability of two particles emerging at the drain terminal due to one ionizing collision event located at y' is

$$dP(2)_{y'} = \underset{(a)}{f(y')} \underset{(b)}{p_0(d-y')} \underset{(c)}{p_0(d-y')} dy' \quad (\text{A-1.6})$$

where (a), (b), etc. indicate the particular paths involved. $P(d-y')^2$ accounts for the fact that two particles cover a distance of $d-y'$ without going through another ionization. The ionization event which we assumed to occur at y' can happen anywhere along the path. Thus integrating over the total distance of d , we get

$$P(2) = \int_0^d dP(2)_{y'}$$

$$= \int_0^d \bar{\alpha} \exp (-\bar{\alpha} y') \exp [-\bar{\alpha}(d-y')]^2 dy'$$

$$= \bar{\alpha} \exp (-2 \bar{\alpha} d) \int_0^d \exp (\bar{\alpha} y') dy'$$

$$= \exp (-2u) [\exp (u) - 1] \quad (\text{A-1.7})$$

Now in order to have three particles emerging at the drain terminal, two ionization event should occur somewhere along the path. There are two possible ways in which this can happen, as indicated in Fig. (A-2). Case I is when the primary particle goes through two successive ionizing collisions; Case II is when the primary and the first secondary particle each go through one ionizing collision. In a similar way as in the

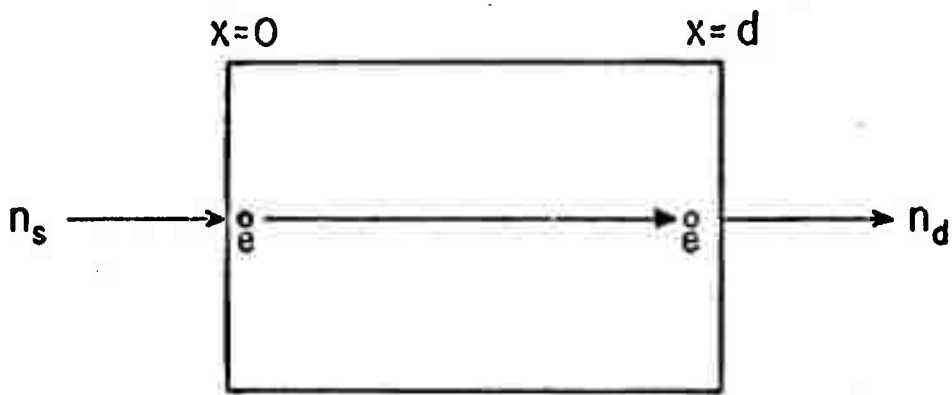


ILLUSTRATION FOR P(1) (NO IONIZING COLLISIONS)

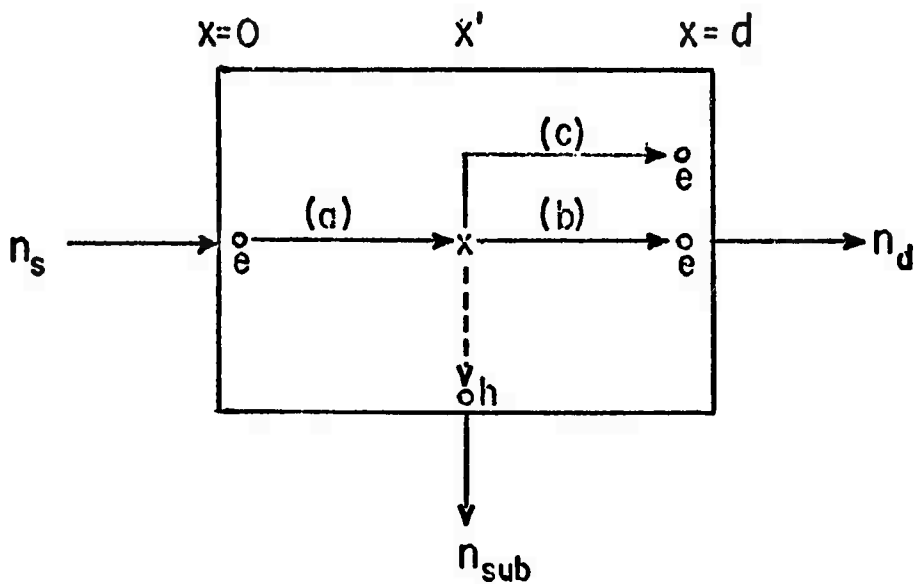


ILLUSTRATION FOR P(2) (ONE IONIZING COLLISION)

Figure A-1--Illustration for P(1) and P(2)

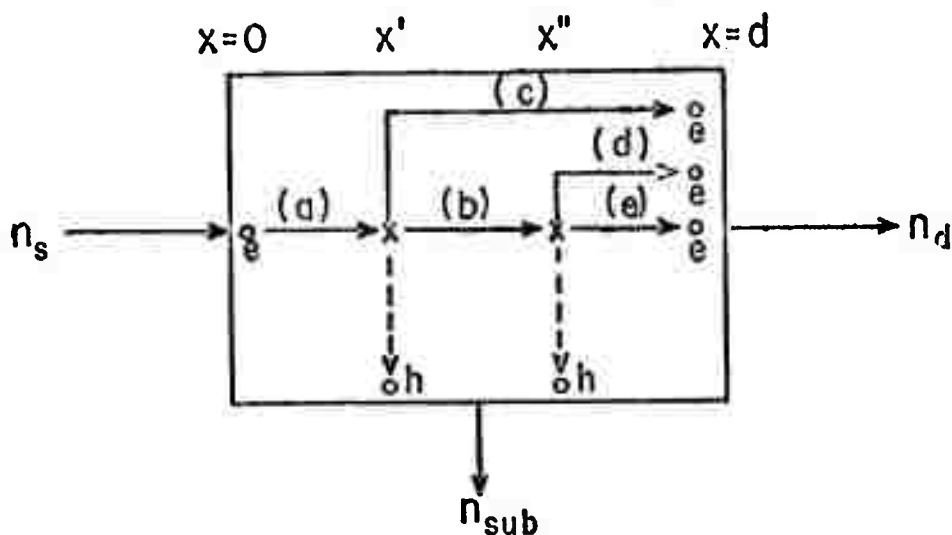


ILLUSTRATION FOR $P(3)$ <CASE I>
(TWO IONIZING COLLISIONS)

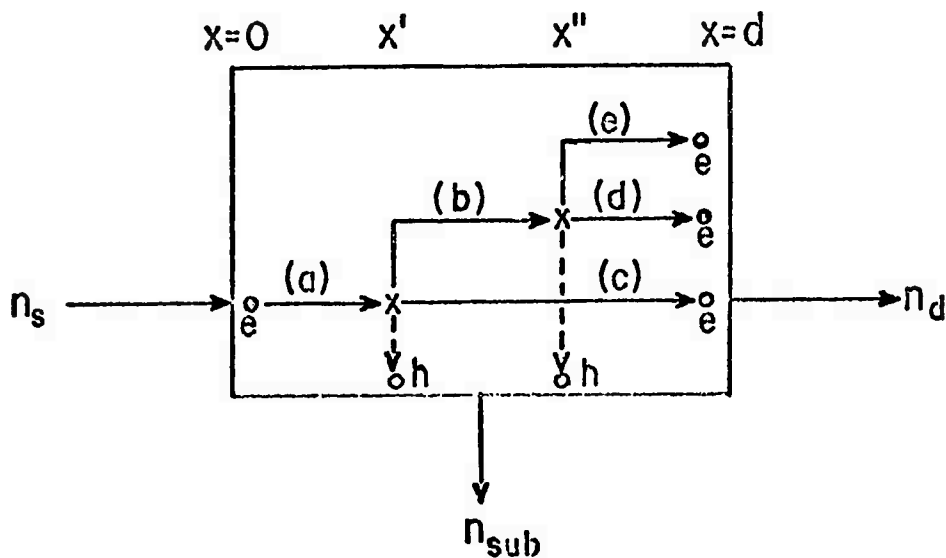


ILLUSTRATION FOR $P(3)$ <CASE II>
(TWO IONIZING COLLISIONS)

Figure A-2--Illustration for $P(3)$, Case I and Case II

P(2) calculation, we have for Case I

$$dP(3)_{y', y''} = \underset{(a)}{f(y')} \underset{(b)}{f(y'' - y')} \underset{(c)}{P_0(d - y')} \underset{(d)}{P_0(d - y'')} \underset{(e)}{P_0(d - y'')} \quad (A-1.8)$$

For Case II, we have the same form of

$$dP(3)_{y', y''} = \underset{(a)}{f(y')} \underset{(b)}{f(y'' - y')} \underset{(c)}{P_0(d - y')} \underset{(d)}{P_0(d - y'')} \underset{(e)}{P_0(d - y'')} \quad (A-1.9)$$

Since both the first and second ionizing collision can occur anywhere along the path as far as they occur in succession, we have to integrate by dy' and dy'' over the entire length of d .

$$\begin{aligned} P(3) &= \int_0^d \int_0^d dP(3) dy' dy'' \\ &= \int_0^d f(y') P_0(d - y') \left\{ \int_{y'}^d f(y'' - y) P_0(d - y'')^2 dy'' \right\} dy' \\ &= \int_0^d [\bar{\alpha} \exp(-\bar{\alpha} y')] \exp[-\bar{\alpha}(d - y')] \int_{y'}^d \bar{\alpha} \exp[-\bar{\alpha}(y'' - y')] \\ &\quad \exp[-\bar{\alpha}(d - y'')]^2 dy'' dy' \\ &= \int_0^d \exp(-2\bar{\alpha}d) \exp(\bar{\alpha} y') [\exp(\bar{\alpha} - d) - \exp(\bar{\alpha} - y')] dy' \\ &= 1/2 \exp(-3\mu) [\exp(u) - 1]^2 \end{aligned} \quad (A-1.10)$$

Following the same reasoning, we can go on calculating $P(4)$, $P(5)$ and so on. Summarizing the results we can write in general

$$P(M) = C_M \exp(-Mu) [\exp(u) - 1]^{M-1} \quad (A-1.11)$$

where C_M is a constant number.

The sum of $P(M)$ for all the possible value of M gives the normalization of the probability density $P(M)$.

$$\sum_{M=1}^{\infty} P(M) = 1 \quad (A-1.12)$$

Differentiating both sides of Eq. (A-1.12) with respect to u gives

$$\frac{\partial}{\partial u} \left[\sum_{M=1}^{\infty} P(M) \right] = \sum_{M=1}^{\infty} \frac{\partial}{\partial u} [P(M)] = 0 \quad (A-1.13)$$

Substituting Eq. (A-1.11) into (A-1.13) we have

$$\begin{aligned} \sum_{M=1}^{\infty} \frac{\partial}{\partial u} [P(M)] &= \sum_{M=1}^{\infty} P(M) \{ (M-1) \exp(u) [\exp(u) - 1]^{-1} - M \} \\ &= \sum_{M=1}^{\infty} P(M) (-M) + \exp(u) [\exp(u) - 1]^{-1} \sum_{M=1}^{\infty} P(M) M \\ &\quad - \sum_{M=1}^{\infty} P(M) M - \exp(u) [\exp(u) - 1]^{-1} \sum_{M=1}^{\infty} P(M) = 0 \end{aligned} \quad (A-1.14)$$

Now \bar{M} and $\overline{M^2}$ can be defined as

$$\begin{aligned} \bar{M} &= \sum_{M=1}^{\infty} P(M) M \\ \overline{M^2} &= \sum_{M=1}^{\infty} P(M) M^2 \end{aligned} \quad (A-1.15)$$

Combining Eq. (A-1.14) and (A-1.15) we have

$$\begin{aligned} \bar{M} &= \exp(u) [\exp(u) - 1]^{-1} \bar{M} - \exp(u) [\exp(u) - 1]^{-1} \\ &= \exp(u) \end{aligned} \quad (A-1.16)$$

Differentiating both sides of Eq. (A-1.16) again with respect to u , we have

$$\begin{aligned} \frac{\partial}{\partial u} \bar{M} &= \frac{\partial}{\partial u} \left[\sum_{M=1}^{\infty} P(M) M \right] \\ &= \sum_{M=1}^{\infty} M \frac{\partial}{\partial u} P(M) \\ &= \exp(u) [\exp(u) - 1]^{-1} \sum_{M=1}^{\infty} P(M) M (M-1) - \sum_{M=1}^{\infty} M^2 P(M) \\ &= \exp(u) \end{aligned} \quad (A-1.17)$$

Substituting Eq. (A-1.16) into the above, we get

$$\begin{aligned}\overline{M^2} &= 2 \exp(2u) - \exp(u) \\ &= 2(\overline{M})^2 - \overline{M}\end{aligned}\tag{A-1.18}$$

Hence,

$$\begin{aligned}\text{Var } M &= \overline{M^2} - (\overline{M})^2 \\ &= \overline{M} (\overline{M} - 1)\end{aligned}\tag{A-1.19}$$

APPENDIX II

CALCULATION OF $\overline{i_{sub}^2}$ AND $\overline{i_d i_{sub}^*}$

The number of secondary particles emerging out of the substrate terminal, n_{sub} , can be written as

$$n_{sub} = n_d - n_s$$

$$= \sum_{i=1}^{n_s} M_i - n_s$$

$$= \sum_{i=1}^{n_s} (M_i - 1) \quad (A-2.1)$$

where n_d and n_s are the number of particles emerging out of the drain terminal and the number of particles entering from the source terminal respectively. Applying the variance theorem, we have

$$\text{Var } n_{sub} = (\bar{M} - 1)^2 \text{Var } n_s + \bar{n}_s \text{Var } M \quad (A-2.2)$$

Hence,

$$\begin{aligned} S_{i_{sub}}(0) &= q^2 \text{Var } n_{sub} \\ &= 2q^2 [(\bar{M} - 1)^2 \text{Var } n_s + \bar{n}_s \text{Var } M] \end{aligned} \quad (A-2.3)$$

Expressing the above equation in terms of equivalent noise diode current, we have

$$I_{eqsub} = I_{eqs} (\bar{M} - 1)^2 + I_{sub} \bar{M} \quad (A-2.4)$$

where the result of Eq. (A-1.19) is also used.

For the correlated part, we can write

$$\begin{aligned}
 \text{Var } (n_d n_{\text{sub}}) &= \overline{n_d n_{\text{sub}}^*} - \overline{n_d} \overline{n_{\text{sub}}} \\
 &= \overline{\left(\sum_{i=1}^{n_s} M_i \right) \left[\sum_{j=1}^{n_s} (M_j - 1) \right]^*} - (\overline{n_s} \overline{M}) [\overline{n_s} (\overline{M} - 1)] \\
 &= \overline{\sum_{i=1}^{n_s} \sum_{j=1}^{n_s} M_i (M_j - 1)^*} - (\overline{n_s})^2 \overline{M} (\overline{M} - 1) \\
 &= \overline{n_s (n_s - 1) \overline{M} (\overline{M} - 1)} + \overline{n_s} (\overline{M}^2 - \overline{M}) - (\overline{n_s})^2 \overline{M} (\overline{M} - 1) \\
 &= [\overline{n_s}^2 - (\overline{n_s})^2] \overline{M} (\overline{M} - 1) + \overline{n_s} [\overline{M}^2 - (\overline{M})^2] \\
 &= \text{Var } n_s \overline{M} (\overline{M} - 1) + \overline{n_s} \text{Var } M
 \end{aligned} \tag{A-2.5}$$

Hence,

$$\begin{aligned}
 S_{i_d i_{\text{sub}}} (0) &= q^2 2 \text{Var } (n_d n_{\text{sub}}) \\
 &= 2q^2 [\overline{M} (\overline{M} - 1) \text{Var } n_s + \overline{n_s} \text{Var } M]
 \end{aligned} \tag{A-2.6}$$

Again expressing the above in terms of equivalent saturated noise diode current, we have

$$I_{\text{eqdsub}} = I_{\text{eqs}} \overline{M} (\overline{M} - 1) + I_{\text{sub}} \overline{M} \tag{A-2.7}$$

REFERENCES

1. E. S. Schlegel, "A Bibliography of Metal-Insulator-Semiconductor Studies." IEEE Trans., ED-14, #11, pp. 728-749, November, 1967
2. E. S. Schlegel, "Additional Bibliography of Metal-Insulator-Semiconductor Studies." IEEE Trans., ED-15, #12, pp. 951-952,
3. William E. Sayle, II, and Peter O. Lauritzen, "Avalanche Ionization Rates Measured in Silicon and Germanium at Low Electric Fields." IEEE Trans., ED-18, #1, pp. 58-66, January, 1971
4. R. D. Ryan, "The Gate Current of Junction Field-Effect Transistors at Low Temperatures." Proc. IEEE (Lett), V 57, pp. 1225-1226,
5. F. M. Klaassen and J. R. Robinson, "Anomalous Noise Behavior of Junction-Gate Field Effect Transistor at Low Temperature." IEEE Trans., ED-17, pp. 852-857, October, 1970.
6. M. Nakahara, H. Iwasawa, and K. Yasutake, "Anomalous Enhancement of Substrate Terminal Current Beyond Pinch-Off in Silicon N-Channel MOS Transistor." Electronics & Communication in Japan, V 52-C, #3, pp. 173-180, 1969
7. F. M. Klaassen, "On the Substrate Current Noise in MOS Transistors Beyond Pinchoff." Proc. IEEE (Lett), V 59, #2, pp. 331-332, February, 1961.
8. C. T. Sah, H. C. Pao, "The Effects of Fixed Bulk Charge on the Characteristics of MOS Transistor." IEEE, ED-13, #4, p. 393, April, 1966.
9. W. Shockley, "Problems Related to p-n Junctions in Silicon." Solid State Electronics, V 2, #1, pp. 35-67, January, 1961.
10. G. A. Baraff, "Distribution Functions and Ionization Rates for Hot Electrons in Semiconductors." Phy. Rev., V 128, #6, pp. 2507-2517, December, 1962
11. A. S. Tager, "Current Fluctuations in a Semiconductor under the Conditions of Impact Ionization and Avalanche Breakdown." Fiz. Tver. Tela., V6, pp. 2418-2427, or Soviet Phys. Solid State, VG #8, pp. 1919-1925, February, 1965

12. R. J. McIntyre, "Multiplication Noise in Uniform Avalanche Diodes." IEEE Trans., ED-13, #1, pp. 164-168, January, 1966
13. C. T. Sah, "Theory of MOS Capacitor." Solid State Electronics Laboratory, University of Illinois Technical Report 1, December, 1964.
14. T. M. Chen, A van der Ziel, "Hanbury Brown--Twiss Type Circuit for Measuring Small Noise Signals." Proc. IEEE, V 53, #4, p. 395, April, 1965.
15. H. L. Kalter, "A System for High-Accuracy Noise Measurement." Engineer Degree Thesis, University of Florida, 1970.
16. A. G. Chynoweth, "Ionization Rates for Electrons and Holes in Silicon." Phys. Rev., V 109, #5, p. 1537, March, 1958.
17. T. Ogawa, "Avalanche Breakdown and Multiplication in Silicon p-n Junctions." Jap. J. Appl. Phys., V 4, pp. 473-484, July, 1965.
18. C. T. Sah, S. Y. Wu, F. H. Hielscher, "The Effect of Fixed Bulk Charge on the Thermal Noise in MOS Transistors." IEEE Trans., ED-13, #4, p. 410, April, 1966.
19. F. M. Klaassen, J. Prins, "Thermal Noise of MOS Transistors." Phillips Res. Repts., V 22, pp. 505-514, 1967.
20. H. E. Halladay, A. van der Ziel, "On the High Frequency Excess Noise and Equivalent Circuit Representation of the MOS-FET with N-type Channel." Solid State Electronics, V 12, # 11, pp. 167-176, November, 1968.
21. A. van der Ziel, "Thermal Noise in the Hot Electron Regime in FET's." IEEE Trans., ED-18, in press.

B. A NEW GRATING TYPE Au-NSi SCHOTTKY-BARRIER PHOTODIODE FOR 0.4-1.06 MICRON PHOTODETECTION (S.S. Li and C.T. Wang)

I. Introduction

The qualities desired in a solid-state photo-detector are high speed, high sensitivity and low noise operation for the photon energies of interest. For years it has been known that a Schottky-barrier (S. B.) photodiode could yield these qualities if incident optical radiation could be efficiently coupled into the depletion layer of the diode to create electron-hole pairs there. Because of losses associated with coupling light through the metal contact into the semiconductor below, however, the potential of an S. B. photodiode has yet to be achieved.

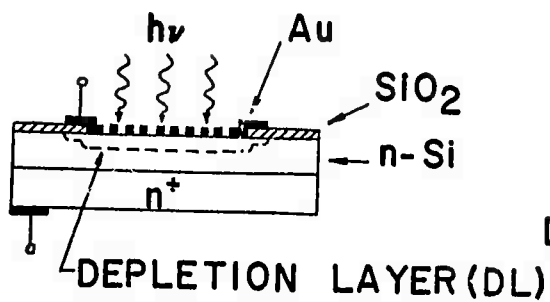
Schneider¹ has attempted a solution to the problem of coupling optical radiation by fabricating contacts of thin ($\sim 100\text{\AA}$), semi-transparent gold film coated with zinc sulfide as an antireflecting agent. Photodiodes made in this way suffer two main disadvantages: (1) they require complicated processing compared with that used in the conventional technology of silicon devices; and (2) the detector shows sensitivity only in a very narrow range of the spectrum.

In this paper we present a grating-type Au-nSi S. B. photodiode fabricated with a new structure of contact mask. The mask forms a grating of gold film over the contacting silicon substrate. The new structure can be readily constructed by employing the standard silicon planar technology. The resulting device shows properties (such as quantum yield and spectral response et al) much superior to those of previous S. B. photodiodes.²

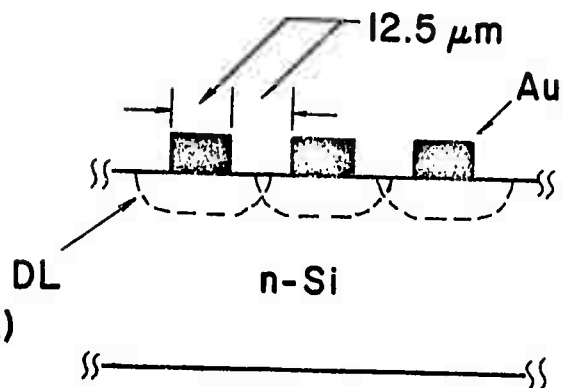
In the following sections, a brief report is given on the I-V characteristics, spectral response, noise performance and the technology used to fabricate such grating type Au-nSi S. B. photodiode.

II. Device Fabrication

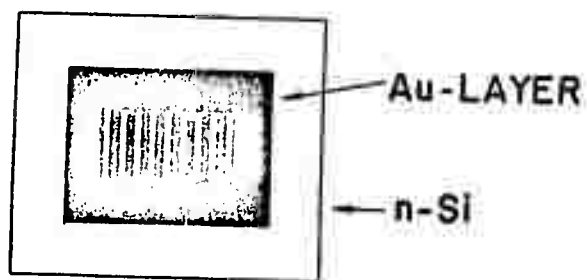
The structure and geometry of the grating type Au-nSi S. B. photodiode is displayed in Fig. 1. The device was constructed by



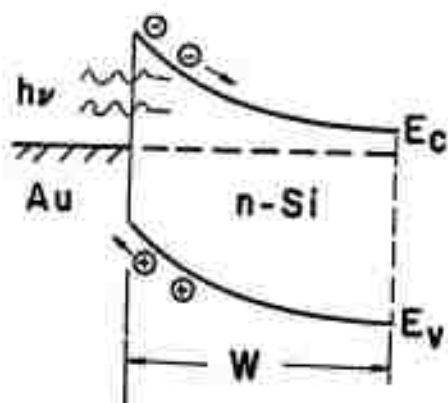
(a) SIDE VIEW



(c) ENLARGED PORTION OF THE WINDOW AREA IN (a).



(b) TOP VIEW



(d) ENERGY BAND OF Au-nSi SCHOTTKY DIODE.

Fig. 1

Structure and geometry of a grating type Au-nSi Schottky-barrier photodiode.

first growing an SiO₂ mask on a 1300 ohm-cm n-type silicon wafer approximately 10 mil thick. A window for metalization was opened on the oxide mask by using standard photoelectric and etching processes. A thin gold film was deposited onto the window area (which is the bare silicon surface) and extended to part of the oxide layer (see Fig. 1(a)) by vacuum evaporation technique. The thickness of the gold film is not crucial in this case and may be of a few microns. The grating pattern of the gold film shown in Fig. 1(b) was made by using the Shipley process. The selection of grating spacing is determined by the resistivity of silicon substrate and the device operating bias condition (since the depletion layer width depends on both the doping density and the applied reverse bias voltage). For example, in the present case, with a 1300-ohm-cm silicon wafer being used, the grating spacing is chosen equal 12.5 μm , which is sufficient to form a complete depletion layer between gold gratings and the silicon surface at zero bias condition (see Fig. 1(c)). The total area of the device is $25 \times 10^{-4} \text{ cm}^2$ and the effective area for photodetection is $9.3 \times 10^{-4} \text{ cm}^2$. However, the area of the device could be either enlarged or reduced, depending on specific applications. Note that extension of the gold film into part of the oxide layer is to serve as a field plate so that soft breakdown could be avoided under large reverse bias condition.³

III. Measurements and Discussions

In this section, we report the results of our measurements on the I-V characteristics of the device under reverse and forward bias conditions, the spectral dependence of the quantum yield, determination of the barrier height and the noise characteristics.

A. I-V Characteristic curves:

The I-V plot for the device G-6 and G-9 under forward bias condition is shown in Fig. 2, for temperatures between 263°K and 317°K. These curves can be described by the Shockley diode equation that

$$I_F = I_S \exp \left(\frac{qV_F}{nkT} \right) \quad (1)$$

where V_F is the applied voltage, n is found (from Fig. 2) to vary between 1.06 and 1.10 for both G-6 and G-9, and I_S is the reverse saturation current which is given by⁴

$$I_S = SA^* T^2 \exp \left(- \frac{q\phi_{Bn}}{kT} \right) \quad (2)$$

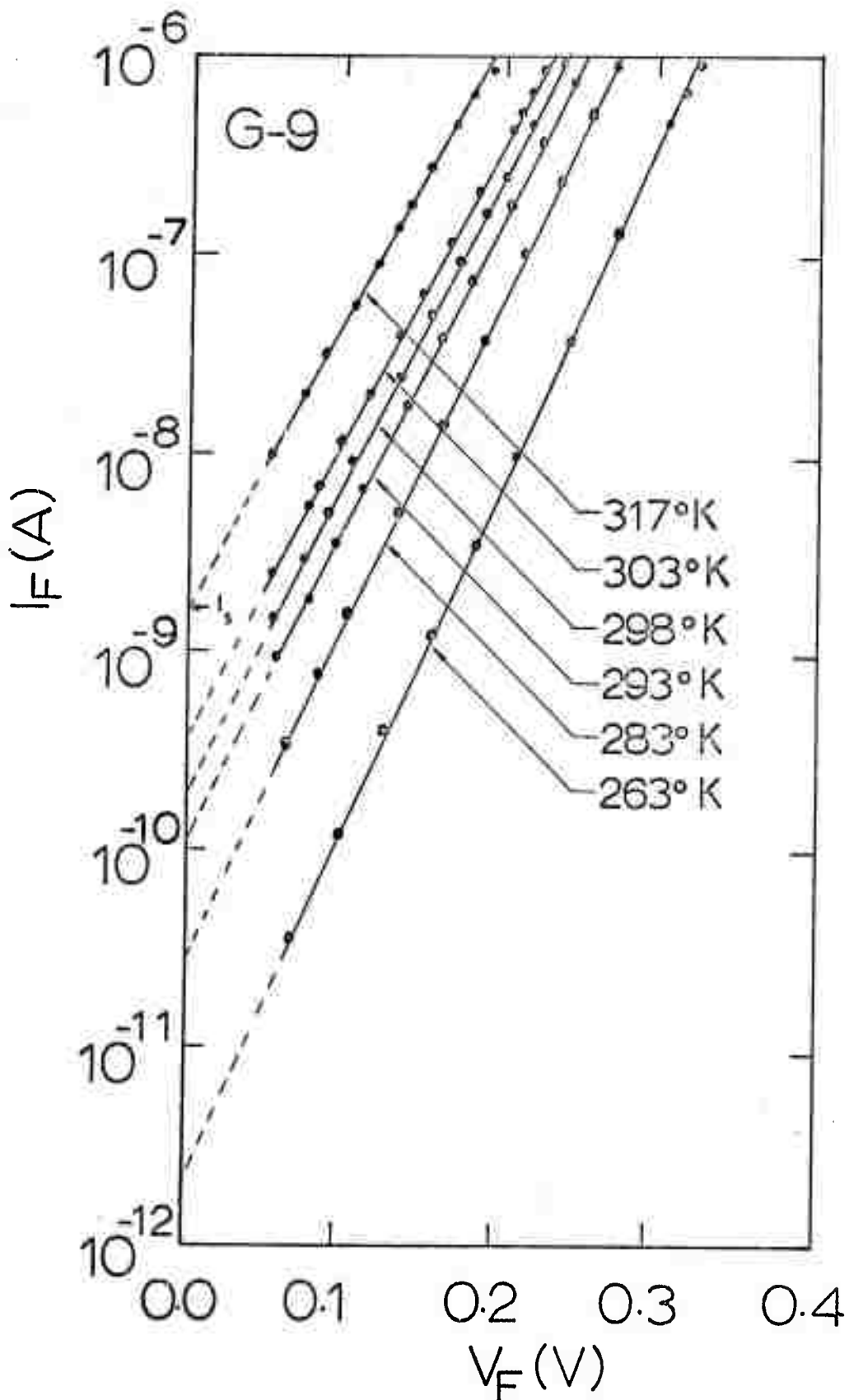


Fig. 2 The I-V characteristic curves for devices G-6 and G-9 under forward bias condition and for different temperatures. I_s is the reverse saturation current. The curves are in accord with the prediction that $I_F = I_s \exp\left(\frac{qV_F}{nkT}\right)$, with n varying from 1.06 to 1.10.

Here A^* is the effective Richardson constant, S is the cross section area of the diode (which is equal to $1.57 \times 10^{-3} \text{ cm}^2$ for the present case), and ϕ_{Bn} is the barrier height.

The barrier height, ϕ_{Bn} , is determined from the slope of I_S/T^2 versus $1/T$ plot, as is shown in Fig. 3. The result yields $\phi_{Bn} = 0.8075 \text{ eV}$, which is in good agreement with the reported value for the Au-nSi system.⁴ Note that values of I_S used in Fig. 3 are obtained from Fig. 2. The effective Richardson constant A^* is calculated from Eq. (2) and is found to be 84.2 for $T = 300^\circ\text{K}$ and for $\epsilon_m < 5 \times 10^3 \text{ V/cm}$.

Fig. 4 shows the I-V characteristic curve for Device G-6 under reverse bias condition and for $T = 300^\circ\text{K}$.

To compare the result with theory, we use the following expression for the reverse leakage current, I_R , which is given by:⁵

$$I_R = SA^*T^2 \exp\left(-\frac{q\phi_{Bn}}{kT}\right) \left[1 - \exp\left(-\frac{qV_R}{kT}\right)\right] \quad (3)$$

where V_R is the applied reverse bias voltage, and the barrier height, ϕ_{Bn} , taking into account the image force lowering effect and the static dipolar charge layer effect, can be written as⁵

$$\phi_{Bn} = (\phi_M - \chi) - (q\epsilon_m/4\pi\epsilon_o\epsilon_s)^{1/2} - \alpha\epsilon_m \quad (4)$$

where ϕ_M is the metal work function, χ is the electron affinity of the semiconductor, α is a parameter to be determined from the experiment, and ϵ_m is the maximum electric field strength in the depletion region which is given by⁴

$$\epsilon_m = [(2qN_D/\epsilon_o\epsilon_s)(V_D + V_R)]^{1/2} \quad (5)$$

where V_D is the diffusion potential and N_D is the donor density.

The second term on the right hand side of Eq. (4) represents the image force lowering potential,⁴ and the third term denotes the lowering potential due to the static dipolar charge layer presenting at the metal-semiconductor interface.⁵ The dipole layer is thought to be a fundamental consequence of electronic wave function penetrating from the metal into the forbidden gap of the semiconductor. This correction to the barrier height is assumed to be a linear function of electric field.

The solid line in Fig. 4 is the theoretical curve computed by using Eqs. (3), (4), and (5). The parameters used for this computation are $S = 1.57 \times 10^{-3} \text{ cm}^2$, $A^* = 84.2$, $T = 300^\circ\text{K}$, and $\alpha = 1.74 \times 10^{-5} \text{ cm}$.

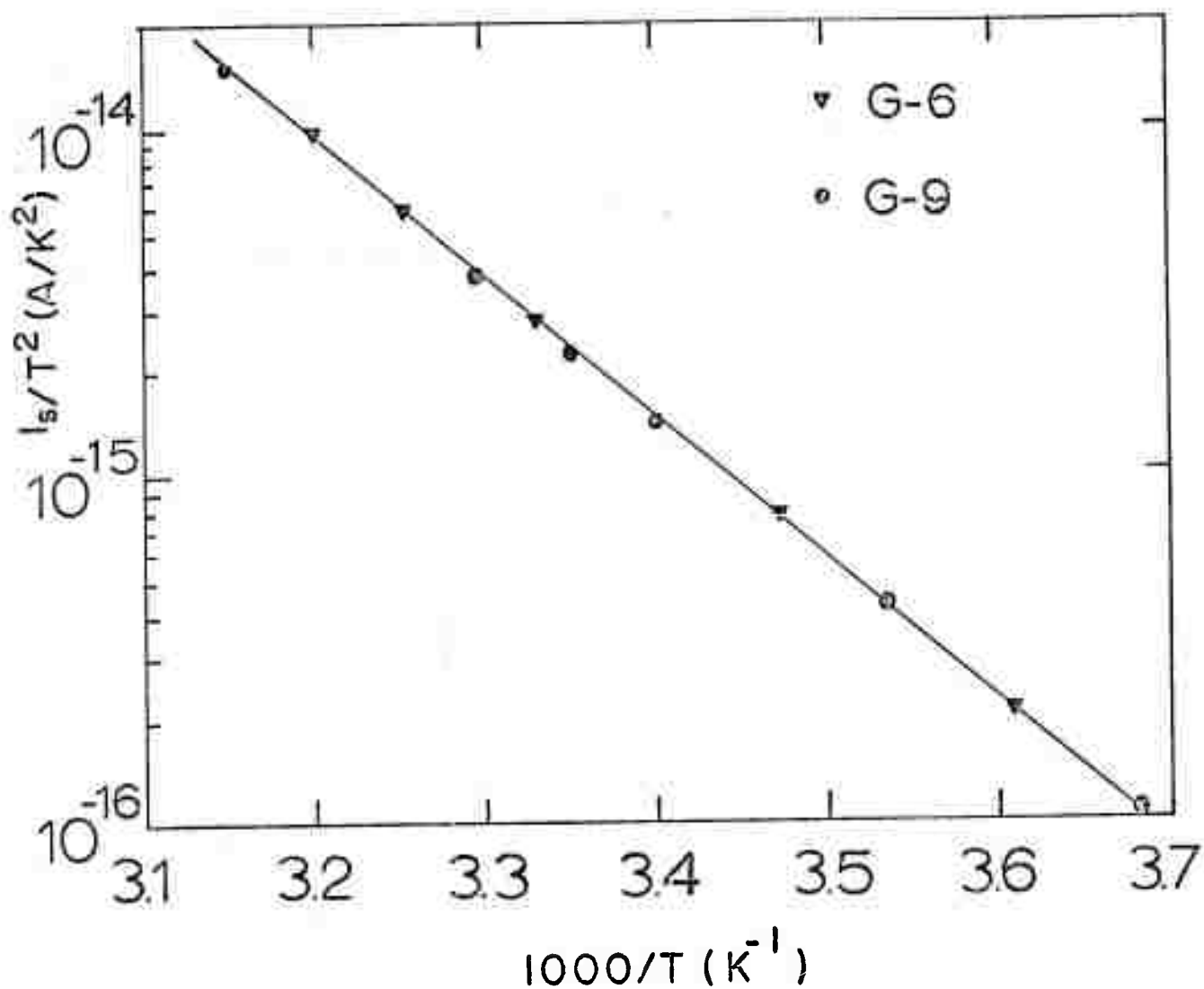


Fig. 3

The reverse saturation current, I_s/T^2 , versus $1/T$ for devices G-6 and G-9. The barrier height, ϕ_{Bn} , deduced from the slope of this plot is 0.8075eV.

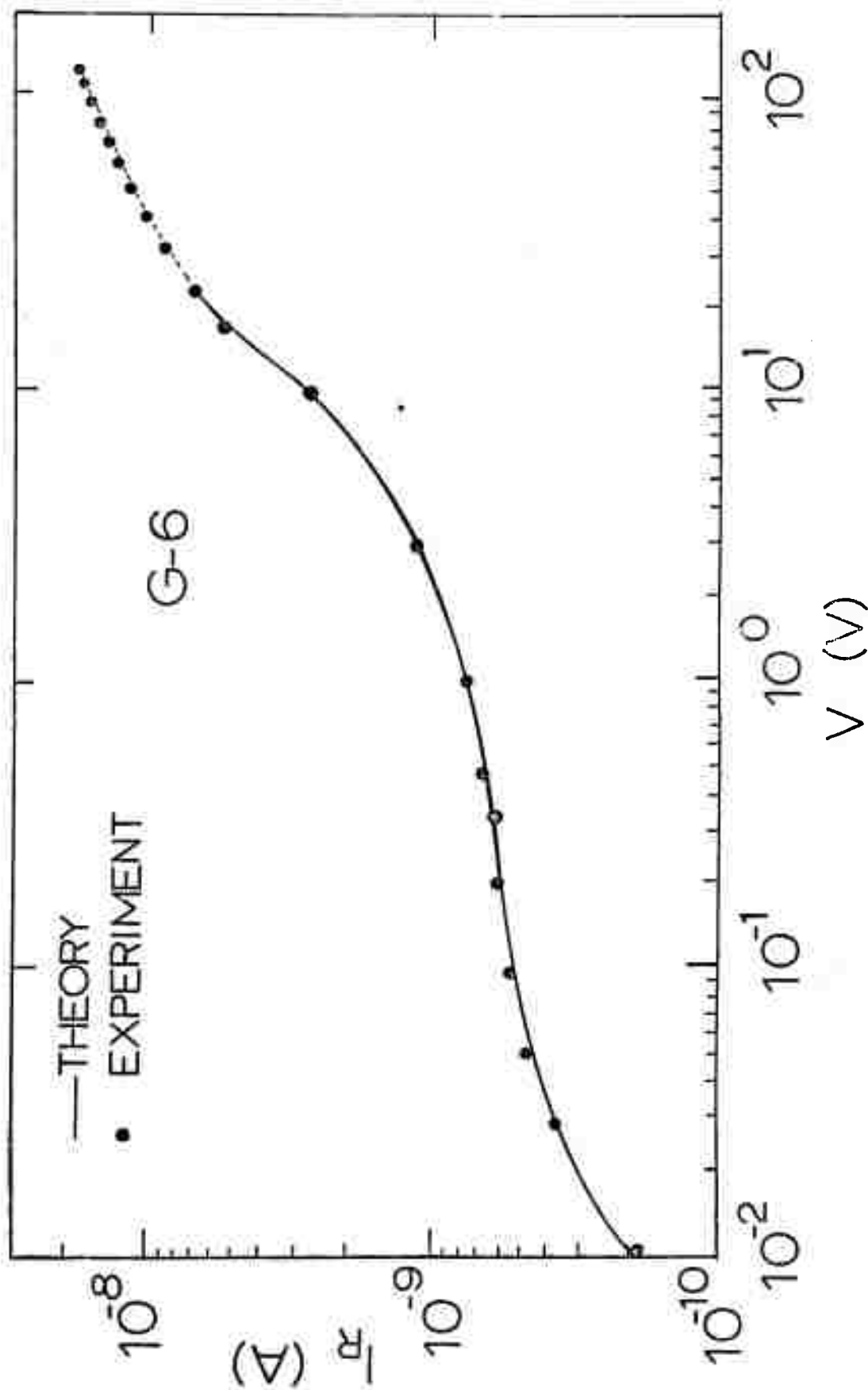


Fig. 4 The I-V characteristic curve for Device G-6 under reverse bias condition and for $T = 300^\circ\text{K}$. The solid line is computed by using Eqs. (2), (3) and (4) of the main text. The parameters used are $\phi_{\text{Bn}} = 0.8075\text{V}$, $A^* = 84.2$ and $\alpha = 1.74 \times 10^{-5}$ cm.

It is noted from Fig. 4 that the results are in excellent agreement with the theory for $V_R < 30V$. For $V_R > 30V$, the theoretical prediction exceeds the measured values. This discrepancy could be corrected if a different value of α is used. The value of α can be determined from the slope of $\ln I_R$ versus $(V_D + V_R)^{1/2}$ plot. The barrier height, ϕ_{Bn} , decreases with increasing reverse bias voltage. For example, $\phi_{Bn} = 0.8075V$ at $V_R = 0$ and $\phi_{Bn} = 0.7069V$ at $V_R = 30V$.

B. Spectral Response and Quantum Yield

Fig. 5 shows the spectral response curves for devices G-6 and G-9 for $V_R = 0$ and $10V$, and for $T = 300^\circ K$. The results show that at zero bias voltage, the net quantum yield (i.e. photo-current per absorbed photon) exceeds 0.6 for wavelength between $0.5 \mu m$ and $0.85 \mu m$ and is about 0.06 at $\lambda = 1.06 \mu m$; at $V_R = 10V$, the quantum yield varies between 0.8 - 0.85 for λ between $0.55 \mu m$ and $0.9 \mu m$, and is about 0.15 at $\lambda = 1.06 \mu m$. This result can be explained as follows. The present device is operating in depletion-mode photo-detection. The main contribution of the photocurrent in such device comes from photocarriers generated in the depletion region and the carriers generated within one diffusion length outside the depletion layer region. At zero bias condition, it is believed the depletion layer of the present device may not well cover the whole silicon window areas between the gold gratings, and hence the quantum yield may not be very high due to the recombination losses outside the depletion region. However, by increasing the reverse bias voltage, the depletion layer width is increased, as a result more photocarriers are generated within the depletion region, and hence the quantum yield is increased.

The responsivity (i.e. photocurrent/incident photon energy density/sec) of devices G-6 and G-9 is also calculated. The results yield that $R = 0.44 A/W$ at $\lambda = 0.63 \mu m$ and $V_R = 10V$, and $R = 0.63 A/W$ at $\lambda = 0.9 \mu m$. The spectral dependence of the responsivity for device G-6 is also displayed in Fig. 5, for $V_R = 10V$.

C. Response Time

Since the present device is operating under depletion mode photodetection, the upper limit of device response time will be equal to the carrier transit time across the depletion layer (which is of the order of 10^{-11} sec.). However, since the RC time constant of the device is longer than the carrier transit time, the response time of the present device will be limited by the RC time constant. The

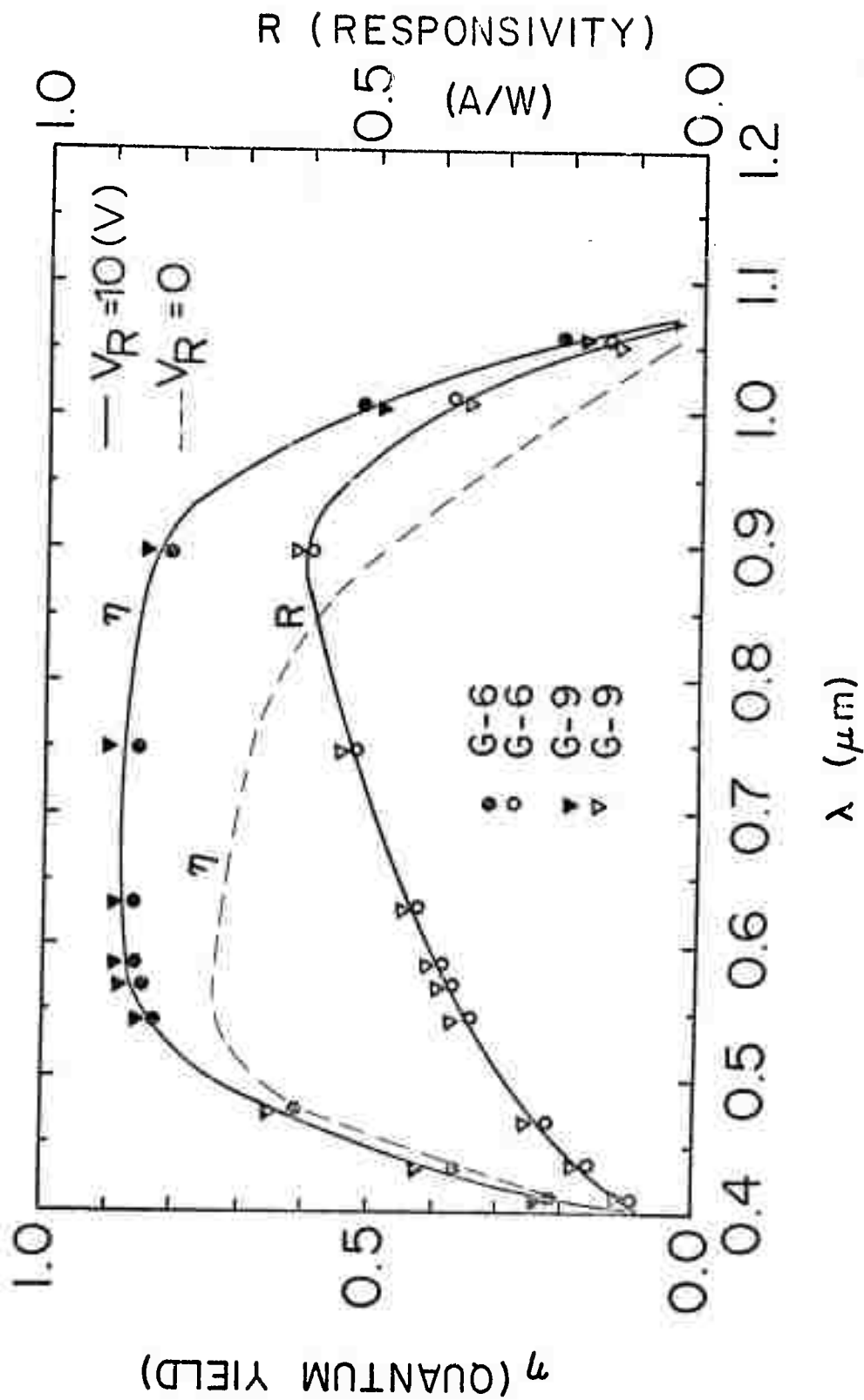


Fig. 5

The spectral dependence of quantum yield and responsivity for devices G-6 and G-9, for $V_R = 10\text{V}$.

series resistance of the device is equal to $1.5 \text{ K}\Omega$ and the capacitance at $V_R = 10\text{V}$ is found to be 3pf . Therefore, the RC time constant of the present device at $V_R = 10 \text{ V}$ is 4.5 nsec , which should be the upper limit of the device response time. We have made use of device G-6 to detect the light pulse of a Strobotac light source and observed the rise time of light pulse to be $0.15 \text{ }\mu\text{sec}$ and pulse width of $0.4 \text{ }\mu\text{sec}$., in good agreement with the value specified by the instructions manual. This indicates that our detector has a response time less than $0.15 \text{ }\mu\text{sec}$.

D. Noise Measurements and Noise Equivalent Power (NEP)

The noise measurements on our detector are performed by employing a low noise, high input impedance ($10\text{M}\Omega$) preamplifier incorporated with a noise resistance of $1.24 \text{ K}\Omega$. A general radio (G.R.) 1381 Random-Noise generator, a G.R. 1925 multifilter and a G.R. 1926 multichannel RMS detector have been used for noise analysis.

The resulting noise spectrum is plotted in Fig. 6, for device G-9, with the reverse bias voltage $V_R = 8.6\text{V}$ and the primary current, $I_p = 132 \text{ nA}$.

The primary current, I_p , is the sum of the dark leakage current, I_R , and the photocurrent, I_{ph} . The broken line in Fig. 6 represents the full shot noise, I_N , calculated from $I_N = \sqrt{2qI_p\Delta f}$.⁶ The measured equivalent noise current is somewhat lower than the computed full shot noise. This is expected at this low level of primary current due to the fact that effect of traps in the interface region and the recombination centers in the junction region may not be completely negligible. If this is the case, the measured equivalent noise current is usually less than the calculated full shot noise.⁶

The equivalent excess $1/f$ noise current for G-9 (and G-6) is about 553 nA at 10Hz and decreases to 15nA at 100 Hz . It has been pointed out by Hsu⁷ that the $1/f$ noise for an S.B. diode using field plate structure³ will not be a strong function of the reverse bias voltage; this has also been observed for the present case.

The noise equivalent power (NEP) is defined as the noise equivalent current per responsivity of the detector. In the present device, we have calculated the NEP for device G-6 for $\lambda = 0.63 \text{ }\mu\text{m}$ and $0.90 \text{ }\mu\text{m}$. Table 1 summarizes all the important measured and calculated parameters for G-6 and G-9 grating type Au-nSi Schottky-Barrier photodiodes.

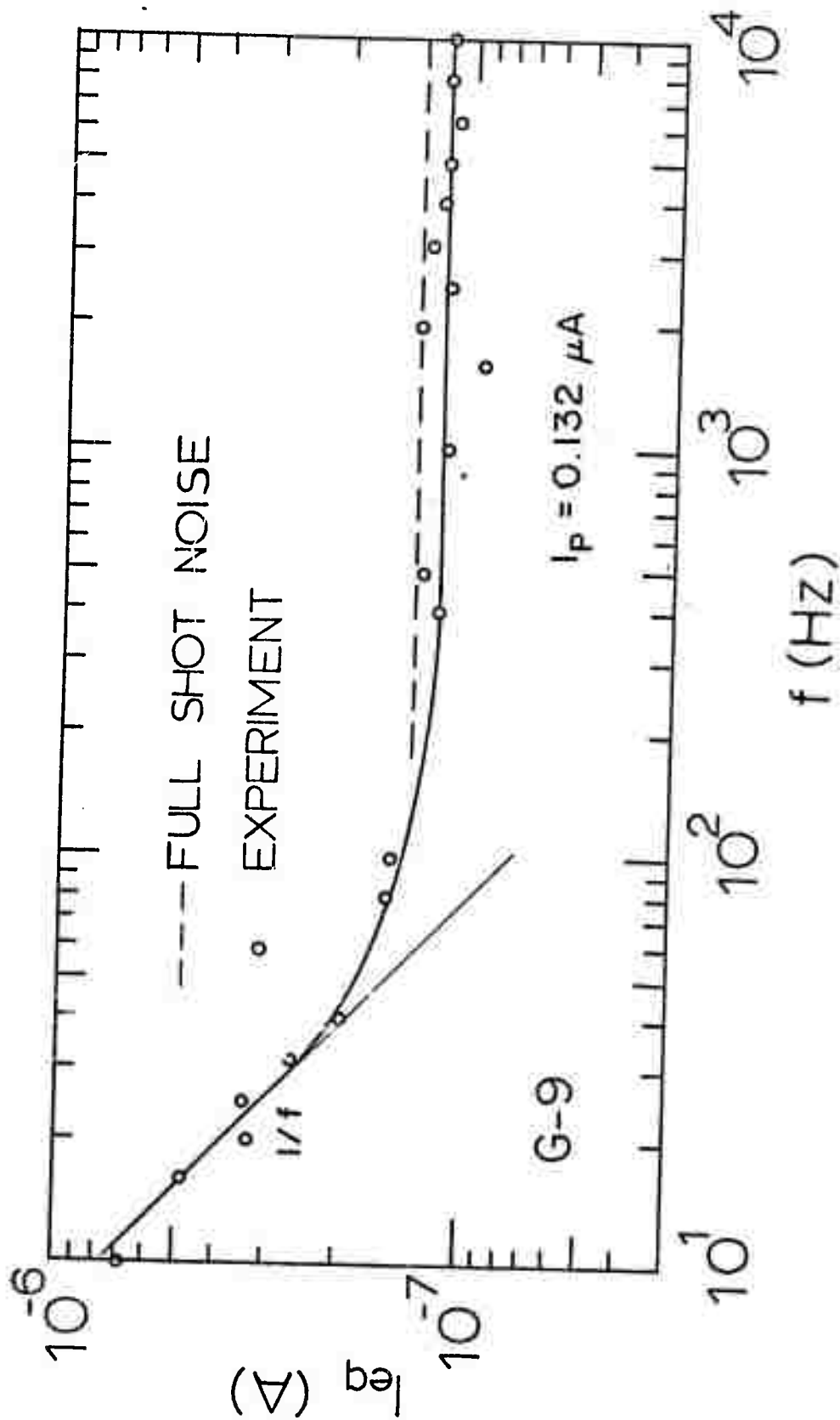


Fig. 6 The noise equivalent current is plotted as a function of frequency for Device G-9, for $V_R = 8.6V$ and $I_p = 132nA$, where V_R is the reverse bias voltage, I_p is the primary current. The broken line is the full shot noise calculated from

$$I_N = \sqrt{2qI_p \Delta f}$$

TABLE I

Measured and Computer Parameters for a Grating-type

Au-nSi Schottky Barrier Photodiode,

$$V_R = 10V \text{ and } T = 300^\circ K$$

1. Device active area: $9.3 \times 10^{-4} \text{ cm}^2$
2. Silicon substrate resistivity: $1300 \Omega\text{-cm}$
3. Spacing between gold gratings: $12.5 \mu\text{m}$
4. Series resistance: $1.5 \text{ K}\Omega$ at $V_F = 1V$
5. Capacitance: $C = 45 \text{ pf}$ at $V_R = 0$, $C = 3 \text{ pf}$ at $V_R = 15V$
6. Full shot noise current: $I_N = 2 \times 10^{-14} \text{ A}$ at $V_R = 1V$
 $I_N = 4 \times 10^{-14} \text{ A}$ at $V_R = 10V$
7. Photoresponse: (at $V_R = 10V$ and $\lambda = 0.9 \mu\text{m}$)
 Quantum yield: 0.85
 Responsitivity: $R = 0.63 \text{ A/W}$
 NEP: $6.3 \times 10^{-14} \text{ W}$
 Detectivity (D^*): $0.48 \times 10^{12} \text{ cm} - \text{Hz}^{1/2}/\text{W}$

REFERENCES

1. M. V. Schneider, Bell Sys. Tech. J., 45, 1611 (1966).
2. H. Melchion, M. B. Fisher and F. R. Arams, Proc. IEEE, 58, 1466 (1970).
3. A. Y. C. Yu and C. A. Mead, Solid State Elec., 13, 97 (1970).
4. S. M. Sze, Phys. of Semi-Devices, p. 399, Wiley (1969).
5. J. M. Andrews and M. P. Lepselter, Solid State Elec., 13, 1011 (1970).
6. R. J. Minniti, Jr., G. W. Neudeck and R. M. Anderson, J. Appl. Phys., 42, 1886 (1971).
7. S. T. Hsu, I.E.E.E. Trans. on Electr. Devices, ED-17, 495 (1970).

C. QUANTUM YIELD OF METAL-SEMICONDUCTOR PHOTODIODES
(S. S. Li, F. A. Lindholm and C. T. Wang)

I. Introduction

Gärtner⁽¹⁾ has expressed the quantum yield, or internal quantum efficiency, (defined as the photon current produced per absorbed photon) in a metal-n-type semiconductor photodiode as

$$\eta = 1 - \frac{e^{-\alpha W}}{(1 + \alpha L_p)} \quad (1)$$

In this expression α is the absorption coefficient of the semiconductor, the magnitude of which depends strongly on the photon wavelength, W is the depletion layer width, and L_p is the diffusion length of minority carriers.

Eq. (1) predicts that the quantum yield will approach unity if $\alpha W \gg 1$. For most metal-semiconductor photodiodes this inequality is indeed obeyed in the short wavelength region (near UV region) of the spectrum where the absorption coefficient exceeds 10^4 cm^{-1} .⁽²⁾ In conflict with the prediction of Eq. (1), however, experimental observations⁽³⁾ show a sharp decrease in quantum yield with decreasing wavelength. Although qualitative explanations⁽¹⁾ have been suggested to account for this decrease, no quantitative analysis has yet been given.

In this paper we show that the observed fall-off can be attributed to the presence of an inversion layer near the metal-semiconductor interface. A principal result of the paper is a theoretical expression including the effects of an inversion layer and displaying the functional dependence of quantum yield upon doping concentration and photon wavelength. This expression, together with related expressions for the width of the inversion region and for the electric field in the inversion region, are derived in the Appendices. In the presentation immediately below, we apply these expressions to a Au-nSi Schottky barrier diode. The theoretical predictions agree well with observed behavior, including the decrease in quantum yield seen at short wavelengths.

For concreteness, we shall assume in our discussion below that the semiconductor is n-type. A similar treatment will describe the behavior of p-type Schottky photodiodes.

II. Existence of an Inversion Layer in a Metal-n-type Semiconductor Diode

According to Shockley and Spenke,⁽⁴⁾ an inversion layer forms in a metal-n-type semiconductor diode if either: (1) the barrier height of the diode exceeds one half of the forbidden band gap of the constituent semiconductor, or (2) a large concentration of acceptor surface states is present at the interface between metal and semiconductor. Condition (1) is fulfilled for Schottky-barrier photodiodes such as Au-nSi, PtSi-nSi, and any metal-n GaAs.⁽⁵⁾ In the absence of donor surface states, therefore, one can expect a p-type inversion region to exist in these diodes.

Fig. 1(a) shows the energy band diagram for a metal-n semiconductor diode when an inversion layer is present at the interface between metal and semiconductor. Fig. 1(b) shows a schematic representation of the carrier profile (not to scale) in the inversion region and in the bulk. Henish⁶ finds it instructive to regard the inversion layer as a thin highly conductive film, termed a channel or gutter, bordering the surface. There is much experimental evidence for its existence in germanium and silicon.⁽⁷⁻⁹⁾

III. Computation of the Inversion and Depletion Layer Widths for a Au-nSi Schottky Diode

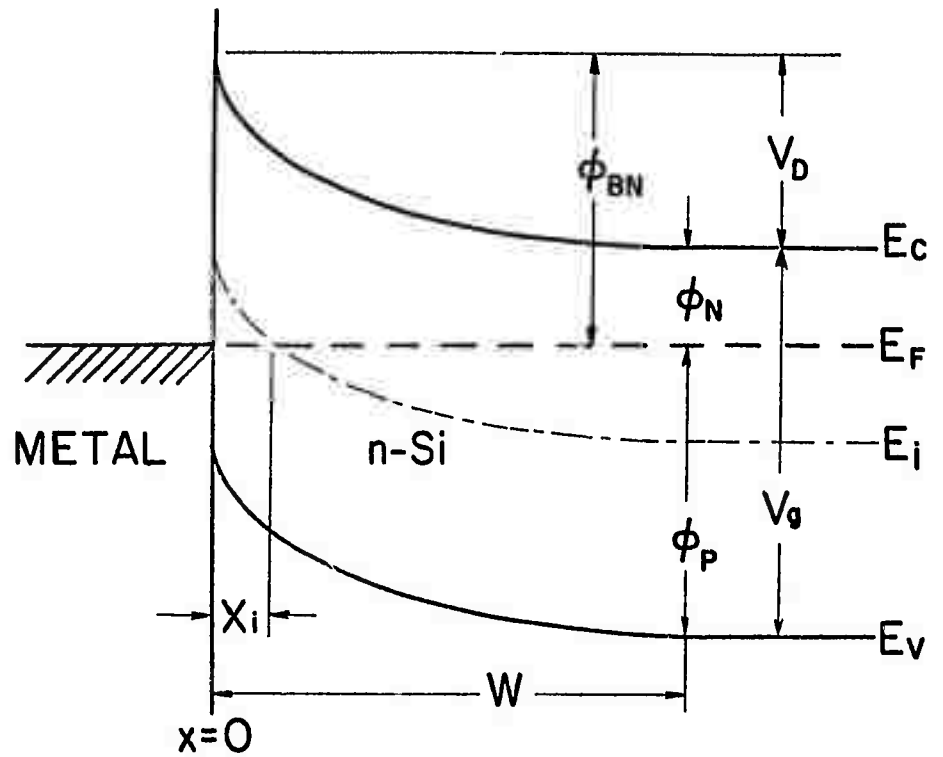
As is derived in Appendix A, the inversion layer width x_i at zero bias voltage is given by:

$$x_i = \left(\frac{\epsilon_0 \epsilon_R}{2qN_D V_D} \right)^{1/2} \left[\left(\phi_{Bn} - \frac{1}{2} V_g \right) - V_t \ln \left(\frac{\sqrt{V_D + V_t \left(\frac{N_V}{N_D} \right) \exp \left(-\frac{V_g - \phi_{Bn}}{V_t} \right) + \sqrt{V_D}}}{\sqrt{V_D + V_t \left(\frac{N_V}{N_D} \right) \exp \left(-\frac{V_g}{2V_t} \right) + \sqrt{V_D}}} \right) \right] \quad (2)$$

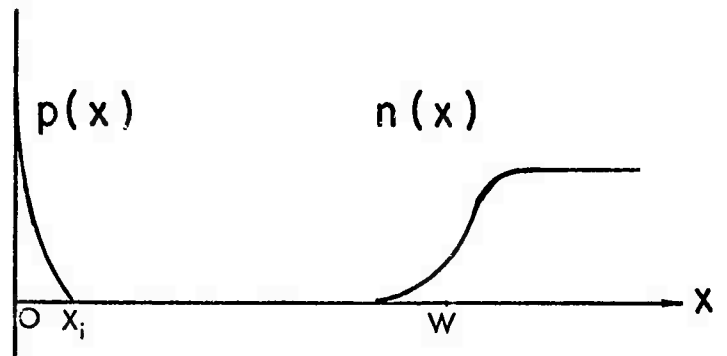
where ϵ_0 is the free space permittivity, ϵ_R is the dielectric constant of the semiconductor (e.g. $\epsilon_R = 11.7$ for Si), N_D is the donor density, V_D is the diffusion potential, ϕ_{Bn} is the barrier height of the diode, V_g is the energy gap of the semiconductor expressed in electron volts, V_t is the thermal voltage kT/q , and N_V is the effective density of states in the valence band.

For a Au-nSi Schottky photodiode, the logarithmic term in the bracket of Eq. (2) is much smaller than the term $\left(\phi_{Bn} - \frac{1}{2} V_g \right)$. Thus

$$x_i = \left[\frac{\epsilon_0 \epsilon_R}{2qN_D V_D} \right]^{1/2} \left(\phi_{Bn} - \frac{1}{2} V_g \right) \quad (3)$$



(a) BAND DIAGRAM



(b) CARRIER PROFILE

Fig. 1 (a) Energy band diagram for a metal-n-type semiconductor photo-diode when an inversion layer is present.
(b) Spatial dependence of electrons and holes in the bulk of semiconductor and in the inversion layer region, respectively.

Using Eq. (3), we compute the inversion layer width for a Au-nSi Schottky-barrier photodiode as a function of donor density. The result is shown in Fig. 2.

The total depletion layer width, W , is not materially affected by the presence of an inversion layer,⁽¹⁰⁾ and thus the conventional depletion approximation gives

$$W \approx \left[\frac{2\epsilon_o \epsilon_R (V_D + V_R)}{qN_D} \right]^{1/2} \quad (4)$$

The functional dependence of W for a Au-nSi Schottky barrier photodiode, computed by using Eq. (4), is also shown in Fig. 2; V_R denotes the reverse bias voltage.

The electric field strength within the inversion layer is given by

$$\epsilon(x) = \left(\frac{2qN_D}{\epsilon_o \epsilon_R} \right)^{1/2} \left[-(\phi_n + V(x)) + V_t \left(\frac{N_V}{N_D} \right) \exp\left(-\frac{V(x) + V_R}{V_t}\right) \right]^{1/2} \quad (5)$$

The derivation appears in Appendix A. Eq. (5) predicts that the electric field holds nearly constant in the inversion layer, as shown in Table AI. This constancy justifies an approximation used in Appendix B to derive the expression for quantum yield.

IV. Calculation of the Quantum Yield for a Au-nSi Schottky-Barrier Photodiode

The presence of an inversion layer at the interface between metal and semiconductor has an important effect on the quantum yield of a metal-semiconductor photodiode, particularly in the short wavelength region of the spectrum. Derivation of the quantum yield for a metal-n-type semiconductor photodiode in which an inversion layer is present is given in Appendix B, and the result is

$$\eta = \left(\frac{\alpha L_n}{\alpha L_n + \epsilon/\epsilon_c} \right) \left[e^{-\alpha x_i} - \frac{1}{\alpha x_i} (1 - e^{-\alpha x_i}) \right] + \left(e^{-\alpha x_i} - \frac{e^{-\alpha W}}{(1 + \alpha L_p)} \right) \quad (6)$$

where $\epsilon_c = kT/qL_n$ is called the critical field, $\bar{\epsilon}$ is the mean electric field strength in the inversion region deduced from Eq. (5), L_n is the electron diffusion length in the inversion region, and L_p is the hole diffusion length in the n-region. The first term on the right hand side of Eq. (6) is due to the contribution from the inversion region, while the second term represents contributions from both depletion layer region and the bulk of the semiconductor. Note that Eq. (6) reduces to that of Gärtner's expression (Eq. (1)) if $x_i = 0$.

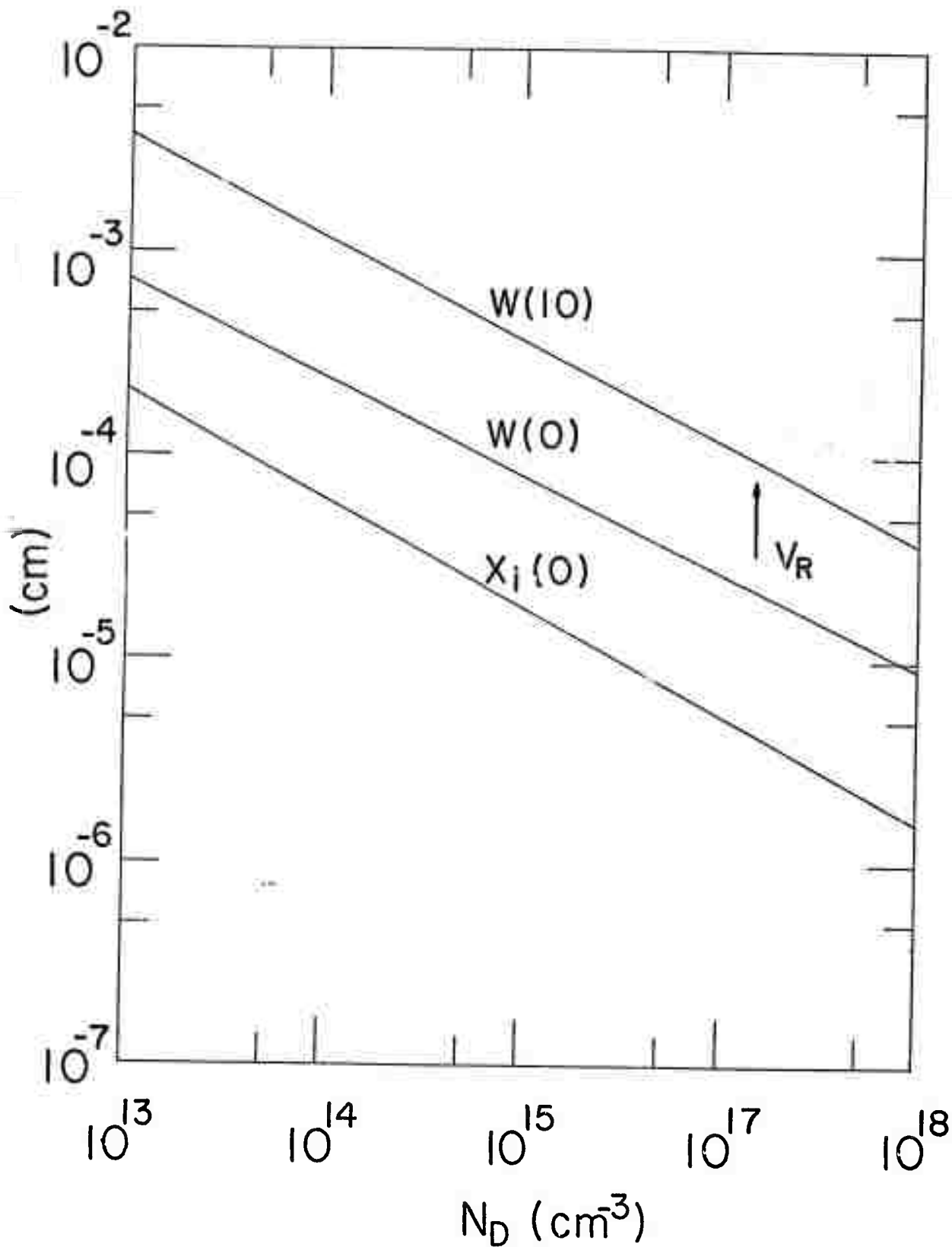


Fig. 2 Dependence of the inversion layer width x_i and the depletion layer width W on the doping densities, N_D , for a Au-nSi Schottky-barrier photodiode, for $V_R = 0$ and 10V.

We now apply Eq. (6) to calculate the quantum yield for a Au-nSi Schottky-barrier photodiode. For a Au-nSi Schottky-barrier photodiode, the barrier height ϕ_{Bn} is 0.81 eV⁽⁵⁾ and the band gap $V_g = 1.12$ eV at 300°K, is expected to be $\phi_{Bn} > V_g/2$. Thus, because $\phi_{Bn} > V_g/2$, one may expect an inversion layer to exist in the absence of large concentrations of donor surface states. In computing the quantum yield, η , we use the data for the absorption coefficient of silicon given by Dash and Newman⁽¹¹⁾ and the carrier diffusion length deduced from the lifetime data given by Ross and Madigan.⁽¹²⁾ The results are shown in Figures 3-5.

Fig. 3 shows the quantum yield versus photon wavelength for a Au-nSi photodiode, with doping concentrations, N_D , as a parameter and for $V_R = 0$. The result indicates that the quantum yield depends strongly on the doping densities both in the short wavelength and the long wavelength sides of the spectrum. In the long wavelength side, the quantum yield increases with decreasing doping densities, while in the short wavelength region the quantum yield increases with increasing doping densities.

This behavior can be explained by using the results shown in Fig. 2 together with Eq. (6) for the quantum yield. From Eq. (6) note that the depletion layer width, W , determines the quantum yield in the long wavelength region; the quantum yield will increase with increasing W . From Eq. (4), it is also noted that the depletion layer width is inversely proportional to the square root of the doping density. As a result, the quantum yield is expected to increase with decreasing doping density in the long wavelength region. On the other hand, the inversion layer width, x_i , controls the quantum yield in the short wavelength side of the spectrum; the quantum yield increases with decreasing values of x_i . Furthermore, Eq. (3) shows that x_i is inversely proportional to the square root of the doping concentration N_D . Therefore the quantum yield will increase with increasing doping density in the short wavelength region of the spectrum, and decrease with increasing doping densities in the long wavelength region.

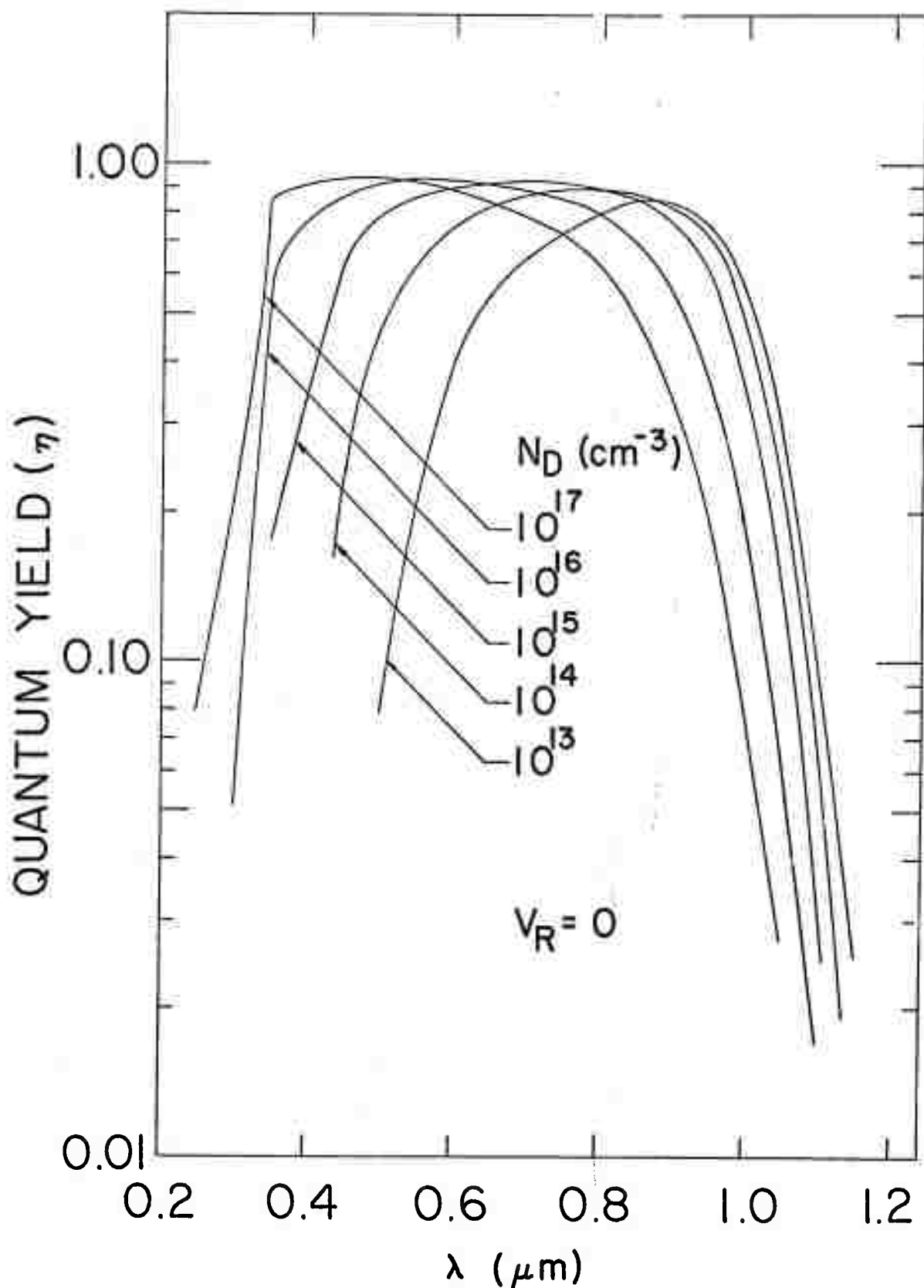


Fig. 3 The quantum yield, η , versus photon wavelength, λ , for a Au-nSi photodiode with doping density as a parameter, and for $V_R = 0\text{V}$. The result shows that η increases with increasing doping density in the short wavelength region, and decreases with increasing doping density in the long wavelength region.

To compare the theoretical curve with experimental data, we fabricated a Au-nSi Schottky-barrier photodiode having a gold film approximately 100Å thick and a doping density of the n-Si substrate of $4 \times 10^{14} \text{ cm}^{-3}$. The measured and theoretical values for the quantum yield are displayed in Fig. 4. Note that the experimental data in the short wavelength regime are in excellent agreement with the theoretical values, while in the long wavelength region the measured values are lower than the calculated values. The discrepancy can be attributed to the fact that the reflection coefficient for gold film increases in the long wavelength side of the spectrum.¹ To lend credibility to this explanation, we measured the quantum yield of a grating-type Au-nSi Schottky barrier photodiode¹⁴ and compared with the theoretical curve computed from Eq. (6). The result displayed in Fig. 5, shows that the theoretical predictions and the experimental data are in excellent agreement over the whole spectral range.

It is concluded that the sharp decrease of the quantum yield in the short wavelength region for a metal-n-type silicon photodiode can be attributed to the presence of an inversion layer. By increasing the doping density of the semiconductor one can reduce this effect.

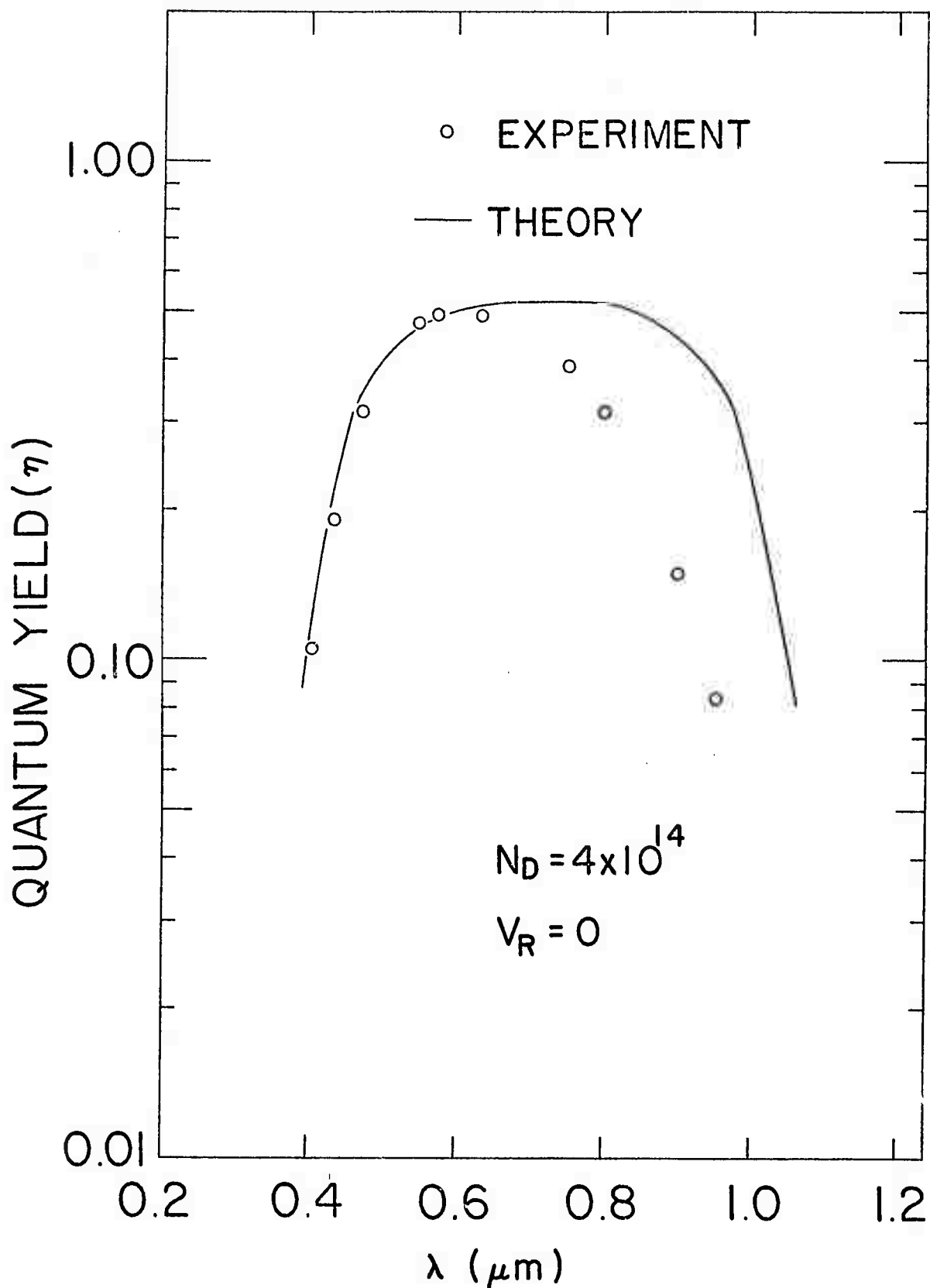


Fig. 4 Comparison of the computed quantum yield with experimental data for a thin film type Au-nSi photodiode for $V_R = 0$ and $N_D = 4 \times 10^{14} \text{ cm}^{-3}$. The theoretical curve has been normalized at $\lambda = 0.6 \mu$.

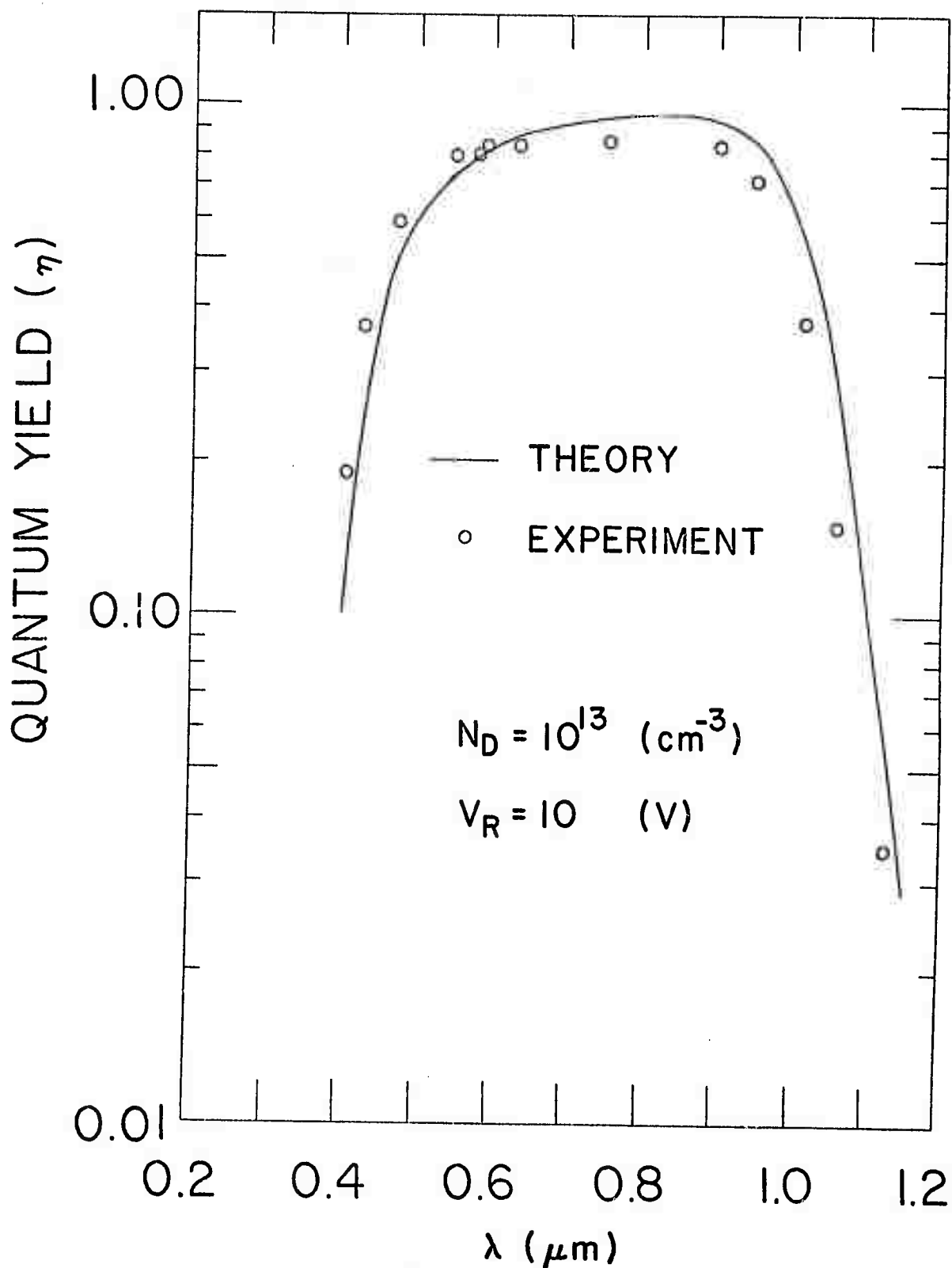


Fig. 5 Comparison of the computed quantum yield with experimental data for a grating type Au-nSi Schottky-barrier photodiode, for $V_R = 10\text{V}$ and $N_D = 10^{13} \text{ cm}^{-3}$. The grating structure is designed to overcome the reflection loss due to gold film.¹⁴

Appendix A: Derivation of the inversion layer width for a metal-n-type semiconductor diode

If we neglect the majority carriers (electrons) in the inversion layer of the diode shown in Fig. 1(b), the space charge carrier density is

$$\begin{aligned} \rho(x) &= q(N_D + p(x)), \text{ for } 0 < x < x_i \\ &\approx qN_D, \quad x_i < x < W \end{aligned} \quad (\text{A.1})$$

where

$$p(x) = N_V \exp\left(-\frac{\phi_p(x)}{V_t}\right) = N_V \exp\left(-\frac{V_g + V(x)}{V_t}\right) \quad (\text{A.2})$$

In writing Eq. (A.2), we have assumed that in the inversion region the quasi Fermi level for holes is nearly constant. This assumption is valid for light intensities small enough that $\overline{\Delta p} \ll \overline{p}_0$ where $\overline{\Delta p}$ and \overline{p}_0 denote the excess density and the equilibrium density, both averaged over the width of the inversion layer. Substituting Eqs. (A.1) and (A.2) into Poisson's equation gives

$$\frac{d^2 V(x)}{dx^2} = - \left(\frac{q}{\epsilon_o \epsilon_R} \right) \left[N_D + N_V \exp\left(-\frac{V_g + V(x)}{V_t}\right) \right] \quad (\text{A.3})$$

The electric field strength, $\epsilon(x)$, within the inversion layer region is obtained by integrating (A.3) once and then using the boundary condition that $\frac{dV(x)}{dx} = 0$ at $x = W$. This yields:

$$\epsilon(x) = \left(\frac{2qN_D}{\epsilon_o \epsilon_R} \right)^{1/2} \left[-(\phi_n + V(x)) + V_t \left(\frac{N_V}{N_D} \right) \exp\left(-\frac{V_g + V(x)}{V_t}\right) \right]^{1/2}, \quad 0 < x < W \quad (\text{A.4})$$

Eq. (A.4) is used to estimate the electric field strength within the inversion region of a Au-nSi Schottky-barrier diode. The result for different doping densities is computed in Table A.1, for $x = 0$ and $x = x_i$. For $0 < x < x_i$, note that the electric field strength within the inversion region varies by at most 25% for all doping densities.

The inversion layer width is obtained by integrating Eq. (A.4) once and using the boundary conditions that $V(x) = -\phi_{Bn}$ at $x = 0$, and $V(x) = -V_g/2$ for $x = x_i$. The result is

$$x_i = \left(\frac{\epsilon_o \epsilon_R}{2qN_D V_D} \right)^{1/2} \left[\left(\phi_{Bn} - \frac{1}{2} V_g \right) - V_t \ln \left(\frac{\sqrt{V_D + V_t \left(\frac{N_V}{N_D} \right) \exp\left(-\frac{V_g - \phi_{Bn}}{V_t}\right)} + \sqrt{V_D}}{\sqrt{V_D + V_t \left(\frac{N_V}{N_D} \right) \exp\left(-\frac{V_g}{2V_t}\right)} + \sqrt{V_D}} \right) \right] \quad (\text{A.5})$$

Eq. (A.5) is derived for the case of zero bias voltage, and can be further simplified for Au-nSi Schottky-barrier photodiodes. The detailed discussion is given in the main text.

The result given in Eq. (A.5) is obtained using the treatment employed first by Bamburg⁽¹³⁾ and Henisch.⁽¹⁶⁾

| $N_D (\text{cm}^{-3})$ | 10^{13} | 10^{14} | 10^{15} | 10^{16} | 10^{17} |
|---|--------------------|--------------------|--------------------|--------------------|--------------------|
| $\epsilon_m (\text{volt/cm})$ at $x=0$ | 1.20×10^3 | 3.89×10^3 | 1.29×10^4 | 4.29×10^4 | 1.42×10^5 |
| $\epsilon_i (\text{at } x=x_i)$ | 7.81×10^2 | 2.79×10^3 | 9.82×10^3 | 3.37×10^4 | 1.15×10^5 |

Table A.1 Electric field strength in the inversion region of Au-nSi Schottky barrier photodiodes, with donor density as a parameter. Computed from Eq. (A.4).

Appendix B: Derivation of the quantum yield for a metal-n-type semiconductor photodiode when an inversion layer is present

The current density J_{ph} produced by the incident (non-reflected) photon flux ϕ is the superposition of hole and electron components,

$$J_{ph} = J_n + J_p, \quad (B.1)$$

which applies at any plane x in the diode. Thus

$$\begin{aligned} J_{ph} &= J_n(x_i) + J_p(x_i) \\ &= J_n(x_i) + J_p(W) + J_{dep} \end{aligned} \quad (B.2)$$

where

$$J_{dep} = J_p(x_i) - J_p(W) \quad (B.3)$$

is the component of hole current density arising from carrier generation in the depletion region. To find the functional dependence of the quantum yield η , therefore, we need only express $J_n(x_i)$, $J_p(W)$, and J_{dep} as functions of ϕ .

The derivation is based on the following assumptions: (1) small injection (Δn or $\Delta p \ll n_o, p_o$), (2) small reverse bias condition (no avalanche multiplication occurs within the depletion region).

For monochromatic radiation, the rate of generation of photocarriers is

$$g(x) = \phi \alpha e^{-\alpha x} \quad (B.4)$$

Thus

$$\begin{aligned} J_{dep} &= -q \int_{x_i}^W g(x) dx = -q \int_{x_i}^W \phi \alpha e^{-\alpha x} dx \\ &= q \phi (e^{-\alpha x_i} - e^{-\alpha W}) \end{aligned} \quad (B.5)$$

where x_i is the inversion layer width given by Eq. (A.5)

In the bulk of the n-type semiconductor, holes, the minority carriers, flow mainly by diffusion. Thus the continuity equation becomes

$$D_p \frac{\partial^2 \Delta p}{\partial x^2} - \frac{\Delta p}{\tau_p} + g(x) = 0, \quad x > W \quad (B.6)$$

where D_p , τ_p denote the hole diffusion constant and lifetime, respectively. From the solution⁽¹⁾ of this equation, one finds that

$$J_p(W) = (q\phi) \frac{\alpha L_p}{(1 + \alpha L_p)} e^{-\alpha W} \quad (B.7)$$

Since the inversion region is very close to the metal surface, Eq. (B.4) implies that the excess carriers generated in this region arise mainly from the absorption of short wavelength photons. The pertinent continuity equation is

$$D_n \frac{\partial^2 \Delta n}{\partial x^2} - |\bar{\epsilon}| \mu_n \frac{\partial \Delta n}{\partial x} - \frac{\Delta n}{\tau_n} + g(x) = 0, \quad 0 < x < x_i \quad (B.8)$$

Here we have approximated the electric field in the inversion layer by the mean electric field $\bar{\epsilon}$, derived from Eq. (A.4).

Substituting Eq. (B.4) into (B.8), yields

$$\frac{\partial^2 \Delta n}{\partial x^2} - \frac{|\bar{\epsilon}|}{\epsilon_c} \frac{1}{L_n} \frac{\partial \Delta n}{\partial x} = - \left(\frac{\phi \alpha}{D_n} \right) e^{-\alpha x} \quad (B.9)$$

where $\epsilon_c = \frac{kT}{qL_n}$, for $L_n = 0.05$ cm, $\epsilon_c = 0.5$ eV at $T = 300^\circ\text{K}$.

For the case of Au-nSi Schottky diode, $|\bar{\epsilon}/\epsilon_c| \gg 1$ (see Table A.1).

The general solution of Eq. (B.9) can be written as:

$$\Delta n = A \cosh \left(\frac{x_i - x}{L} \right) + B \sinh \left(\frac{x_i - x}{L} \right) - \left(\frac{\phi L_n}{D_n} \right) \frac{e^{-\alpha x}}{(\alpha L_n + |\bar{\epsilon}/\epsilon_c|)} \quad (B.10)$$

where $L = \frac{|\bar{\epsilon}|}{\epsilon_c} L_n$ is the effective electron diffusion length in the inversion region.

Constants A and B in Eq. (B.10) are determined from the boundary conditions that $\Delta n = 0$ at $x = x_i$ and $x = 0$. The results yield:

$$A = \left(\frac{\phi L_n}{D_n} \right) \frac{e^{-\alpha x_i}}{\alpha L_n + |\bar{\epsilon}/\epsilon_c|} \quad (B.11)$$

and,

$$B = \left(\frac{\phi L_n}{D_n} \right) \left(\frac{1}{\alpha L_n + |\bar{\epsilon}/\epsilon_c|} \right) \left(\frac{1 - e^{-\alpha x_i} \cosh(x_i/L)}{\sinh(x_i/L)} \right) \quad (B.12)$$

The electron diffusion current density directed towards the depletion region may be evaluated at $x = x_i$, the result is given by:

$$J_n(x_i) = qD_n \frac{d\Delta n(x_i)}{dx} = \left(\frac{q\phi\alpha L_n}{\alpha L_n + |\bar{\epsilon}/\epsilon_c|} \right) \left[e^{-\alpha x_i} - \left(\frac{1}{\alpha L_n} \right) \frac{1 - e^{-\alpha x_i} \cosh(x_i/L)}{\sinh(x_i/L)} \right] \quad (B.13)$$

For a Au-nSi Schottky barrier photodiode, $x_i \ll L$, Eq. (B.13) reduces to:

$$J_n(x_i) = \left(\frac{q\phi\alpha L_n}{\alpha L_n + |\bar{\epsilon}/\epsilon_c|} \right) \left[e^{-\alpha x_i} - \left(\frac{1}{\alpha x_i} \right) (1 - e^{-\alpha x_i}) \right] \quad (B.14)$$

Combining Eqs. (B.1) through (B.14), the total photocurrent density produced in the diode is thus given by:

$$J_{ph} = \left(\frac{q \Phi \alpha L_n}{\alpha L_n + |\bar{E}/\epsilon_c|} \right) \left[e^{-\alpha x_i} - \left(\frac{1}{\alpha x_i} \right) (1 - e^{-\alpha x_i}) \right] + \left[e^{-\alpha x_i} - \frac{e^{-\alpha W}}{(1 + \alpha L_p)} \right] q \Phi \quad (B.15)$$

and, the quantum yield is given by:

$$\eta = \frac{J_{ph}}{q \Phi} = \left(\frac{\alpha L_n}{\alpha L_n + |\bar{E}/\epsilon_c|} \right) \left[e^{-\alpha x_i} - \left(\frac{1}{\alpha x_i} \right) (1 - e^{-\alpha x_i}) \right] + \left[e^{-\alpha x_i} - \frac{e^{-\alpha W}}{(1 + \alpha L_p)} \right] \quad (B.16)$$

Eq. (B.16) will reduce to the expression for η given by Gärtner (see Eq. (1)) if $x_i = 0$ (no inversion layer). Eq. (B.16) provides a theoretical description of the fall-off of η seen as the wavelength of the incident photon flux decreases. Qualitatively, this fall-off occurs for the following reason. The carriers generated by photons of short wavelength appear mainly near the surface, in the inversion layer, as is implied by Eq. (B.4). Thus the current resulting from short wavelength excitation must come mainly from carriers generated in the inversion layer. Most of the holes and electrons generated there, however, ultimately flow toward the surface and recombine. The charge of these holes and electrons thus cancel and contribute no net current. The holes are directed toward the surface by the electric field in the depletion and inversion regions. The electrons are directed toward the surface by diffusion, which dominates the drift tendency over most of the inversion layer. Only near the plane $x = x_i$ do drift and diffusion cooperate to direct electrons into the depletion region. Thus only a small fraction of the carriers generated in the inversion layer contribute to the photo-current J_{ph} . We have termed the resulting contribution $J_n(x_i)$ and have displayed its functional dependence in Eq. (B.13).

Eq. (B.16) has been used to calculate the quantum yield for a Au-nSi Schottky-barrier photodiode, for different bias voltages and doping concentrations. Note that the present derivation does not include the reflection loss at the metal surface, and thus the actual quantum yield should be lower than the predicted values by Eq. (B.16), by a fraction of R (where R is the reflection coefficient at the metal surface).

References:

1. W. W. Gärtner, Phys. Rev., 116, 84 (1959).
2. see for example, R. H. Buke, Photoconductivity of Solids, p. 220, Wiley (1960).
3. H. Melchior, M. B. Fisher and F. R. Arams, Proc. IEEE, 58, 1466 (1970).
4. W. Shockley and E. Spenke, Wiss. Veröff, a.d. Siemens-Werken, 18, 225 (1939).
5. S. M. Sze, Phys. of Semiconductors, p. 397, Wiley (1969).
6. H. K. Henisch, Rectifying Semiconductor Contact, p. 224, Oxford (1957).
7. R. Lawrance, A. F. Gibson and J. W. Granville, Ibid, p. 625 (1954).
8. M. Cutler and H. M. Bath, J. Appl. Phys., 25, 1440 (1954).
9. W. L. Brown, Phys. Rev., 91, 58 (1953).
10. J. H. Simpson and H. L. Armstrong, J. Appl. Phys., 24, 25 (1953).
11. W. C. Dash and R. Newman, Phys. Rev., 99, 1151 (1955).
12. B. Ross and J. R. Madigan, Phys. Rev., 108, 1428 (1957).
13. P. C. Bamberg, University of Reading, Thesis (1952).
14. S. S. Li and C. T. Wang, to be presented at the 22nd Electronic Components Conference, May 15-17, Washington, D. C. (1972).

D. DETERMINATION OF ELECTRON AND HOLE CAPTURE RATES IN NICKEL-DOPED GERMANIUM USING PHOTOMAGNETOELECTRIC AND PHOTOCONDUCTIVE METHODS
(H. F. Tseng and S. S. Li)

I. Introduction

It is known that a substitutional nickel atom introduces, in agreement with the tetrahedral covalent bond model, two acceptor levels in the forbidden band of germanium. One of them is located at 0.30eV below the conduction band edge, and the other is 0.22eV above the valence band edge; both levels are known to serve as efficient recombination centers. Nickel atoms can be introduced into germanium crystal by ordinary diffusion process.

The properties of nickel doped germanium have received considerable attention since the recombination property was first investigated by Burton et. al.¹ They were able to interpret the electron-hole recombination in terms of the first acceptor level. Tyler et. al.² later found the second acceptor level, but failed to show that both levels were associated with the same substitutional nickel atom. Subsequently, Battey and Baum,³ in a study of the temperature dependence of lifetime, deduced the electron capture rates in both levels. They found that C_{n1} was independent of the temperature, while C_{n2} increased exponentially with temperature. On the other hand, Okada⁴ showed that photoconductivity in nickel-doped germanium crystals can be interpreted in terms of the temperature independent capture rates C_{n2} and C_{p2} ; Kalashnikov and Tissen⁵ showed that the photomagnetolectric (PME) lifetime in p-type crystals can be interpreted in terms of a two-level model assuming that C_{n1} and C_{n2} are independent of temperature and with ratio of $C_{n1}/C_{n2} = 6$. However, Wertheim,⁶ in his study of the bombardment-conductivity decay-time experiments, concluded that C_{n1} and C_{n2} are independent of temperature but with the ratio $C_{n1}/C_{n2} = 1/6$, which is contradictory to the result of Kalashnikov and Tissen.⁵ This discrepancy was later explained by Eliseev and Kalashnikov⁷ as due to dislocations in their early germanium crystals, and concluded that C_{n2} is larger than C_{n1} with the ratio $C_{n1}/C_{n2} = 1/6$.

Note that the ratios of electron capture rates, C_{n1}/C_{n2} reported by Wertheim⁶ and Eliseev et.al.⁷ are consistent at room temperature (i.e., $C_{n1}/C_{n2} = \frac{1}{6}$). However, the values of C_{n1} and C_{n2} reported by Eliseev et.al. are a factor of 2 smaller than that of Wertheim (see Table I). The values of hole capture rates reported by previous authors

Table 1
Capture Rates for Nickel Atoms in Germanium (in units of 10^{-9} cm³/sec), T=300°K

| Authors | C _{n1} | C _{n2} | C _{p1} | C _{p2} |
|--------------------------------------|-----------------|-----------------|-----------------|-----------------|
| Burton et al ¹ | 0.8 | - | - | >40 |
| Wertheim ⁶ | 0.96 | 5.9 | - | ~100 |
| Eliseev and Kalashnikov ⁷ | 0.5 | 3 | - | - |
| This paper | 1.4 | 8 | - | 40 |

are even more widely spread and less conclusive. The main reason for this is due to the fact that most of these results are determined from the temperature dependence of lifetimes, which is further complicated and prone to lead incorrect results if some of the recombination parameters (e.g., capture rates) become temperature dependent.

In this paper, we shall demonstrate that by including the excess carrier trapping effect in the theory of photomagnetolectric (PME) and photoconductive (PC) effects and by elaborately controlling the compensation ratio of nickel and shallow impurity densities in germanium, we are able to determine carrier capture rates more accurately at room temperature from PME and PC measurements. Furthermore, by closely examining the previous results, we are able to interpret consistently the present results with those reported by Wertheim and Eliseev et.al.

II. Theory

The energy levels of nickel atom in germanium and the transitions among bands and the nickel levels are shown schematically in Fig. 1. The nickel atom in the three possible charge states (with zero, one and two electrons in the two acceptor levels of nickel atom) are designated by N_0 , N_1 , and N_2 , which are further related by the total-ity condition

$$N_0 + N_1 + N_2 = N_i \quad (1)$$

where N_i is the total concentration of nickel atoms. The parameters n_1 , p_1 , n_2 and p_2 represent the carrier densities when the Fermi level coincides with acceptor levels E_1 and E_2 , respectively. They are related to the densities of impurity charge states through the following relations⁸:

$$\begin{aligned} n_1 &= n_0 p_0 / p_1 \\ &= n_0 \cdot \exp (E_1 - E_F) / kT \\ &= n_0 N_0^0 / N_1^0 \end{aligned} \quad (2)$$

similarly, $n_2 = n_0 \exp (E_2 - E_F) / kT$

$$= n_0 N_1^0 / N_2^0 \quad (3)$$

where we have used the superscript "o" to denote the equilibrium densities and E_F is the Fermi level. The above equations also provide the relationship of the equilibrium nickel densities in different charge states to the Fermi level. From Eqs. (1), (2) and (3), the density of nickel atoms in each charge states can be determined from the Hall effect and the conductivity experiments.

From Fig. 1, the rate equations in the bands and the nickel acceptor levels can be written as

$$\begin{aligned}
 \frac{dn}{dt} &= \sum_{j=1}^2 R_{nj} + G \\
 \frac{dp}{dt} &= \sum_{j=1}^2 R_{pj} + G \\
 \frac{dN_2}{dt} &= R_{n2} - R_{p2} \\
 \frac{dN_1}{dt} &= R_{n1} - R_{p1} - \frac{dN_2}{dt} \\
 R_{n1} &= C_{n1} (nN_o - n_1N_1) \\
 R_{p1} &= C_{p1} (pN_1 - p_1N_o) \\
 R_{n2} &= C_{n2} (nN_1 - n_2N_2) \\
 R_{p2} &= C_{p2} (pN_2 - p_2N_1)
 \end{aligned} \tag{4}$$

The charge neutrality condition expressed in terms of the excess densities from the equilibrium values is given by:

$$\Delta p - \Delta n - \Delta N_1 - 2 \Delta N_2 = 0 \tag{5}$$

Under the condition of small injection⁹ (i.e., $\Delta n \ll n_o + n_j$, $\Delta p \ll p_o + p_j$, $j = 1, 2$), and the steady state case, the lifetimes for electrons and holes are defined respectively by⁸:

$$\tau_n = \Delta n / \sum_{j=1}^2 R_{nj} \tag{6}$$

and

$$\tau_p = \Delta p / \sum_{j=1}^2 R_{pj} \tag{7}$$

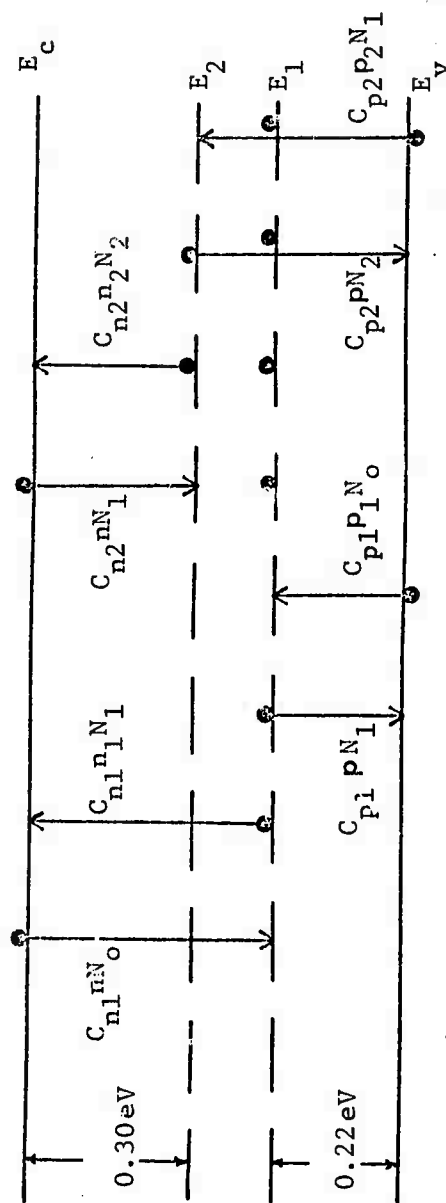


Figure 1

Energy band diagram for nickel-doped germanium; the transitions between the bands and the two nickel acceptor levels are shown.

From Eqs. (4), (5), (6) and (7), the trapping ratio, Γ , and the lifetimes can be expressed by¹⁰

$$\Gamma = \frac{\Delta n}{\Delta p} = \frac{\tau_n}{\tau_p} = \frac{1 - \beta_1 \beta_2 + (1 + \beta_2) \mu_{p1} + (1 + \beta_1) \mu_{p2}}{1 - \beta_1 \beta_2 + (1 + \beta_2) \mu_{n1} + (1 + \beta_1) \mu_{n2}} \quad (8)$$

$$\begin{aligned} \tau_n^{-1} &= (p_o + \Gamma^{-1} n_o) [C_{n1} C_{p1} (N_o^o + N_1^o) / H_1 + C_{n2} C_{p2} (N_1^o + N_2^o) / H_2] \\ &= (p_o + \Gamma^{-1} n_o) \{ [\tau_{po1} (n_o + n_1) + \tau_{no1} (p_o + p_1)]^{-1} \\ &\quad + [\tau_{po2} (n_o + n_2) + \tau_{no2} (p_o + p_2)]^{-1} \} \end{aligned} \quad (9)$$

where

$$H_1 = C_{n1} (n_o + n_1) + C_{p1} (p_o + p_1) \quad (10)$$

$$H_2 = C_{n2} (n_o + n_2) + C_{p2} (p_o + p_2) \quad (11)$$

$$\mu_{n1} = C_{n1} N_o^o / H_1, \quad \mu_{n2} = C_{n2} N_1^o / H_2 \quad (12)$$

$$\mu_{p1} = C_{p1} N_1^o / H_1, \quad \mu_{p2} = C_{p2} N_2^o / H_2 \quad (13)$$

$$\beta_1 = N_o^o / (N_o^o + N_1^o) \quad (14)$$

$$\beta_2 = N_2^o / (N_1^o + N_2^o) \quad (15)$$

$$\tau_{no1} = 1 / C_{n1} (N_o^o + N_1^o), \quad \tau_{no2} = 1 / C_{n2} (N_1^o + N_2^o) \quad (16)$$

$$\tau_{po1} = 1 / C_{p1} (N_o^o + N_1^o), \quad \tau_{po2} = 1 / C_{p2} (N_1^o + N_2^o) \quad (17)$$

For steady state case, $R_{n1} = R_{p1} = R_1$, $R_{n2} = R_{p2} = R_2$, and the relative importance of the net steady state recombination rates of the two levels can be obtained from the following expression⁸:

$$\frac{R_2}{R_1} = C_{n2} (n_o + p_1 C_{p1} / C_{n1}) / C_{p1} (p_o + C_{n2} n_2 / C_{p2}) \quad (18)$$

For n-type sample, $n_o \gg p_o$, $p_1 C_{p1} / C_{n1} \gg C_{n2} n_2 / C_{p2}$, therefore

$R_2 \gg R_1$; the upper level dominates for all temperatures, and the recombination process reduces to the simple Shockley-Read model.¹¹ Eq. (9) then reduces to Eq. (A7) of reference (11).

For p-type samples,

$$R_2/R_1 \approx \frac{C_{n2}}{C_{n1}} \frac{p_1}{p_0} \quad (19)$$

The relative importance of the two acceptor levels depends on the ratio of C_{n2}/C_{n1} and the resistivity of the sample.

For the case of small injection, by taking into account the trapping effect, the steady state PME open circuit voltage can be expressed in terms of the photoconductance^{1,2}:

$$V_{PME} = \frac{(\theta_n + \theta_p)}{\mu_p (b + \Gamma^{-1})} \left(\frac{n_o \Gamma^{-1} + p_o}{n_o b + p_o} \right)^{\frac{1}{2}} \left(\frac{D}{\tau_n} \right)^{\frac{1}{2}} \left(\frac{\Delta G}{G_o} \right) \quad (20)$$

where V_{PME} is the PME open circuit voltage per unit length, $\theta_n = \mu_{nH} B$, $\theta_p = \mu_{pH} B$ are Hall angles for electrons and holes, respectively. ΔG is the photoconductance per unit length to width ratio of the sample, and G_o is the dark conductance. Other parameters not defined here have the conventional meanings. By meanings of Eqs. (8), (9) and (20), we can compute the capture rates and lifetimes from the PME and PC data.

III. Experimental Details

N-type germanium single crystals were cut into rectangular bars with typical dimensions of $0.8 \times 5 \times 12 \text{ mm}^3$. The shallow donor densities were determined from the Hall effect and the conductivity measurements. These samples were cleaned by chemical process and coated with nickel by vacuum evaporation. The samples were then placed in the furnace for diffusion. At the end of the diffusion period, the samples were quenched to room temperature. The nickel concentrations were controlled by the diffusion temperature. The nickel-doped sample was mounted in a AC-310 liquid helium refrigeration system for measurements. The Hall effect and the conductivity measurements were taken by standard d.c. technique. The PME and PC measurements were taken by using a chopped light source and an a-c detecting system, so that the temperature gradient effect can be eliminated.

The samples for investigation were divided into two groups: one group has the nickel densities in the range that $N_i < N_D < 2N_i$. In this way, the nickel doped germanium samples remained as n-type, but with high resistivity. The second group was prepared with $N_i > N_D$, so that samples became p-type after nickel diffusion. The

nickel densities can be determined accurately from Hall effect and the conductivity measurements. We shall next discuss the results of our measurements on these two groups of samples separately.

N-type samples

For this group of samples, the first acceptor level (i.e., E_1 level) of the nickel atom is fully occupied by electrons, and the second acceptor level (i.e., E_2) is partially occupied. The occupation probability of the second level and the densities of nickel in each charge states can be determined from Eq. (3). In order to show that nickel is the only dominant impurity in these samples, we measured the Hall coefficient, electrical resistivity and electron densities as a function of temperature before the PME and PC measurements.

Fig. 2 shows the temperature dependence of Hall mobility for temperature between 180°K and 300°K, for samples Ge - N2 ($N_D = 3.5 \times 10^{15} \text{ cm}^{-3}$, $N_A = 2 \times 10^{15} \text{ cm}^{-3}$). The Hall mobility is found nearly independent of temperature in this temperature range. The electron drift mobility μ_n can be deduced from the relation that¹³

$$\mu_n = \mu_{nH} R_{\infty} / R_H$$

Here μ_{nH} and R_H are the low field Hall mobility and Hall coefficient respectively, and R_{∞} is the Hall coefficient at very high field. For electron, this ratio is nearly equal to unity in the temperature range of interest^(13, 14). Fig. 3 and Fig. 4 illustrate the temperature dependence of resistivity and electron concentration, respectively, for sample Ge - N2. Since the electron mobility is nearly independent of temperature, the activation energies deduced from the slope of these two curves are identical and equal to 0.30 eV. This represents the activation energy of the second acceptor level of nickel. (i.e., $E_2 = 0.30 \text{ eV}$ below the conduction band edge.)

The PME and PC measurements were taken at room temperature, and the result is displayed in Fig. 5, for $B = 3 \text{ kG}$.

The linear relationship between V_{PME} and $\Delta G/G_0$, as predicted by Eq. (20), is observed in Fig. 5.

To calculate the recombination parameters from Eqs. (8), (9) and (2), we examined over ten samples with different donor and nickel concentrations. The parameters n_1 , p_1 , n_2 and p_2 used in computations have the following values at 300°K:

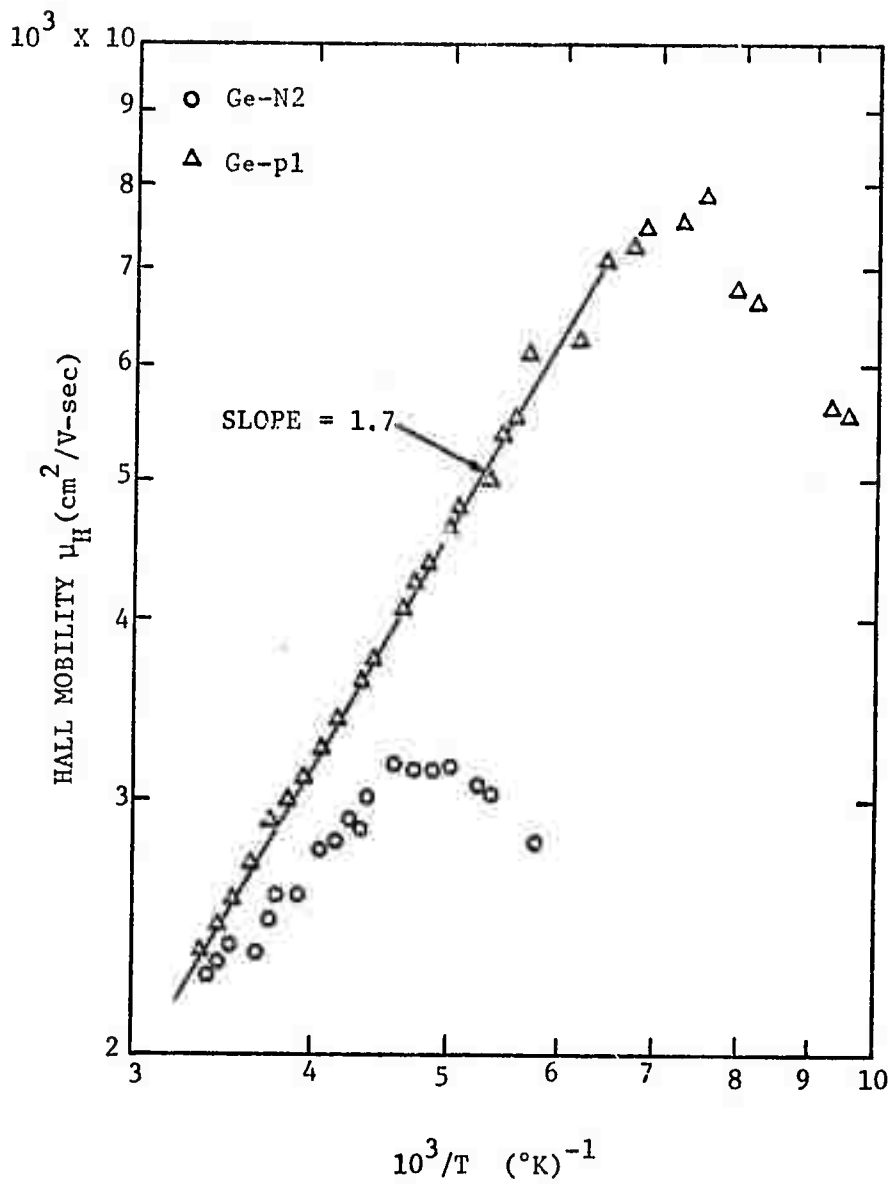


Figure 2

Hall mobility versus temperature for samples Ge-N2 (with $N_D = 3.5 \times 10^{15} \text{ cm}^{-3}$, $N_A = 2.0 \times 10^{15} \text{ cm}^{-3}$) and Ge-P1 (with $N_D = 1.4 \times 10^{14} \text{ cm}^{-3}$, $N_A = 7.5 \times 10^{14} \text{ cm}^{-3}$).

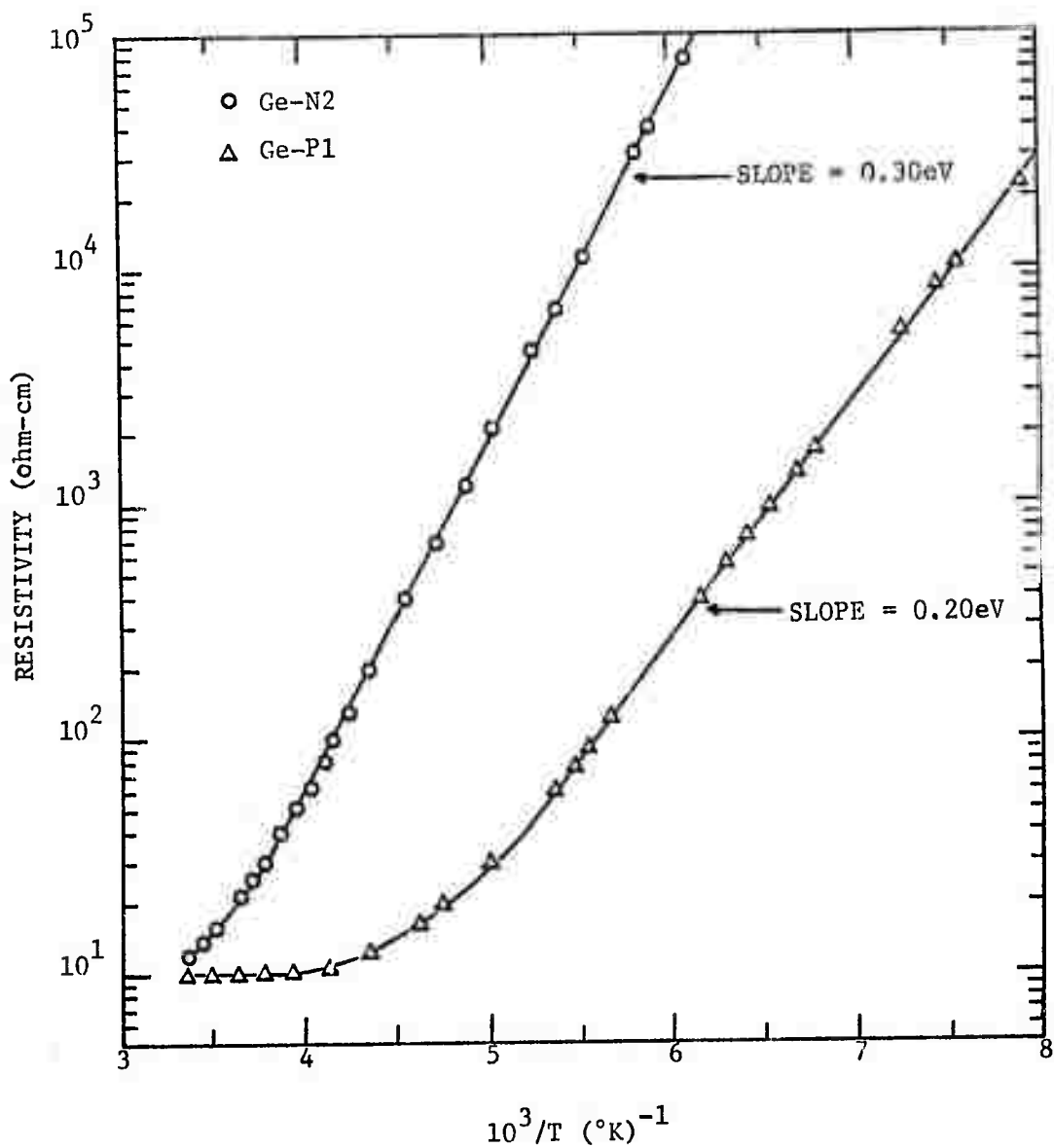


Figure 3

Resistivity versus temperature for samples Ge-N2 and Ge-P1.

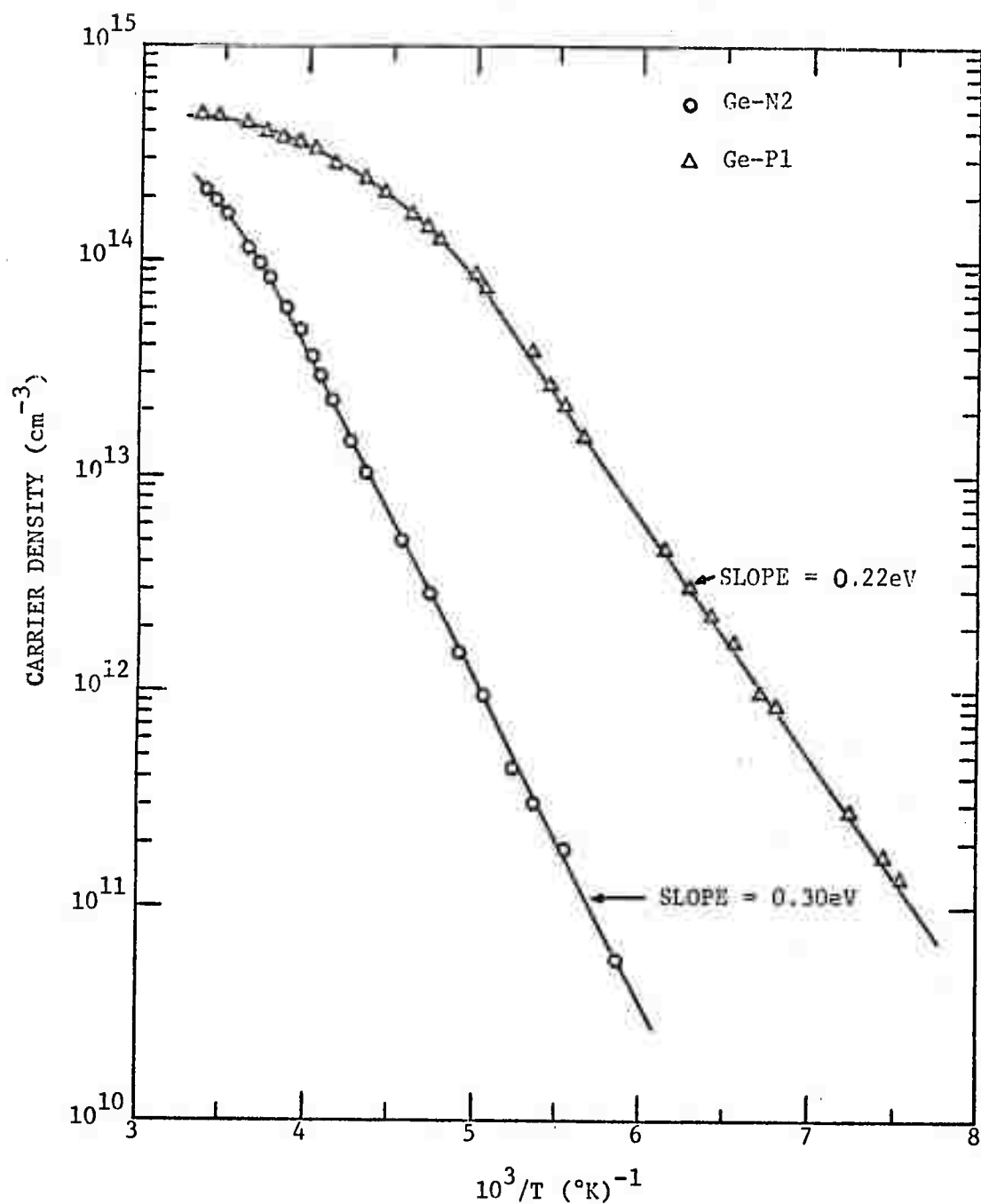


Figure 4

Carrier densities versus temperature for samples Ge-N2 and Ge-P1. The activation energy for Ge-N2 is found equal 0.30 eV which is the second acceptor level of nickel atom in Ge. The activation energy for Ge-P1 is found equal 0.22 eV which is the first acceptor level of nickel atom in Ge.

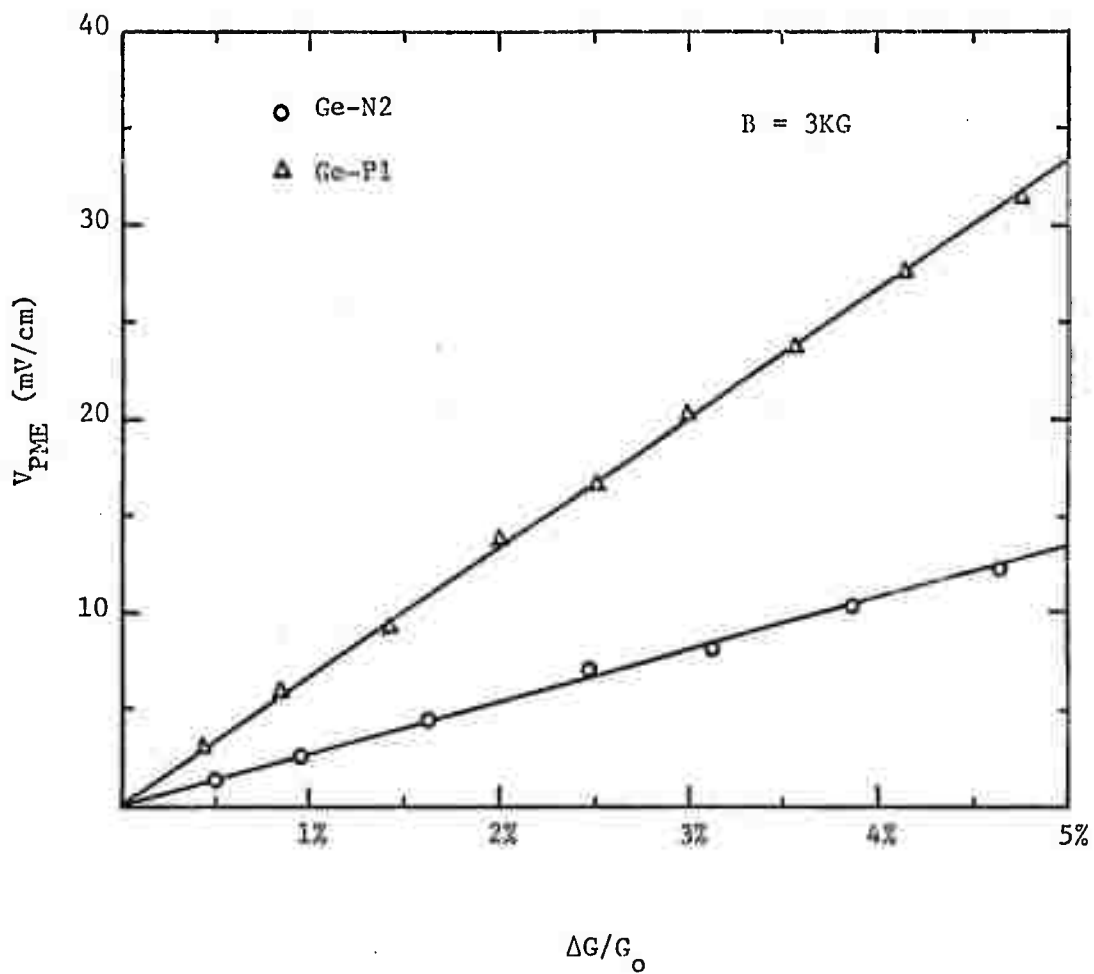


Figure 5

The PME open circuit voltage, V_{PME} , versus photoconductance, $\Delta G/G_0$, for samples Ge-N2 and Ge-P1, for $B = 3$ KG.

$$n_1 = 3.0 \times 10^{11} \text{ cm}^{-3}$$

$$p_1 = 1.2 \times 10^{15} \text{ cm}^{-3}$$

$$n_2 = 9.7 \times 10^{13} \text{ cm}^{-3}$$

$$p_2 = 3.8 \times 10^{12} \text{ cm}^{-3}$$

The electron diffusion coefficient D_n is obtained from μ_n through the use of Einstein's relation that $D_n = \left(\frac{kT}{q}\right) \mu_n$. The ratio of electron and hole mobilities is taken from the results reported by Prince¹⁴.

For n-type samples, the upper level is dominant and the lower level has little effect on the trapping ratio Γ (since p_1 is very large), Eqs. (8) and (9) can be simplified into the forms that:

$$\Gamma = \frac{n_o + n_2 + \gamma_2(p_o + p_2 + N_2)}{n_o + n_2 + \gamma_2(p_o + p_2) + N_1} \quad (21)$$

and

$$\tau_n^{-1} = (p_o + \Gamma^{-1}n_o) / \left[\tau_{po2}(n_o + n_2) + \tau_{no2}(p_o + p_2) \right] \quad (22)$$

where

$$\gamma_2 = C_{p2}/C_{n2}, \text{ and } \tau_{no2} \text{ and } \tau_{po2} \text{ are given by Eqs. (16-17).}$$

From Eqs. (20) and (22), it is noted that V_{PME} and τ_n^{-1} depend greatly on the trapping ratio Γ which in turn depends on the ratio γ_2 .

From the present experimental data, we can calculate γ_2 as well as C_{n2} and C_{p2} . The result yields:

$$\gamma_2 = 5$$

$$C_{n2} = 8 \times 10^{-9} \text{ cm}^3/\text{sec}$$

$$C_{p2} = 40 \times 10^{-9} \text{ cm}^3/\text{sec}$$

For comparison, we summarize our results together with the results reported by other investigators in Table 1.

P-type samples

For this group of samples, the first acceptor level (i.e., E_1) are partially occupied, and the second acceptor level are completely empty. The results are shown in Fig. 2 to Fig. 5 for sample Ge - P1 (with $N_D = 1.4 \times 10^{14} \text{ cm}^{-3}$, $N_A = 7.5 \times 10^{14} \text{ cm}^{-3}$). Fig. 2 shows the hole Hall mobility versus temperature. The temperature dependence of the hole Hall mobility is found to be $T^{-1.7 \pm 0.2}$ which is in good agreement with the $T^{-1.6}$ dependence of hole mobility reported by Prince¹⁴. The temperature dependence of the resistivity shown in Fig. 3 yields a slope of 0.20 eV which is less than the activation energy, $E_1 = 0.22 \text{ eV}$, of the first acceptor level. This is due to the fact that hole mobility increases with decreasing temperature. Fig. 4 shows the hole concentration versus temperature, and the slope of this plot yields the activation energy of the first level, which is found to be 0.22 eV above the valence band edge. The hole drift mobility is deduced from the Hall mobility and the ratio R_H / R_∞ which ranges from 1.4 to 1.8 depending on the temperature and impurity concentration.¹³⁻¹⁴ The linear relationship between V_{PME} and $\Delta G / G_0$ is also observed for p-type samples, as is shown in Fig. 5 and predicted by Eq.(20).

For p-type samples, $p_0 \gg n_0$, also $p_1 \gg n_1$, from Eqs. (9) and (20), it is noted that the trapping ratio Γ has little effect on the values of V_{PME} and τ_n ; also τ_{pol} can be ignored in the expression of τ_n . Thus, for p-type samples, we were unable to determine C_{p1} and γ_1 (where $\gamma_1 = C_{p1} / C_{n1}$) accurately. The relative importance of the recombination in both levels for this case depends not only on the resistivity of the samples, but also on the ratio of C_{n2} / C_{n1} . By varying the resistivity of the samples, which is achieved by changing the nickel doping densities, we can obtain the ratio of C_{n2} / C_{n1} . From this result, we conclude that C_{n2} is larger than C_{n1} with the ratio of $C_{n2} / C_{n1} = 6$.

For samples with $p_0 < p_1$, the second acceptor level (i.e., E_2) dominates the recombination process, and τ_n is nearly equal to τ_{n02} . In this case, the value of C_{n2} obtained from the p-type sample agrees well with that obtained from n-type samples.

For samples with $p_0 < p_1$, the effect of the first acceptor level (i.e., E_1) becomes important. The value of C_{n1} can be determined from the PME and PC measurements. The result yields

$$C_{n1} = 1.4 \times 10^{-9} \text{ cm}^3\text{-sec}^{-1}.$$

For comparison, the above result is also included in Table 1.

IV. Discussions and Comparison with Previous Work

In computing carrier capture rates from lifetime measurements for the nickel-doped germanium crystal, the reasons for the wide spread in the previous results may be attributed to the following facts: (1) experimental difficulties in determining accurately the density of electrically active nickel atoms; (2) failure to include the excess carrier trapping effect in the PME theory; (3) improper assumptions on the temperature dependence of hole capture rates, C_{p2} ; and (4) neglecting term due to hole capture rates, C_{p2} in the lifetime expression for n-type samples, which results in underestimating the electron capture rate, C_{n2} , at room temperature.

In an attempt to avoid all the possible errors cited above, we have employed a unique approach in determining the carrier capture rates for nickel-doped germanium crystals at room temperature. First, we have elaborately controlled the compensation ratio of nickel atoms and the shallow impurity densities (see Section III) such that the density of nickel atoms can be measured accurately. Secondly, instead of computing capture rates from temperature dependence of lifetime data, we have determined the electron and hole capture rates at one single temperature (i.e., room temperature) in both n- and p-type samples; this has the advantage of eliminating possible errors arising from (3) discussed above. Thirdly, we have included the excess carrier trapping effect in our PME and PC theory; our result has shown that the effect of trapping is more prominent in n-type crystals than in the p-type samples. Implications of the above criteria to our present work as well as previous work are discussed as follows.

The ratio of electron capture rates, C_{n1}/C_{n2} , obtained by us is 1/6 at room temperature, which is in excellent agreement with that reported by Wertheim⁶ and Eliseev⁷ et. al., respectively. However, the values of C_{n1} and C_{n2} obtained here are somewhat higher than that of Wertheim and

Eliseev's, while value of C_{p2} obtained here is much lower than that of Wertheim but agree well with Burton et. al.¹ This discrepancy can be explained by the following facts. Wertheim deduced the ratio of C_{n1}/C_{n2} from the two lifetime plateaus, one at low temperature (i.e. C_{n1}) and the other near room temperature (i.e., C_{n2}). Although C_{n1} is independent of temperature due to its neutral-center nature, it has been reported by Belgaev and Miselguk¹⁵ that C_{n2} decreases with decreasing temperature for $140^\circ\text{K} < T < 280^\circ\text{K}$ due to Coulomb repulsion, and is essentially independent of temperature for $280^\circ\text{K} < T < 350^\circ$ due to the tunnelling penetration of the Coulomb barrier by electrons. The room temperature value of C_{p2} reported by Wertheim was taken from his low temperature lifetime data by assuming that C_{p2} is independent of temperature. There has been no temperature dependent data on C_{p2} reported as yet. However, it is expected that value of C_{p2} will decrease with increasing temperature due to its attractive-center nature.¹⁶ Thus the value of C_{p2} reported by Wertheim at room temperature was overestimated, and C_{p2} should be less than $100 \times 10^{-9} \text{ cm}^3\text{-sec}^{-1}$ at $T = 300^\circ\text{K}$. In computing C_{n2} at room temperature from lifetime data for n-type crystals, Wertheim employed Eq. (1) of his paper and neglected term due to C_{p2} . This results in underestimating the value of C_{n2} , because C_{p2} is not negligible at room temperature. In fact, we have substituted values of C_{n2} and C_{p2} , obtained in this paper, into Eq. (1) of his paper, and found that lifetimes computed from this result are in excellent agreement with his measured lifetimes for samples 532 at room temperature. Therefore, the value of C_{n2} reported by Wertheim is somewhat underestimated, while the value of C_{p2} deduced from his low temperature data is overestimated at room temperature. Our present results support such conclusions.

Next, we examine the values of C_{n1} and C_{n2} reported by Eliseev and Kalashnikov.⁷ Their analysis of the lifetime data is essentially similar to that of Wertheim, however, they obtained values of C_{n1} and C_{n2} which are a factor of two lower than that of Wertheim. This is due to the fact that they determined C_{n1} and C_{n2} from the PME method, which they failed to include the trapping effect in their PME theory. They pointed out that the lifetime data observed from photoconductivity-decay experiment was only about 50 ~ 60% of their PME lifetimes. If we use the lifetime data they obtained from photo-decay experiment to analyze Eliseev's data, the results for C_{n1} and C_{n2} will be close to the values of ours. Thus,

the values of C_{n1} and C_{n2} reported by Eliseev et. al. are underestimated, which is due to the fact that they neglected the excess carrier trapping effect in the PME theory.

Finally, the results of capture rates reported by Burton et. al.¹ were obtained from lifetime data, which they determined from diffusion length measured over a wide range of conductivity at room temperature. Although the value of hole capture rate reported by them agrees quite well with ours, it is noted that this data was available before the existence of the upper level had been recognized. The present result confirms that the hole capture rate due to upper level C_{p2} is equal to $40 \times 10^{-9} \text{ cm}^3\text{-sec}^{-1}$ at room temperature.

V. Conclusions

From the present study of the capture rates for nickel-doped germanium crystal determined by PME and PC methods at $T = 300^\circ\text{K}$, we conclude that: (1) The ratio of C_{n1}/C_{n2} is equal to 1/6, which is in good agreement with that of Wertheim and Eliseev et. al.; (2) Our result yields $C_{n1} = 1.4 \times 10^{-9} \text{ cm}^3\text{-sec}^{-1}$, and $C_{n2} = 8 \times 10^{-9} \text{ cm}^3\text{-sec}^{-1}$; this result is consistent with Wertheim's result if C_{p2} was included in his Eq. (1) in computing C_{n2} from room temperature lifetime data, and agrees well with Eliseev et. al.'s result if the trapping effect was included in their PME theory. (3) Our result for C_{p2} ($40 \times 10^{-9} \text{ cm}^3\text{-sec}^{-1}$) is in excellent agreement with Burton et. al.'s value, although their study was completed before the discovery of the upper level; the present result is also consistent with Wertheim's if his low temperature data on C_{p2} was corrected to the room temperature value without approximation. In short, we have demonstrated that by including the trapping effect in the PME and PC theory and by elaborately controlling the compensation ratios of nickel atoms and shallow impurity densities, we are able to determine more accurately than previous results three of the four capture rates for nickel atoms in germanium at room temperature from PME and PC measurements.

References

1. J. A. Burton, G. W. Hull, F. J. Morin and J. C. Severiens, J. Phys. Chem., Vol. 57, p. 853, (1953).
2. W. W. Tyler, R. Newman and H. H. Woodbury, Phys. Rev., Vol. 98, p. 461, (1955).
3. J. F. Battey and R. M. Baum, Phys. Rev., Vol. 100, p. 1634, (1955).
4. J. Okada, J. Phys. Soc. Japan, Vol. 12, p. 471, (1957); Vol. 12, p. 1338, (1957).
5. S. G. Kalashnikov and K. P. Tissen, Soviet Physics - Solid State, Vol. 1, p. 491, (1959).
6. G. K. Wertheim, Phys. Rev., Vol. 115, p. 37, (1959).
7. P. G. Eliseev and S. G. Kalashnikov, Soviet Physics - Solid State, Vol. 5, p. 223, (1963).
8. S. T. Sah and W. Shockley, Phys. Rev., Vol. 109, p. 1103, (1958).
9. S. C. Choo and A. C. Sanderson, Solid-State Electronics, Vol. 13, p. 609, (1970).
10. S. C. Choo, Phys. Rev. B, Vol. 1, p. 687, (1970).
11. W. Shockley and W. T. Read, Jr., Phys. Rev., Vol. 87, p. 835, (1952).
12. S. S. Li and H. F. Tseng, Phys. Rev. B, Vol. 4, p. 490, (1971).
13. J. Wiley, Progress in Semiconductor, Vol. 8, (1964), Chapter 4, pp. 96-131.
14. M. B. Prince, Phys. Rev., Vol. 92, p. 861, (1953).
15. A. D. Belyaev and E. G. Miselyuk, Soviet Physics - Solid State, Vol. 6, p. 2101 (1965).
16. M. Lax, Bull. Am. Phys. Soc. Ser. II, 1, 128 (1956) and J. Phys. Chem. Solids, 8, 66 (1969).

E. AMORPHOUS SEMICONDUCTOR FILMS

(P. K. Chaudhari, E. R. Chenette, and A. van der Ziel)

This report is concerned with the results of an intensive study of the electrical and optical properties of amorphous films of a typical chalcogenide semiconductor. The report is divided into two almost independent parts for convenience.

PART I: OPTICAL PROPERTIES OF As_2Se_3 - Sb_2Se_3 FILMS.

A. INTRODUCTION

The band structure and the transport properties of chalcogenide semiconductor materials have attracted increasing interest in recent years, especially, since new electronic devices^{1,2} have been reported. The use of these materials as photodetectors is of great practical interest. The understanding of the carrier transport behavior in these material is still in its infant state. Many of the properties connected with the electric conductivity seem to vary widely from sample to sample. The reasons are not fully understood. Investigation of optical absorption and photoconductivity has provided valuable insight in the physics of crystalline semiconductors. The main contribution of work reported here is to apply these methods to vitreous semiconductors to obtain information about electronic structure. The emphasis is on the optical properties deduced from optical transmittance data on evaporated films of As_2Se_3 - Sb_2Se_3 at 300°K. These data are analyzed

to determine optical constants (refractive index, extinction coefficient k or absorption coefficient $\alpha = 4\pi k/\lambda$). An analysis of the absorption edge has also been carried out to obtain the optical band-gap, and the nature of the transitions involved (direct or indirect). An interpretation and discussion of the results that are related to the energy band diagram and electron transport behaviour is presented in the discussion of electrical properties (Part II) which follows.

B. EXPERIMENTAL TECHNIQUE

The compounds As_2Se_3 and Sb_2Se_3 used were of high purity (semiconductor grade 99.999+ %). Each compound was weighed separately with precision and then mixed together and ground to a fine powder in a mortar. The resulting material was mixed thoroughly in a steel cylinder with a steel ball by vibrating for three minutes to obtain a homogeneous mixture. Disks of 1 cm diameter and about 1mm thick were formed in a press at 7000 lb/in.^2 at room temperature under vacuum. These alike were then used as sources for evaporation. The evaporation was carried out in a beel jar system at a pressure of about 10^{-6} torr from a quartz crucible. The substrates were at room temperature. A shutter arrangement permitted deposition to occur only after the desired constant evaporation rate had been established. Ten separate runs, under identical conditions, were made. The films were deposited on glass, and on NaCl crystals. The glass substrates were degreased thoroughly and washed with deionized water. They were then placed in an ultrasonic cleaner containing hot trichloroethylene (TCE) for 15 minutes, and then rinsed with TCE followed by acetone and stored in methyl alcohol. The NaCl crystals were polished with running deionized water and rinsed with alcohol and also stored in methyl alcohol. The film thickness was determined by a Sloan Angstrommeter with an accuracy of $\pm 100 \text{ \AA}$. For films greater than 3μ the interferometric thickness was used to calculate the optical constants of the amorphous films. X - ray diffraction on two films indicated a vitreous structure. Transmittance was obtained using 10 different samples at room temperature, from $2.5\text{-}16 \mu$ using a Beckman model IR-10 spectrophotometer. All the data were taken under identical conditions with a reproducibility better than 1%. Optical absorption was measured at room temperature and at liquid nitrogen (LN_2) temperature from $0.7\text{-}2 \mu$ using a Carry model 14 spectrophotometer. For LN_2 measurements a specially constructed cryostat having a brass finger for sample mounting and with appropriate quartz windows for light transmittance, was placed in the sample compartment of the Carry 14. Absorbance curves were measured for 6 different samples at LN_2 temperature and for 10 different samples at room

temperature, one after the other, under identical conditions of Carry 14 settings. Because there might be a difference in composition from run to run due to the Variations in substrate temperature and evaporation rate, which were not controlled precisely during this study, the absorption coefficient was calculated for individual samples.

C. THEORIES

Analysis of the optical data can best be approached by first summarizing the various theoretical results and their relationships to the physical phenomenon of absorption. These results will be employed wherever applicable.

If no interference fringes are observed, the optical density D of a film is given by³

$$D = \alpha d / 2.3 \quad (1)$$

Here α is the absorption constant and d is the film thickness. This relation assumes double reflection at the film-air and substrate-film interfaces and an exponential law for the absorption process. The absorption coefficient α is related to the extinction coefficient k by

$$\alpha = 4\pi k / \lambda = 1.01 \times 10^5 k E \text{ cm}^{-1} \quad (2)$$

where λ and $E = h\nu$ are the free space wavelength and photon energy in electron volts, respectively. Thus, k can be found simply from the measured value of D

If α is small enough to allow the light wave to traverse the sample several times, interference fringes result in the transmittance response T . The values of the wavelengths at which T shows a maxima and minima can be used advantageously to determine the refractive index n . The condition for the occurrence of extremum values for T is⁴

$$4nd = m\lambda \left\{ 1 - \left[(\delta_{af} + \delta_{fs}) / \pi m \right] \right\} \quad (3)$$

(maxima for even m ; minima for odd m). Here, m is an interger. The parameters δ_{af} and δ_{fs} are phase angles due to reflections at the air-film (af) and film-substrate (fs) interfaces and are given by

$$\delta_{af} = \tan^{-1} \left[2k / (n^2 - 1 + k^2) \right] \quad (4a)$$

$$\delta_{fs} = \tan^{-1} \left[2n_1 k / (n^2 - n_1^2 + k^2) \right] , \quad (4b)$$

where n_1 is the refractive index of the nonabsorbing ($k = 0$) substrate. If k is small, the δ 's may be neglected. In our films, for $n = 2.26$, $k \approx 10^{-3}$ and

$n_1 = 1.50$ which are typical numbers; the values of δ_{af} and δ_{fs} are negligibly small ($< 10^{-3}$). Thus the simplified form of Eq. (3),

$$4nd = m\lambda \quad , \quad (5)$$

may safely be used to determine n , provided m is known. If the value of n does not change very rapidly with the wavelength as was found to be true in the present study, then by assuming $4nd = (m+1)\lambda_1$ and $4nd = (m+1)\lambda_2$ for two successive interference maxima, we find that

$$m = \lambda_2 / (\lambda_1 - \lambda_2) \quad (6)$$

Hence Equation (5) gives n at the various wavelengths.

The classical theory of absorption and dispersion of a free carrier gas in the amorphous state leads to the following expressions for the optical constants:⁵

$$n^2 - k^2 = \epsilon_\infty \left\{ 1 - \left(Nq^2 / m^* \epsilon_\infty \right) \left[\tau^2 / (1 + \omega^2 \tau^2) \right] \right\} \quad (7)$$

and

$$2nk = \left\{ \left(Nq^2 / m^* \omega \right) \left[\tau / (1 + \omega^2 \tau^2) \right] \right\} \quad (8)$$

Here q is the electronic charge, ϵ_{∞} is the dielectric constant arising from the combined effects of the bound charges, τ is the carrier density, and m^* is the effective mass of carriers. These equations may be simplified for the limiting cases of high and low frequencies. In the first case ($\omega^2 \tau^2 \gg 1$), and $n^2 \gg k^2$, Eq. (7) reduces to

$$n^2 = \epsilon_{\infty} \left\{ 1 - \left[\left(Nq^2 / m^* \epsilon_{\infty} \right) \left(1 / \omega^2 \right) \right] \right\} \quad (9a)$$

$$= \epsilon_{\infty} \left[1 - \left(\omega_p^2 / \omega^2 \right) \right] \quad (9b)$$

Here $\omega_p^2 = Nq^2 / m^* \epsilon_{\infty}$ is the plasma frequency.

For low frequencies ($\omega^2 \tau^2 \ll 1$) and Eq. (7) reduces to

$$n^2 = \epsilon_{\infty} \left(1 - \omega_p^2 \tau^2 \right) \quad (10)$$

Hence n^2 does not depend any more on λ (if τ is independent of the energy). τ is related to the free carrier mobility by the expression

When the energy of the incident photon exceeds the energy E (optical band gap) an electron can be directly excited from the valence band into the conduction band. In the case where the valence band maximum and the conduction band minimum appear at the same point in the Brillouin zone (namely at $k_{\omega} = 0$) the transitions from the oneband to the other are referred to as direct transitions between parabolic energy bands. The energy dependence of the absorption coefficient α near the edge of this fundamental absorption is then given by

$$\tau = m^* \mu / q \quad (11)$$

This relation, when plotted as α versus $h\nu$, will yield a straight line giving a value of E_{opt} by extrapolation to $\alpha = 0$.

$$\alpha \sim (h\nu - E_{\text{opt}})^{1/2} \quad (12)$$

D. RESULTS AND DISCUSSION

A typical transmission curve in a region extending from 2.5-16 μ is shown in Fig. 1. The transmission of the film continues to show interference fringes up to 16 μ , indicating that plasma resonance is absent in amorphous films. This is expected because, due to the highly disordered lattice, the time between collisions is considerably lowered so that $\omega\tau \ll 1$ should characterize such a damped system. As we shall see later, dispersion behavior of the refractive index at long wavelengths supports this conclusion.

Interference maxima in the transmittance curves were used to obtain the optical constants. The dispersion of the refractive index is illustrated in Fig. 2. The curve shows a relatively sharp increase towards the short wavelength region and approaches a constant value of 2.26 at long wavelengths, so that the relative dielectric constant $\epsilon = n^2 = 5.11$. This value is typical of the chalcogenide glass. The constancy of the refractive index at long wavelengths is characteristic of a highly damped system ($\omega\tau \ll 1$). Wavelength dependence of n may also be described by the limiting cases of the classical Eq. (7) for the short wave side and the long wave side as shown in Fig. 3. It is clear that n^2 is independent of λ in the long wave region, in good agreement with Equations (9) and (10) respectively. The transition between these two regions occurs at $\lambda_T = 3.08 \mu$ or $\omega_T = 6.14 \times 10^{14}$. According to the classical theory this frequency should be equal to the reciprocal mean free time $1/\tau$ of the free carriers. Therefore $\tau = 1.63 \times 10^{-15}$ sec. The intercept at $\lambda = \infty$ also gives $\epsilon_\infty = 12$. The magnitude of the mobility is determined by using Eq. (11) and is given by

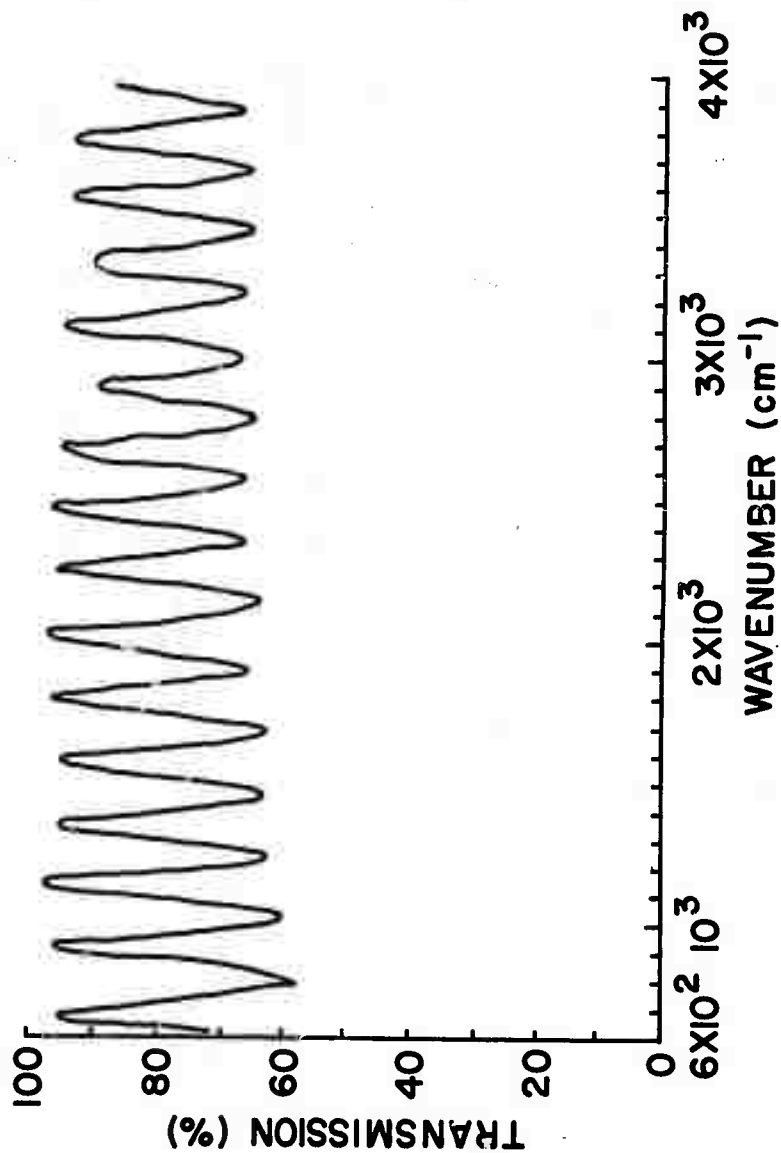


Fig. 1 Typical transmittance spectra of amorphous $\text{As}_2\text{Se}_3 \cdot \text{Sb}_2\text{Se}_3$ films deposited on NaCl at room temperature for sample P_2 .

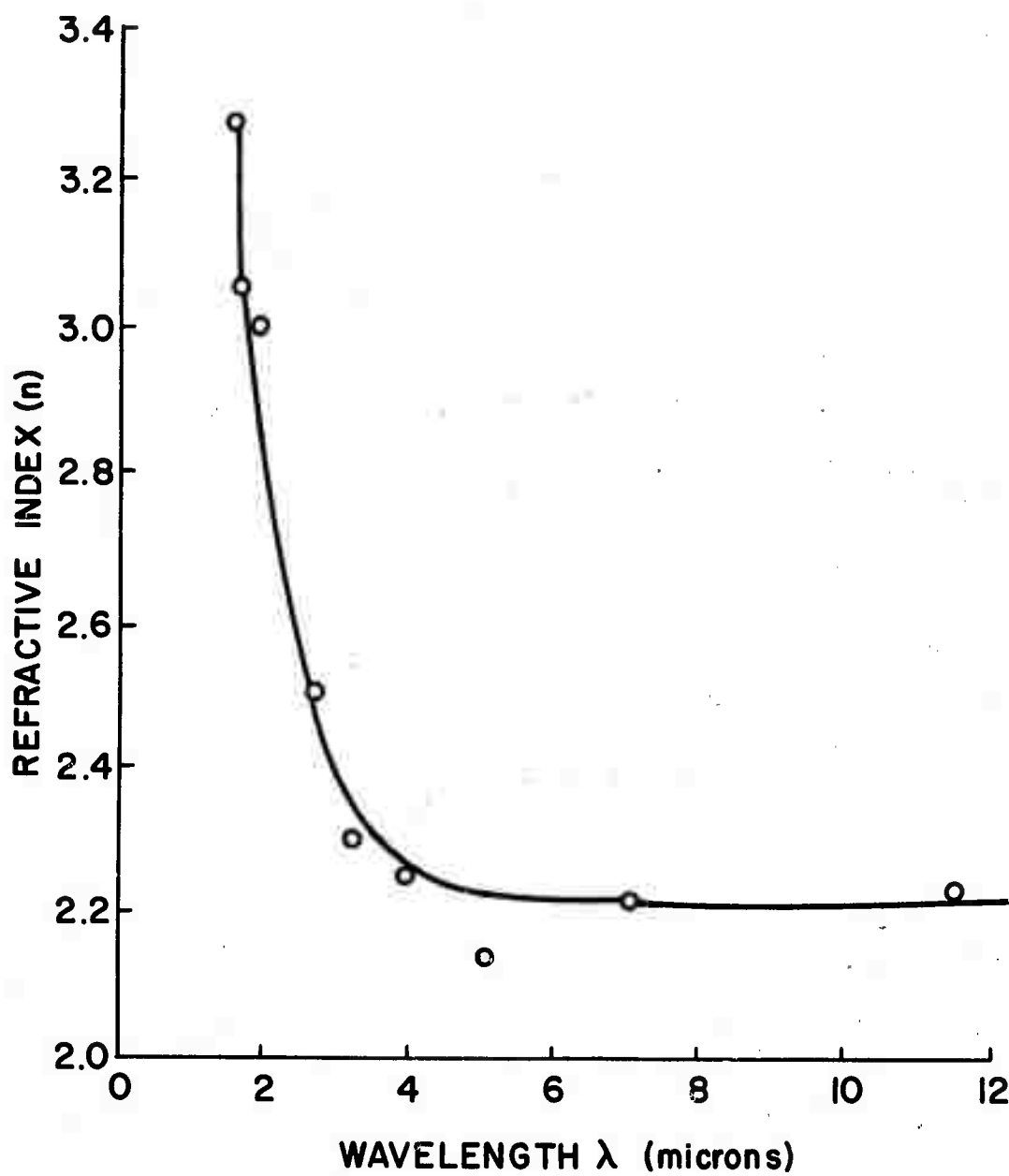


Fig. 2 Refractive index vs λ for sample P₂.

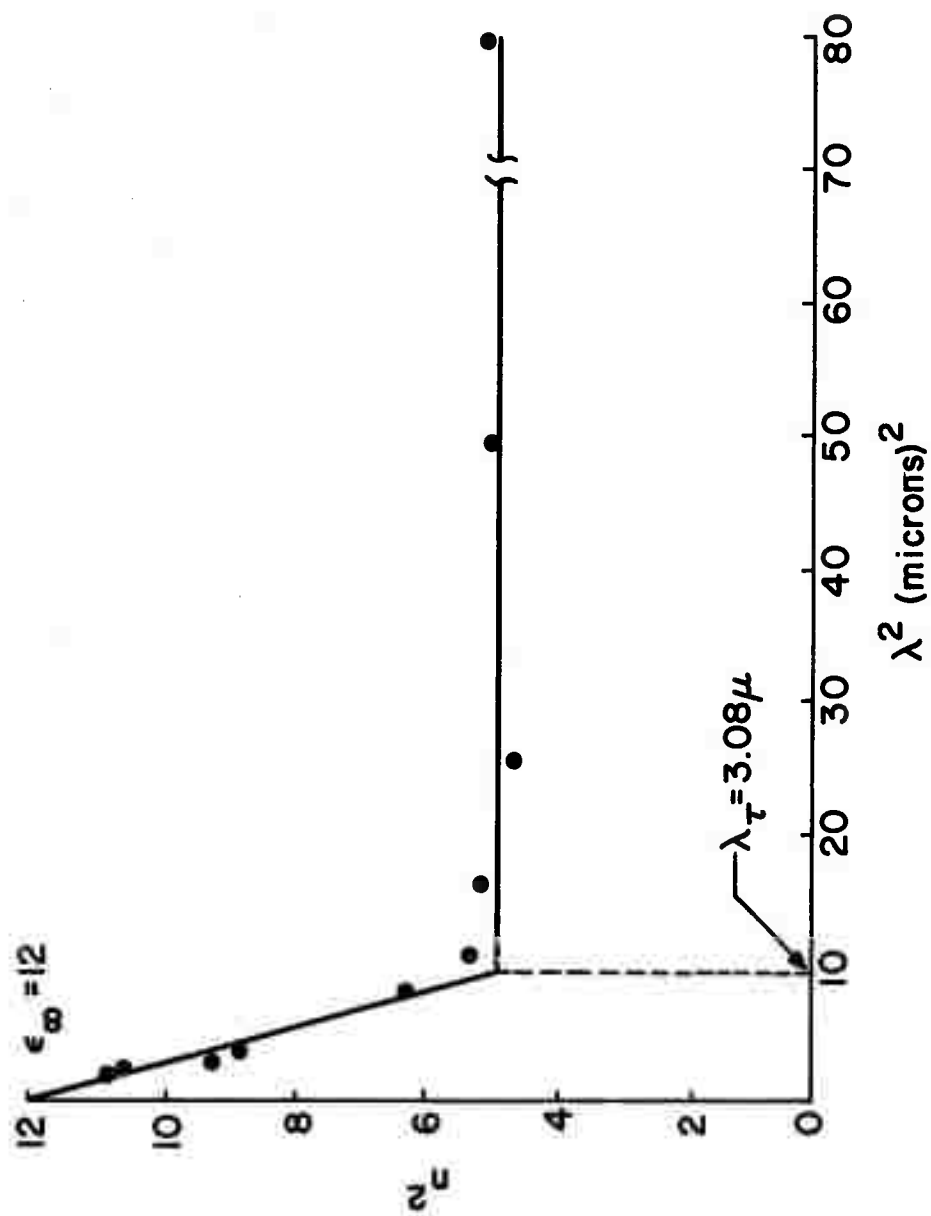


Fig. 3 Graph of $n^2 \sim \lambda^2$ for sample P_2 .

$$\mu = q\tau/m^* = 2.86 \text{ cm}^2/\text{Vsec} , \quad (13)$$

where $m^* = m$.

Figure 4 shows complete curves of the dependence of α on the photon energy obtained from the absorbance data below the interference effect regime, taken at room temperature and at LN_2 temperature. (Note that the energy range covered here is the same as that explored by Platakis et al.,⁶ on this composition in bulk form.) All the samples essentially follow the same law. Note that there is no observable exponential tail. This agrees with the data reported by Platakis et al.,⁶ on the same composition in bulk samples, and by Donovan and Spicer⁷ on amorphous germanium films. The observed $\alpha^2 \sim h\nu$ dependence indicates allowed direct (momentum conserved) transitions between the conduction and valence bands. When extrapolated to $\alpha = 0$, the optical-gap, averaged over 10 samples, is $E_{\text{opt}} = 1.442 \text{ eV}$ at room temperature and $E_{\text{opt}} = 1.558 \text{ eV}$ averaged over 6 samples at LN_2 temperature. Assuming that the absorption edge depends linearly on temperature (such a linearity has been assumed⁸ for As_2Se_3), the thermal coefficient of the absorption edge is $\beta = -5.3 \times 10^{-4} \text{ eV}/^\circ\text{K}$, which agrees with the value found by Kolomiets and Manontova⁹ for $4\text{As}_2\text{Se}_3 \cdot \text{As}_2\text{Te}_3$ glass.

In order to understand the observed optical behavior it is necessary to have a suitable band model. A plausible band structure consistent with both the optical and electrical data is proposed in Part II. For the present purpose it suffices to briefly describe the model consistent with the optical data. Unfortunately, there is no quantitative calculation available regarding the band structure of amorphous materials. Band models proposed so far are based on speculative assumptions that the band structure of the energy spectrum is essentially retained^{10,11} and is not determined by the long range order, but is dependent upon the short range order. The absence of long range order influences,

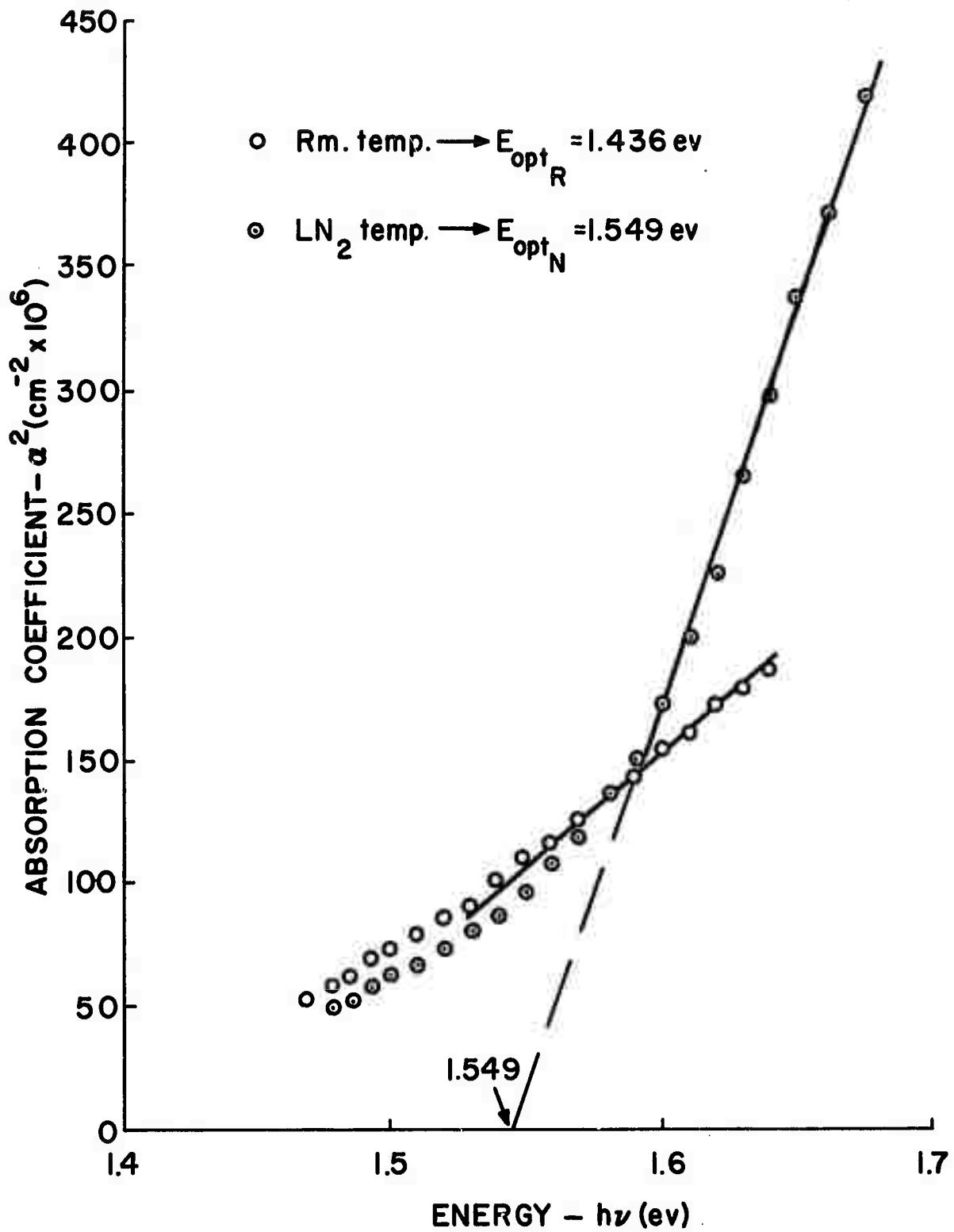


Fig. 4 Optical absorption data for sample -e₃.

however, the detailed shape of the band structure in that the band edges are not well defined, and there are present in the gap a large number of localized levels due to the random potential fluctuations at the atomic sites.¹² Localization presents low mobility because of trapping effects. Consequently, the region between the limits of the localized levels in the conduction and valence bands acts as a pseudogap, usually defined as the mobility gap.¹³ Thus by assuming a localization range equal to 1.50 eV (obtained from the electrical data in Part II), $\alpha^2 \sim h\nu$ dependence, that yields $E_{\text{opt}} = 1.442$ eV, can be explained as follows.

The optical absorption coefficient α is given by¹⁷

$$\alpha \sim \int P_{if}^2 N_c(E) N_v(E + h\nu) dE \quad (14)$$

Here P_{if} is the transition probability, and $N_c(E)$ and $N_v(E + h\nu)$ are the densities of states in the conduction and valence bands respectively. For transitions beyond the mobility gap i.e., involving the nonlocalized states only and based on the assumption that the range of the localized states is small, Eq. (14) is used to interpret the optical absorption data on amorphous germanium¹⁴ and selenium films^{15,16}. Optical transitions between two localized states are not likely to contribute to absorption because they are spatially separated. Transitions between occupied localized states in the valence band edge and nonlocalized empty states in the conduction band across the mobility gap edge could be important however, and these have not been considered by any of the above authors. In fact, the observed optical data, on amorphous As_2Se_3 - Sb_2Se_3 films investigated here, can indeed be interpreted in terms of these transitions. Assume that these transitions contribute to the absorption. It follows that a) $N_v(E) \sim E^{1/2}$, and that b) $N_c(E)$ is large near the mobility edge and can be taken as constant. Furthermore, the transition probability P_{if} , as observed from the data (see Fig. 4.) is constant.

Substituting these results in Eq. (14) shows that

$$\alpha \sim \left[h\nu - (E_{\text{opt}}) \right]^{1/2} \quad (15)$$

In the case of direct-allowed-transitions, the same dependence is found by Smith¹⁷ for crystalline semiconductors.

Equation (15) represents the data observed in Fig.4. This is in good agreement with the proposed band diagram in Part II.

E. SUMMARY AND CONCLUSION

The results of the optical investigations of 60% As_2Se_3 + 40% Sb_2Se_3 evaporated amorphous films may be summarized as follows:

1. The real part of the complex dielectric constant shows a few features that have been predicted by the classical theory of absorption and dispersion by free carriers; the square of the refractive index n^2 is proportional to λ^2 in the short wavelength region.
2. The transition between these two regions occurs at the frequency ω_t which is equal to the reciprocal mean free time $1/\tau$ of the free carriers. The value of $\tau = 1.63 \times 10^{-15}$ sec; was determined.
3. The mobility calculated from the value of τ is $< 5 \text{ cm}^2/\text{Vsec}$.
4. The absence of plasma resonance observed in the long wavelength region enabled us to calculate the value of the static dielectric constant, $\epsilon = n^2 = 5.11$.
5. The optical absorption was interpreted as being related to direct transitions involving the localized states in the conduction band. The optical energy gap extrapolated to $\alpha = 0$ is $E_{\text{opt}} = 1.442 \text{ eV}$.
6. The thermal coefficient of energy was found to be $dE_{\text{opt}}/dT = - 5.3 \times 10^{-4} \text{ eV}/^\circ\text{K}$.

REFERENCES

1. N. F. Mott, *Contemp. Phys.*, 10, 125 (1969).
2. J. G. Simmons, *Contemp. Phys.* 11, 21 (1970).
3. R.S. Knox, *Solid State Phys.*, Suppl. 5 (1963).
4. J. F. Hall and W.F. Ferguson, *J. Opt. Soc. Amer.* 45, 714 (1955).
5. F. Stern, *Solid State Phys.* 15, 300 (1963).
6. N. S. Platakis, V. Sadagopan, and H. C. Gatos, *Electrochem. Soc.* 116, 1436 (1969).
7. T. M. Donovan and W. E. Spicer, *Phys. Rev.* 2, 397 (1970).
8. J. T. Edmonds, *Brit. J. Appl. Phys.* 17, 979 (1966).
9. B. T. Kolomiets and T. N. Mamontova, *Sov. Phys. Doklady* 4, 417 (1959).
10. N.F. Mott, *Advan. Phys.* 16, 49 (1967).
11. A. I. Gubanov, *Quantum Electron Theory of Amorphous Conductors* (Consultants Bureau, New York, 1965).
12. N. F. Mott, *Phil Mag.* 19, 835 (1969).
13. M. H. Cohen, H. Fritzche, and S. R. Ovshinsky, *Bull. Amer. Phys. Soc.* 14, 311 (1969).
14. J. Tauc, *Optical Properties of Solids* (Plenum Press, New York, 1969), Chapter 5.
15. E. A. Davis, *Proc. 3rd Int. Conf. on Liquid and Amorphous Semiconductors*, Cambridge University (1969).

16. J. L. Hartke and P. J. Regensburger, Phys. Rev. 139, A970 (1965).
17. R. A. Smith, Semiconductors (Cambridge University Press, 1961).

PART II: ELECTRICAL PROPERTIES OF As_2Se_3 - Sb_2Se_3 FILMS

A. INTRODUCTION

During recent years, a physical model of the electrical structure of amorphous materials has evolved largely through the work of Mott,¹⁻³ Cohen, Fritzsche, and Ovshinsky⁴ and Cohen.^{5,6} Although the general features appear to be in agreement with experimental evidence, there still is a serious lack of experimental information related to the electronic transport properties. This part of the report is concerned with the results of measurements of electrical conductivity as a function of temperature, applied field, and illumination. The results of these studies, together with those of Part I, are interpreted in the light of a plausible energy-band diagram. Conductivity measurements and the spectral response allowed us to make a number of deductions about the electronic distribution and the transport mechanism.

B. EXPERIMENTAL DETAILS

The general experimental details for the preparation of amorphous $3\text{As}_2\text{Se}_3 \cdot 2\text{Sb}_2\text{Se}_3$ films have already been described in Part I. Specific details pertaining to the electrical measurements are described here. The films for electrical measurements were deposited by evaporation on ultrasonically cleaned Corning 0211 glass and on silicon wafers with a grown SiO_2 (about 1 Mm thick) insulating layer. The Si- SiO_2 substrates had a predeposited aluminum or gold stripe, 25 mils wide and 100 mils long, which was used for one contact to the film. For top electrodes, aluminum or gold dots of varying diameters were evaporated on the films deposited on Corning 0211 glass thus forming a sandwich structure. Three-mil diameter copper leads were attached to the contacts with highly conductive electronic grade Dupont 4922 silver paste. Electrical conductivity measurements in the temperature range of 230 to 370°K were performed using a Statham Model # SD6 oven with an accuracy of $\pm 1^\circ\text{C}$. Thirty to forty minutes were allowed to stabilize the temperature before any readings were taken. Current was measured using a Hewlett Packard Model 413-A micro-micro-ammeter connected in series with the sample. The majority of the measurements were made with a volt-drop of 1 V across the sample. High field data was obtained using the same setup except that a higher power supply was substituted. The photo spectral response was measured using an Aminco-Grating monochromator Model #4-8400 with a 650 W tungsten movie projector lamp. The light was focused on the back of the sample (semitransparent substrate) mounted inside the monochromator in order to eliminate any stray effects. One volt bias was used for most of the data.

C. RESULTS

1. Conductivity

Figure 1 shows a typical curve of conductivity versus $1/T$. Most of the data were on films with a bulk conductivity of about 10^{-9} mhos at room temperature. The conductance of these films was proportional to the area and inversely proportional to the thickness as would be expected for a well-defined conduction mechanism. Anomalous effects occurred in films of lower apparent conductivity. Some of these films showed an erratic "switching" behavior. The conductance then did not show a well defined dependence on film geometry. The conductivity follows an $\exp - [E/K_B T]$ relation with activation energy E . The value of the activation energy, obtained from the measurements averaged over ten samples, E , is 0.82 ± 0.02 eV.

2. Field Dependence of Conductivity

Conductivity for relatively high applied fields (5×10^5 V/cm maximum) and at different temperatures was measured. Semilog plots of I vs $V^{1/2}$ for a 1.35 Mm-thick $3\text{As}_2\text{Se}_3 \cdot 2\text{Sb}_2\text{Se}_3$ film at 296.5, 288, and 282°K are shown in Fig. 2. It is clear that at 296.5°K, the current varies according to $\exp[\beta_F V^{1/2}]$ for fields greater than about 7×10^4 V/cm. A similar variation is observed at other temperatures. The intersection of the three curves, when extrapolated to the high voltage region, yields an estimate of the breakdown field strength. The significance is discussed later.

3. Photoconductivity

The photo spectral response for a typical sample is shown in Fig. 3. The photocurrent is normalized to the per unit incident power. It is seen that thin films of $3\text{As}_2\text{Se}_3 \cdot 2\text{Sb}_2\text{Se}_3$ are sensitive photoconductors over the range of visible light.

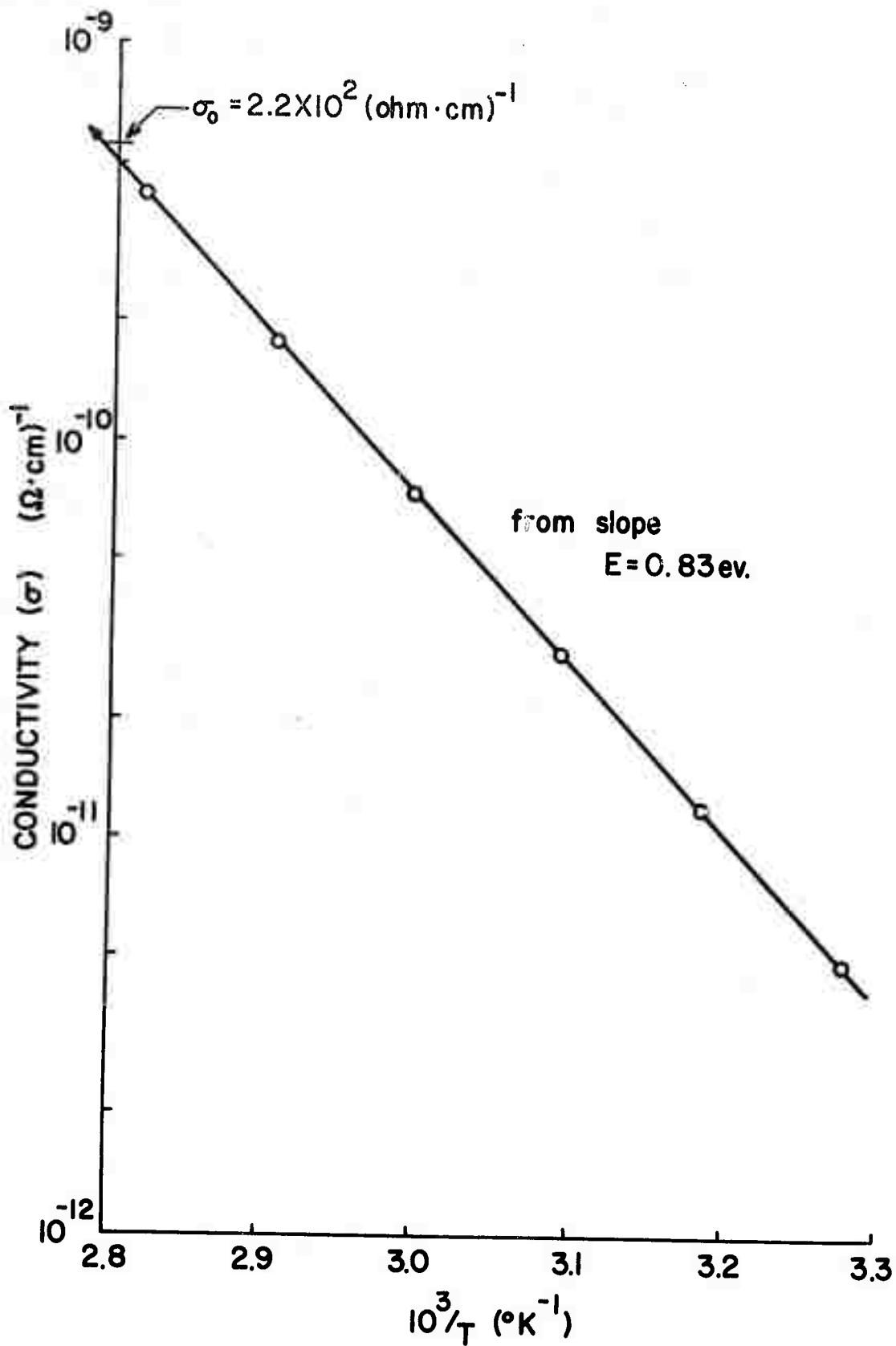


Fig. 1 Semilog plot of conductivity vs reciprocal temperature of an amorphous $3\text{As}_2\text{Se}_3 \cdot 2\text{Sb}_2\text{Se}_3$ film.

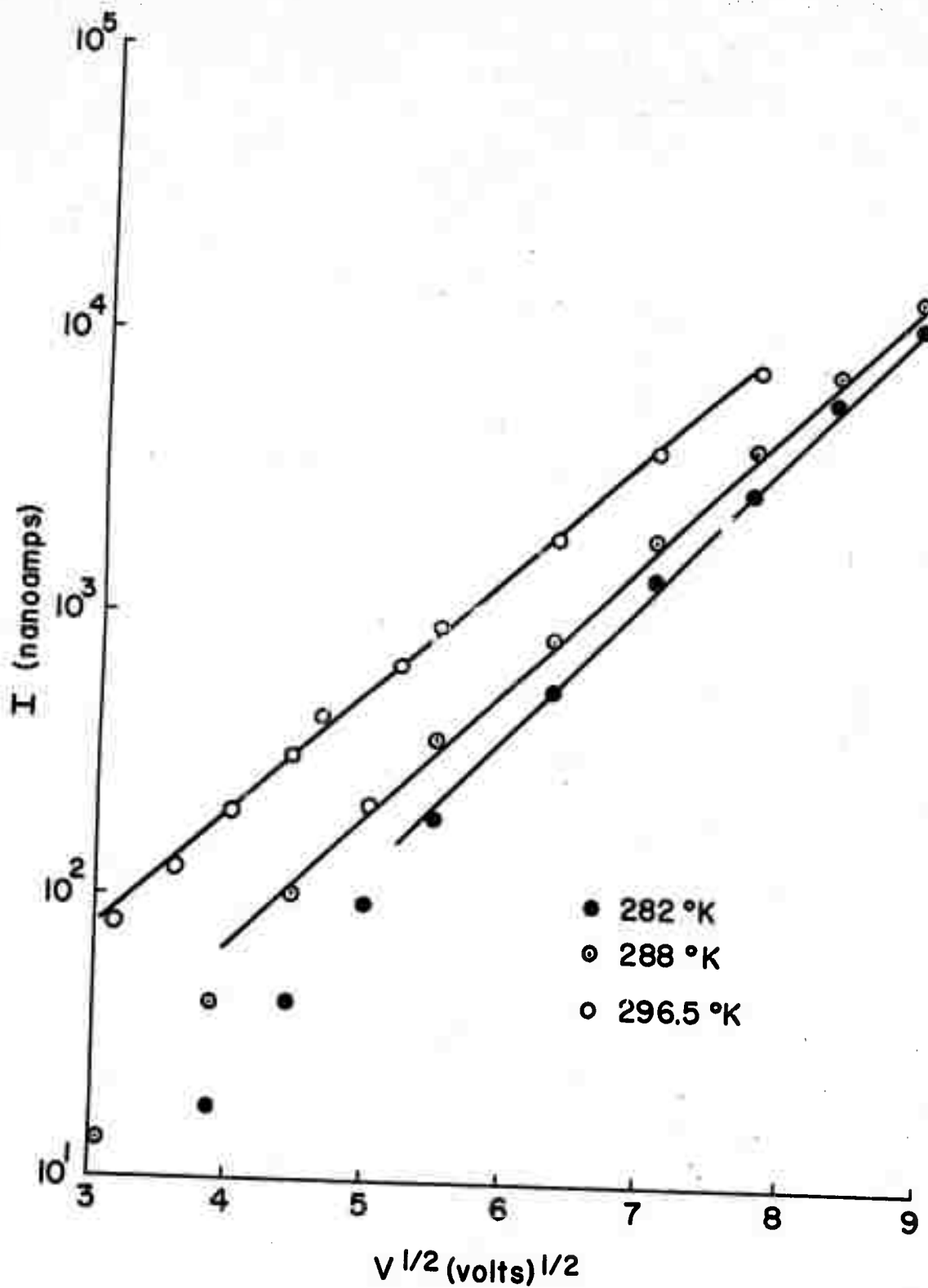


Fig. 2 Semilog plot of I vs $V^{1/2}$ for sample E_{3c} .

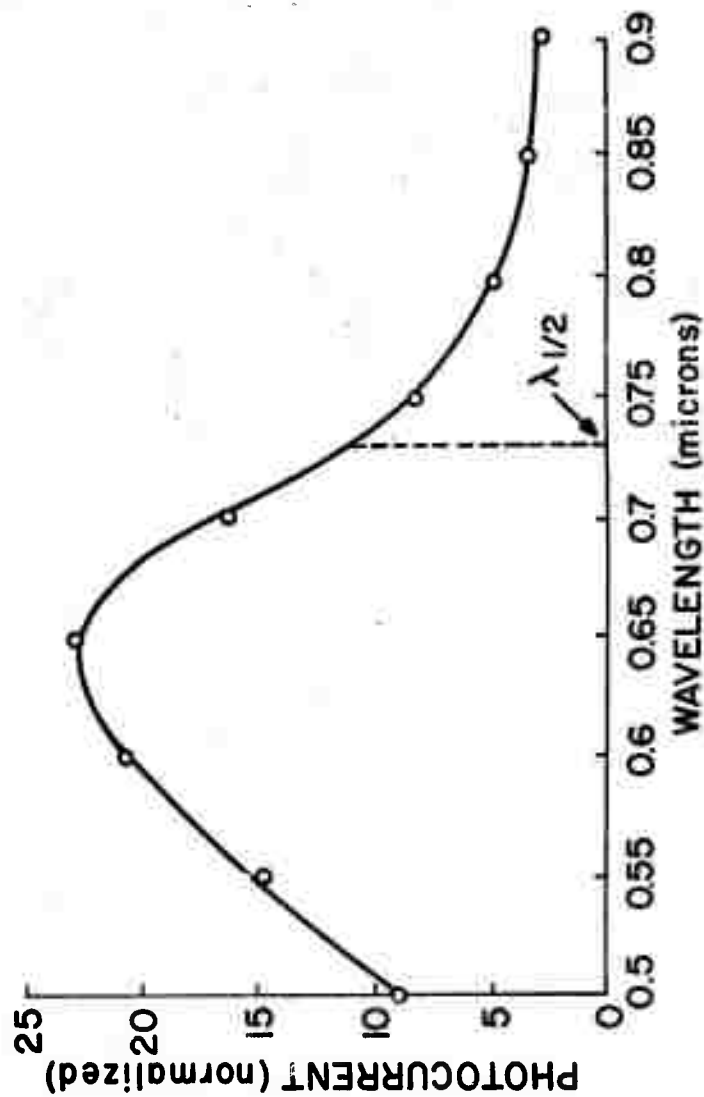


Fig. 3 Photoconductivity response per unit incident power vs wavelength for sample P.

DISCUSSION

In order to interpret the data on amorphous $2\text{As}_2\text{Se}_3 \cdot 2\text{Sb}_2\text{Se}_3$ films, it is necessary to have an energy-band diagram for the material. The usual derivation of an energy-band assumes an ideal periodic crystalline structure⁷. However, this assumption of long-range order is not required. The band structure of one and three-dimensional disordered lattices has been studied theoretically by Gubanov⁸, Mott¹⁻³,⁹ and others^{10,11}. The detailed⁸ analysis has shown that the essential features of the crystalline band structure are retained. However, the absence of long range order produces tailing (also called "smearing" or "fuzziness") of the band edges with a large number of localized states^{12, 13}. Consequently, the interval of localized states acts as a pseudogap and is usually defined as the "mobility gap"⁴.

1. Proposed Energy-Band Diagram

The proposed energy-band diagram is shown schematically in Fig. 4. An appropriate density-of-states diagram shown schematically in Fig. 5. It will be shown that this diagram is consistent with the experimental results.

2. Low Fields Conduction

According to the proposed band model, there can be two processes leading to conduction in amorphous $3\text{As}_2\text{Se}_3 \cdot 2\text{Sb}_2\text{Se}_3$ films: (a) An intrinsic excitation of nonlocalized states; and (b) a hopping process in the localized states. If it is assumed that the Fermi level lies at the middle of the mobility gap, the dc conductivity in the first case will vary as

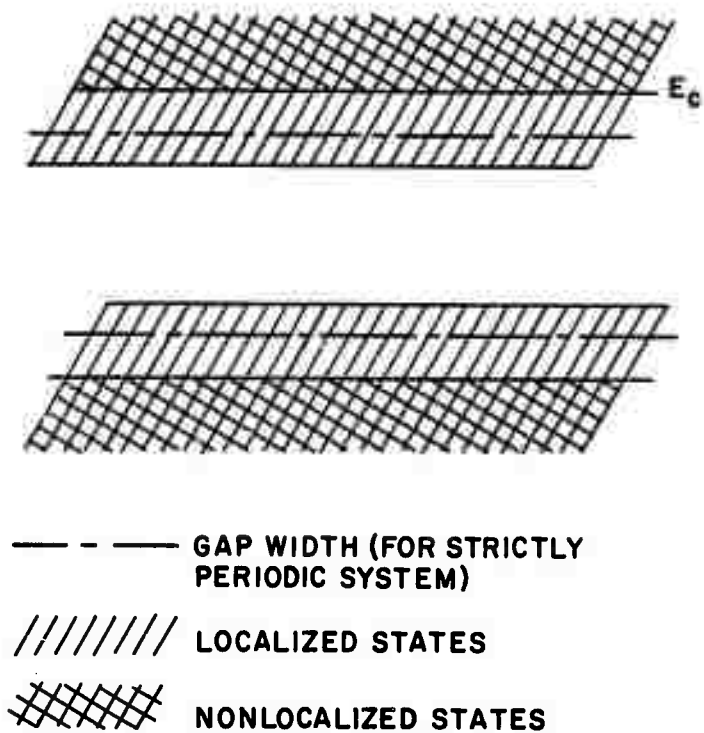
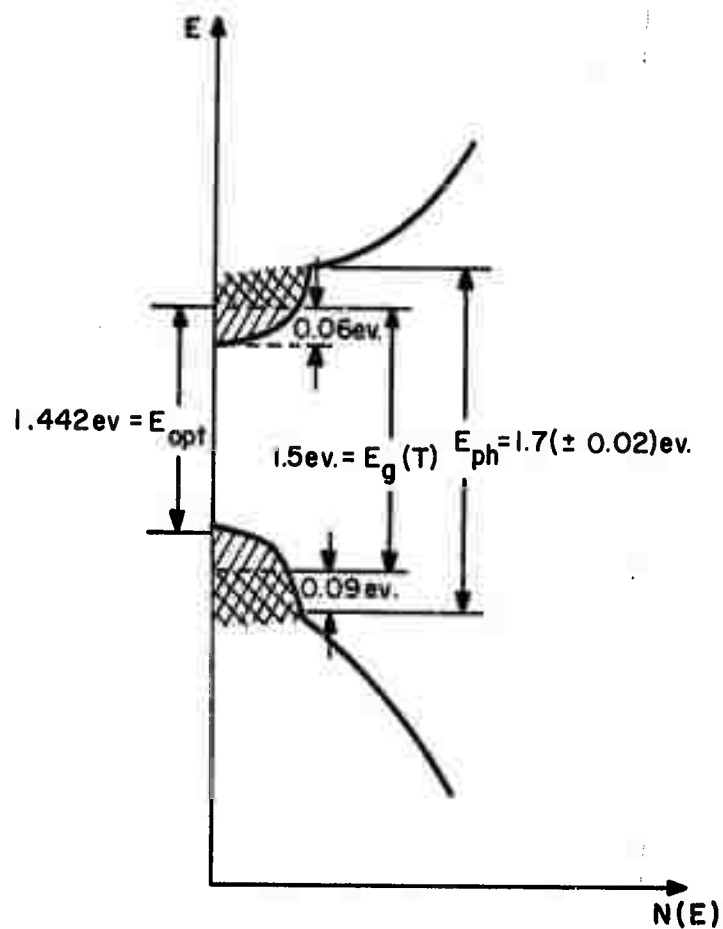


Fig. 4 Proposed energy band diagram of amorphous $3\text{As}_2\text{Se}_3 \cdot 2\text{Sb}_2\text{Se}_3$ films.



E_{ph} PHOTOCONDUCTIVITY GAP

E_{opt} ABSORPTION EDGE

$E_g(T)$ MOBILITY GAP

//// LOCALIZED REGION

XXXX NONLOCALIZED REGION

Fig. 5 Proposed density of states for amorphous $3\text{As}_2\text{Se}_3 \cdot 2\text{Sb}_2\text{Se}_3$ films.

where σ_0 is a slowly varying function of temperature, h is the Boltzmann constant, T is the temperature in degrees Kelvin, and $E_g(T)$ is the energy gap which generally depends on temperature^{14, 15}. If therefore, we write $E_g(T) = E_g(0) + \beta T$, where β is the temperature coefficient of energy, then Eq. (1) becomes

$$\sigma = \sigma_0 \exp -[\beta/2k_B] \exp -[E_g(0)/2k T] \quad (2)$$

Hence, with $E_g(0) = 2E \pm 1.64 \pm 9.92$ eV, and with $S = -5.3 \times 10^{-4}$ eV. $^{\circ}$ K (from optical data in Part I), the value of the energy gap, at room temperature, E_g , is 1.50 eV. In the second process, the conductivity caused by hopping would show a temperature dependence that could be expressed as

$$\sigma_H \sim \exp -[E_H/k T] \quad (3)$$

where E_H is the temperature dependent activation energy required for the hopping process. Experimental results^{16 - 18} indicate that E_H is generally very small (< 0.2 eV) and is not unique in value since it depends on the hopping length. Because our results show a unique and high activation energy, we conclude that phonon assisted hopping is not significant in amorphous $3As_2Se_3 \cdot 2Sb_2Se_3$, down to 230 $^{\circ}$ K. Many amorphous semiconductors show a behavior of type $\sigma \sim C \exp -[E(0)/k T]$ ¹⁹. This is similar in form to Eq. (2), if $C = \sigma_0 \exp -[\beta/k]$. For values of energy just on the nonlocalized side of E_C Mott's theoretical estimates show²⁰ values of σ_0 from $10 \cdot 10^3$, Hence C in the range $10^2 \Omega^{-1} \text{ cm}^{-1}$ is expected. The experimental value of C , found in the present work, is $2.20 \times 10^2 \Omega^{-1} \text{ cm}^{-1}$ (see Fig. 1). Mott and Davis²¹ show that if this mechanism (a) is predominant at room temperature, the range ΔE of localized states must be less than 0.2 eV. The present study yields $\Delta E = E_g - E_{opt} = 0.06$ eV (see Fig. 5). Furthermore, for such a transport behavior the upper limit to the mobility is expressed as²²

$$\mu \leq q a^2 \nu_{el}/kT \quad (4)$$

Here a is the interatomic distance; ν_{el} is the electronic frequency defined by $\nu_{el} = E_e/h$; E_e is the energy of the electron; and h is Planck's constant.

Typical values are $v_{el} = 10^{15}$ per sec and $a = 3 \text{ \AA}$. The value of the upper limit to this mobility is $\mu \leq 5 \text{ cm}^2/\text{Vsec}$. The deduced value of the mobility obtained from the optical data, in Part I, agrees reasonably well with this magnitude. It is clear from the above results that the exponential decrease in conductivity is due to intrinsic conduction across the mobility gap. The dc conductivity is also largely insensitive to the addition of impurities^{23, 24} and this is further evidence for intrinsic conduction.

3. High Field Conduction

It is a well established experimental fact^{25 - 27} that at fields in excess of some 10^4 V/cm , many dielectric films as well as amorphous semiconductor films^{18, 28, 29} exhibit current voltage characteristics of the form

$$I \sim \exp \left[\beta_F V^{1/2} \right] \quad (5)$$

with

$$\beta_F = \frac{q}{kT} \left(\frac{q}{\pi \epsilon \epsilon_0 d} \right)^{1/2}, \quad (6)$$

where I is the current in amperes, V is the voltage drop across the sample, ϵ is the relative dielectric constant, ϵ_0 is the dielectric constant of vacuum, and d is the thickness of the film. This is evidence of either the Schottky or the Poole-Frenkel (PF)³⁰ effect.

It is clear that the curves of Fig. 2 obey Eq. (5). The slope of the straight lines increases with decreasing temperature. This change is consistent with the PF theory. According to this theory the slope is determined from Eq. (6). For a typical temperature of 296.5°K , the value of this slope from the plot of Fig. 2 is 0.96. Using this value in Eq. (6), the dielectric constant is $\epsilon = 6.65$, which is a reasonable value compared to 5.11 obtained from the optical data. The lines extrapolated in the high field region meet at $V = V_B = 256 \text{ V}$.

This, then, yields the field strength for the electric breakdown, $F_B = 1.96 \times 10^6$ V/cm. The curves also indicate that the slopes of $\ln I$ versus $1/T$ have a tendency of increasing from negative towards zero. Hence, the correct form of Eq. (5) should be

$$I \sim \exp \left\{ \left[V_t - \left(\frac{q}{\pi \epsilon \epsilon_0 d} \right)^{1/2} \right] \frac{1}{kT} \right\}. \quad (7)$$

This evidence of a field enhanced thermal emission from a localized level or trap level at V_t . The depth of the trap level is determined from Eq. (7) using $V = V_B$, to be $V_t \approx 0.446$ eV.

The trap depth may correspond to a maximum in the statistical distribution of localized levels. These levels may be due to structural defects and short range order fluctuations³¹. Results of Kolomiets, et al.^{32, 33} for $Tl_2SeAs_2Te_3$ and As_2Se_3 glasses also show evidence of trap levels. The physical model, in agreement with the observed high field transport behavior, for $3As_2Se_3 \cdot 2Sb_2Se_3$ films is schematically displayed in Fig. 6.

4. Photoconductivity

The spectral response of the photoconductivity is displayed in Fig. 3. There is no wavelength at which the response vanishes completely. In such a case the band gap is defined³⁴ as the energy at which the response has fallen to half value. This yields $E_{ph} = 1.70 \pm 0.02$ eV as the photoconductivity gap, and implies an intrinsic gap because the absorption due to localized states would not give rise to photoconductivity.

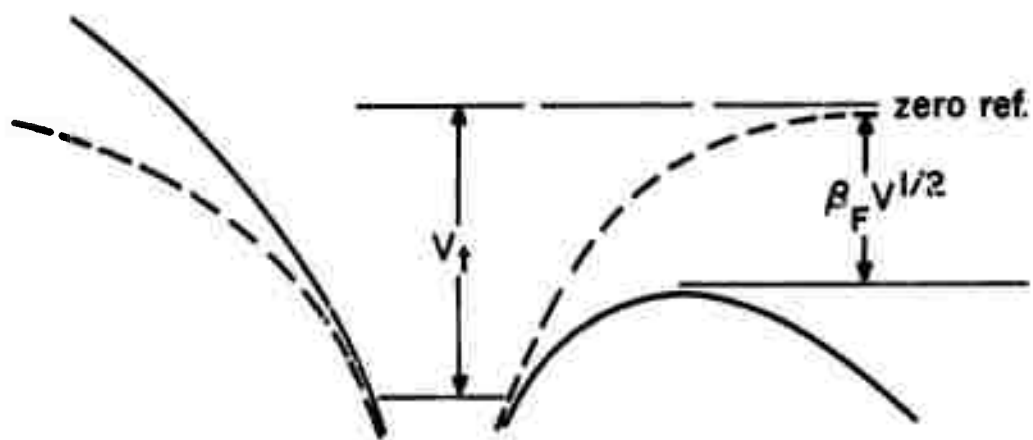


Fig. 6 High field emission model.

V. SUMMARY AND CONCLUSIONS

The results of the electrical investigations of $3\text{As}_2\text{Se}_3 \cdot 2\text{Sb}_2\text{Se}_3$ evaporated amorphous films may be summarized as follows:

1. The observed dc conductivity was found to be consistent with intrinsic semiconducting behavior.
2. A thermal activation energy (mobility gap) at room temperature $E_g = 1.50$ eV was found.
3. The high field conductivity was found to obey the field enhanced thermal emission (PF law) from a deep trap at 0.446 eV.
4. The dielectric constant estimated from the PF-mechanism agreed reasonably well with that determined from the optical data.
5. The photoconductivity was observed to be intrinsic, yielding the band gap. $E_{ph} = 1.70 (\pm 0.02)$ eV at $\lambda_{1/2}$.

The important optical and electrical parameters of amorphous $3\text{As}_2\text{Se}_3 \cdot 2\text{Sb}_2\text{Se}_3$ films obtained during this investigation are compiled in Table I.

Table 1. Summary of the measured electrical and optical constants of amorphous $3\text{As}_2\text{Se}_3 \cdot 2\text{Sb}_2\text{Se}_3$ films.

| | |
|---|-------------------------|
| Resistivity (ohm-cm) at 300°K | $\approx 10^9$ |
| Mobility ($\text{cm}^2 \text{V}^{-1} \text{sec}^{-1}$) at 300°K | < 5 |
| Optical band gap (eV) at 300°K | 1.442 |
| Optical band gap (eV) at 77°K | 1.568 |
| Temperature coefficient of optical band gap (eV/°K) | -5.3×10^{-4} |
| Electrical band gap (eV) at 300°K | 1.50 |
| Breakdown strength (V/cm) | $\approx 2 \times 10^6$ |
| Photoconductivity gap (eV) at 300°K | 1.7 (± 0.02) |
| Refractive index (at 5 μ and 300°K) | 2.26 |
| Dielectric constant (static) | 5.11 |
| Relaxation time (sec) | 1.63×10^{-15} |

REFERENCES

1. N. F. Mott, Advan. Phys. 16, 49 (1967).
2. N. F. Mott, Phil. Mag. 19, 835 (1969).
3. N. F. Mott, Contemp. Phys. 10, 125 (1969)
4. M. H. Cohen, H. Fritzsche, and S. R. Ovshinsky, Phys. Rev. Letters 22, 1065 (1969).
5. M. H. Cohen, J. Non-Crystalline Solids 2, 432 (1970).
6. M. H. Cohen, J. Non-Crystalline Solids 4, 391 (1970)
7. R. Ke L. Kronig, and W. G. Penney, Proc. Roy. Soc. (London) A130, 499 (1931)
8. A. I. Gubanov, Quantum Electron Theory of Amorphous Conductors (Consultants Bureau, New York, 1965).
9. N. F. Mott, Phil. Mag. 17, 1259 (1968).
10. K. Morjani and C. Feldman, Rev. Mod. Phys. 36, 1042 (1964).
11. L. Banyai, Proc. Int. Conf. Phys. of Semiconductors (Dunod, Paris, 1964), p. 417
12. I. M. Lifshitz, Advan. Phys. 13, 483 (1964).
13. B. I. Halperin and M. Lax, Phys. Rev. 148, 722 (1966).
14. J. T. Edmonds, Brit. J. Appl. Phys. 17, 979 (1966).
15. E. A. Davis, Int. Conf. on Amorphous and Liquid Semiconductors (Cambridge University, England, 1969), Unpublished.
16. A. H. Clark, Phys. Rev. 154, 750 (1967).
17. P. A. Walley and A. K. Johscher, Thin Solid Films 1, 367 (1967-68).
18. P. A. Walley, Thin Solid Films 2, 327 (1968).

19. J. Stuke, J. Non-Crystalline Solids 4, 1 (1970).
20. N. F. Mott, Phil. Mag. 22, 1 (1970).
21. E. A. Davis and N. F. Mott, Phil. Mag. 22, 903 (1970).
22. M. H. Cohen, Int. Conf. on Amorphous and Liquid Semiconductors (Cambridge University, England, 1969), Unpublished.
23. B. I. Kolomiets, and T. F. Nazarova, Sov. Phys. Solid State 2, 159 (1960),
24. I. Z. Fisher, Sov. Phys. Solid State 1, 171 (1959).
25. C. A. Mead, Phys. Rev. 128, 2088 (1962).
26. H. Hurose and Y. Wada, Japanese J. Appl. Phys. 4, 639 (1965),
27. T. E. Hartman, J. C. Blair, and R. Bauer, J. Appl. Phys. 37, 2468 (1966).
28. R. C. Chittick, J. H. Alexander, and H. F. Sterling, J. Electrochem. Soc. 116, 77 (1969).
29. P. J. Stiles, L. L. Chang, L. Esaki, and R. Tsu, Appl. Phys. Letters 16, 380 (1970).
30. J. Frenkel, Tech. Phys. USSR 9, 685 (1938).
31. A. I. Gubanov, Sov. Phys. Solid State 4, 2104 (1963).
32. B. T. Kolomiets, E. A. Lebedev, F. T. Mazec, T. N. Mamontova, and G. I. Stepanov, Int. Conf. Phys. of Semiconductors (Dunod, Paris, 1964), p. 1283.
33. B. T. Kolomiets, T. N. Mamontova, and G. I. Stepanov, Sov. Phys. Solid State 9, 19 (1967).
34. T. S. Moss, Photoconductivity in the Elements, (Butterworths Sci. Publication, 1952).

III. Measurement Techniques (R. W. Gould and L. L. Hench)

A. QUANTITATIVE USE OF GUINIER X-RAY CAMERAS IN SOLID STATE REACTION KINETICS

By

D. E. Clark, G. J. Scott and L. L. Hench

Introduction

Many investigators have examined the kinetics of solid state reactions. The methods employed usually consist of either an optical microscopic determination of reaction layer thickness in diffusion couples^(1,2) or quantitative x-ray analysis using standard x-ray diffractometer methods.⁽³⁻⁶⁾ Both of these methods limit the analysis of the reacting materials to the later stage of reaction where the fraction of product formed is greater than about 3 weight percent. However, in many areas of current research interests, the identification of less than 3 percent of a phase is crucial to the characterization of the microstructure, properties and behavior of ceramic materials.

Several examples of the areas where the examination of the products of early stages of reactions are important include: devitrification of glasses, metastable phases and nuclei in glass-ceramics, interfacial compounds in composite materials, oxidation products, grain boundary compounds, sintering additives, precipitates from solid solution, fission products and inorganic compound nucleation in biological systems.

For the purposes of this paper, early-stage reactions are defined as those that involve nucleation, surface diffusion and interfacial rearrangements and which are not lattice diffusion controlled; consequently the fraction of reaction product involved is quite small. Later-stage reactions are defined as those that involve lattice diffusion processes and therefore the fraction of reaction product is usually appreciable.

The objective of this paper is to establish a method for the quantitative analysis of solid state reaction kinetics through the use of Guinier-deWolff and Guinier-Lenné x-ray cameras. Analysis of early-stage solid state reactions requires the use of the Guinier-deWolff x-ray camera. A method for employing a high temperature Guinier-Lenné x-ray camera in the analysis of later-stage solid state reactions is also presented. And finally, the range of applicability of the Guinier cameras in comparison with other x-ray techniques is experimentally established.

Solid State Reaction Kinetics

Numerous diffusion models have been proposed for describing the later stages of solid state reaction kinetics involving two reactants. It has been experimentally established by Branson⁽³⁾ that the most realistic of the various models was developed by Valensi⁽⁸⁾ and Carter.⁽⁹⁾ The model is unique in that it allows for the volume difference between reactants and products. The following equation was used by Valensi for describing the oxidation kinetics of nickel spheres.

$$K't = \frac{\Delta}{\Delta-1} - (1-\alpha)^{2/3} - \frac{1}{\Delta-1} [1 + (\Delta-1)\alpha]^{2/3} \quad (1)$$

where K' = the reaction rate constant for a given temperature,
 t = the reaction time,
 Δ = the volume of product formed per unit volume of reactant consumed, and
 α = the reacted fraction of the reactants.

Branson⁽³⁾ has shown that equation (1) is valid for describing the later-stage kinetics of the $\text{ZnO-Al}_2\text{O}_3$ system. His data, when plotted on a graph of $K't$ versus t , yielded a curve with constant slope that extrapolated through the origin for $t = 0$. The significance of these results is that K' is indeed a constant for a given temperature and, furthermore, the initial conditions are satisfied because initially no product is indicated to be present. Other models fail to satisfy both of these requirements. The Valensi model has also been used successfully by Duncan and Stewart⁽¹⁰⁾ for describing the kinetics of zinc ferrite formation. For these reasons the Valensi-Carter model will be used throughout the development of the later-stage reaction techniques in this paper.

Early-stage solid state reactions have not been examined as extensively as later-stage reactions. This is primarily because adequate equipment has not been available for quantitative analysis of very small fractions of the product phase, i.e., <3 percent. In fact, little early-stage reaction kinetics data have been collected for any system to the authors' knowledge, even though several early-stage models have been proposed.^(3,6) For this reason, the authors suggest that selection of an appropriate kinetics model is an integral part of early-stage kinetics evaluation. Thus, in later discussions "early-stage model" is used in its general sense.

Description of the Two Guinier Cameras

X-ray identification of crystals produced in the early stages of a reaction sequence can be obtained through the use of a vacuum Guinier-deWolff camera. The camera is an evacuated powder camera with a monochromatic x-ray beam incident on the specimen. The focused beam, specimen and film are arranged so as to produce a focusing circle (Figure 1).⁽¹¹⁾ The film is on the circumference of this circle, and a 7-inch filmstrip subtends the arc between approximately -1° and $45^\circ \theta$. The focusing circle has an effective radius of 114.6 mm, so that

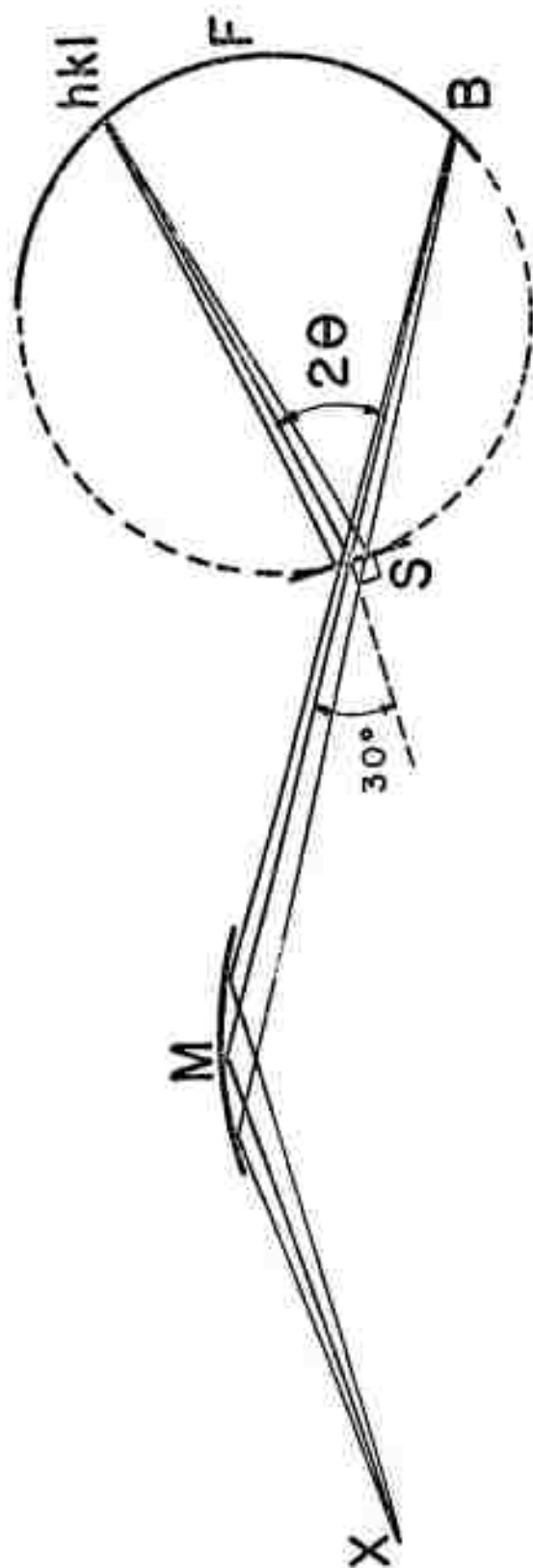


Figure 1. Schematic of Guinier camera x-ray optics. The "X" denotes the line source of an x-ray tube, "M" the monochromator crystal, "S" the sample, "B" the focus of the main beam, "F" the film, and "hkl" the focus of a diffracted beam.

4 mm on the film corresponds to 1° of Bragg angle. Important characteristics of the camera are: (1) high resolution due to eliminating the white radiation background; (2) high intensity from a monochromatic beam focused by a bent quartz single crystal; (3) reduced air scattering background; (4) a larger, more representative sample volume; and (5) four powder samples are exposed simultaneously to x-ray irradiation.

The wavelength of radiation on all four sample holders is the same, but an intensity decrease on the two outer samples results in a lesser photographic density from them. The photographic effects can be empirically normalized to those of the center pair by testing a film of four quantitative samples of the same substance.

The Guinier-Lenné camera, in contrast, holds only one sample, but employs a furnace and a moving film cassette. The x-ray optics are the same as for the Guinier-deWolff camera, but the x-rays pass largely through the ambient atmosphere as only approximately 3 cm on either side of the sample is evacuated. Both incident and diffracted beams pass through beryllium windows that transmit 83 percent of incident $\text{CuK}\alpha$ x-rays. The furnace is platinum-rhodium resistance heated, and its shell is water cooled. The film cassette moves normal to the focusing plane of the x-rays, which permits reaction effects to be recorded on film as they occur. Consequently, one of the most important features of the Lenné camera is that it permits the study of high temperature reactions in-situ. For example, the Lenné camera is especially useful for analyzing: (1) thermal expansion vs. temperature curves, (2) temperatures of phase changes, (3) crystallization of amorphous substances, (4) decomposition reactions, and (5) solid state reactions.

The temperature of the Guinier-Lenné camera may be set up to 1200°C for isothermal runs for an indefinite time period, or motor driven variacs may be engaged to cause the furnace to heat from a preselected low temperature to any higher one at a controlled rate, or for a similarly controlled cooling cycle.

The sample holder temperature is read using a built in Pt-Pt-10Rh thermocouple, which is fed through the vacuum chamber wall.

The elapsed times between initiation and completion temperatures can be selected to be 3, 4, 6, 12, 30, 40, 60 or 120 hours. Rates of film advance available are 0.1, 1.0, 1.5, 2.5, 10, 15 and 20 mm/hour, and slit widths of 1, 3 and 5 mm can be used. Consequently, a large variety of exposure times are obtained by varying the slit widths and the rate of film advance.

Several potential complications in the use of both Guinier cameras include: (1) varying or uncontrolled particle orientation can yield misleading results, especially when examining small fractions, and (2) the presence of $\lambda/2$ radiation can cause both extra lines on the film and can excite characteristic fluorescence of the sample, thus limiting the exposure time. However, it is well-known that these problems are not unique to Guinier cameras and occur with other x-ray methods as well.

The choice of film greatly affects the sensitivity and/or convenience of both Guinier systems. As can be noted from Table I, very long exposure times may be required to obtain quantitative data when very small percentages of compounds are involved, even when an extremely fast x-ray film is used. A trade-off must be made between the available contrast for a low-to-moderate photographic density of the analysis line over background, and the time required to create its image. Kodak No-Screen offers a satisfactory compromise for most applications. The film type giving the next significant step up in contrast from Kodak No-Screen, Kodak AA, requires six times longer exposures.⁽¹²⁾ An additional advantage of the smaller grain size of the slower, higher contrast film types is that it gives a smaller noise amplitude and period, which assists interpretation of microdensitometer graphs.

Although the films of either Guinier camera can be read with standard optical x-ray readers, a Joyce-Loebl recording microdensitometer provides maximum accuracy in analyzing the exposed film. Such accuracy is especially important in early-

stage kinetic studies. This two-beam, continuous wedge instrument features accurately controllable specimen beam intensity, and electronically monitored scanning speed for optimum pen response. A set of levers produce adjustable graph-distance to film-distance ratios. For instance, the breadth of a peak produced on the densitometer output graph will be 100 times the breadth of the same peak on the film when the 100 lever is used. Lever ratios of 1,000:1, 200:1, 100:1, 50:1, 20:1, 10:1, 5:1, 2:1 and 1:1 are available. Examples of a 1:1 lever ratio trace and a 200:1 trace from a film produced in a Guinier-deWolff camera are shown in Figure 2.

Quantitative Sample Preparation

The diffracted intensity equation for Guinier cameras given by Sas and deWolff⁽¹³⁾ is

$$I = LABS G T k p F^2 P \quad (2)$$

$$\text{where } L = \frac{1}{\sin^2 \theta \cos \theta}, \text{ the Lorentz factor for Guinier cameras, and} \quad (3)$$

A is the absorption correction factor which is expressed as

$$A = \frac{1}{\mu d} \frac{\cos \psi \cdot \cos X}{\cos \psi - \cos X} [\exp(-\mu d / \cos \psi) - \exp(\mu d / \cos X)] \quad (4)$$

$$\text{for } X = |2\theta - \psi| \quad (5)$$

where 2θ = Bragg diffraction angle,

ψ = 30° for commercial Guinier cameras,

μ = the linear absorption coefficient for x-rays, and

d = the sample's thickness.

In equation (2) B, the absorption factor for the film's paper wrapper, is

$$B = \exp[-\mu_p d_p / \cos X]. \quad (6)$$

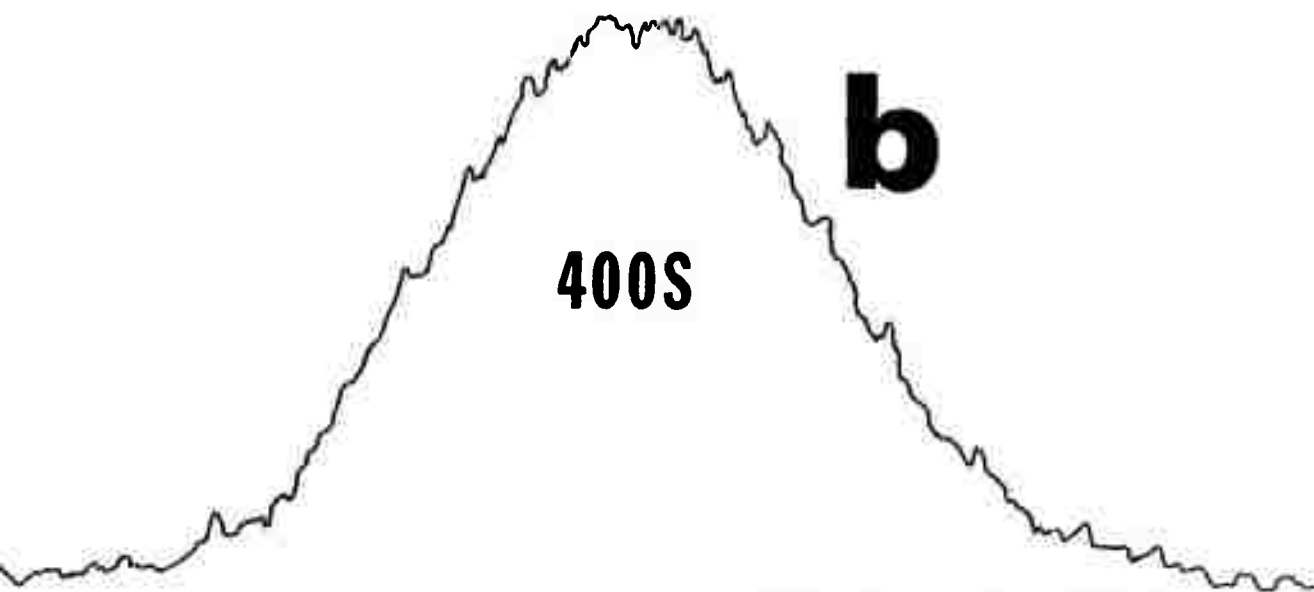
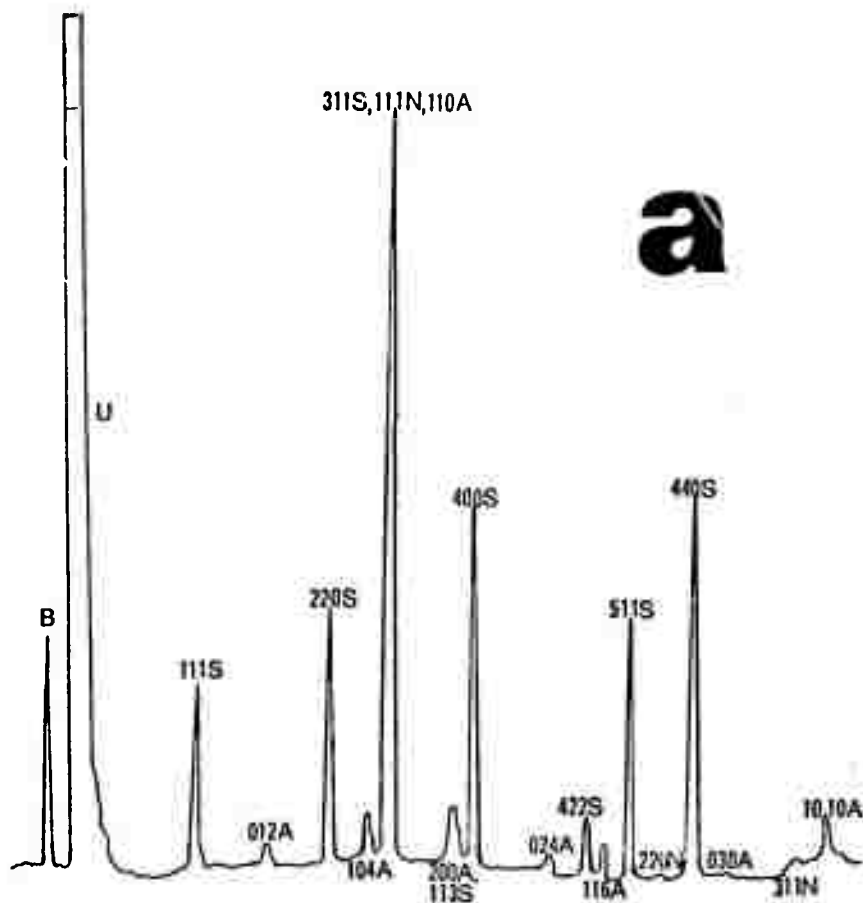


Figure 2a. Microdensitometer trace of Guinier-Lenné camera film, 1:1 level ratio, 90 weight percent NiAl_2O_4 spinel ("S"), 3 weight percent Al_2O_3 ("A"), and 2 weight percent NiO ("N"). The main beam is marked by "B" and the untrapped small angle scattering by "U".

b. 200:1 level ratio trace of 400 NiAl_2O_4 peak from Guinier-deWolff camera film, 65 weight percent spinel.

Kodak No-ScreenTM film was used for both exposures.

The absorption by the Be diffracted-beam window in the Guinier-Lenné camera furnace body is also calculated from formula (6), as should be the atmospheric absorption between the window and the film.

In equation (2) the second emulsion factor for integrated intensities, S , is

$$S = \frac{[1 - \exp\{-(\mu_1 d_1 / \cos X)\}]}{[1 - \exp(-\mu_1 d_1)]} \times \frac{[1 + \exp\{-(\mu_1 d_1 + \mu_2 d_2) / \cos X\}]}{[1 + \exp\{-(\mu_1 d_1 + \mu_2 d_2)\}]}, \quad (7)$$

giving the effective intensity exposing double emulsion films. The hkl beam intensity reaching the rear emulsion has been reduced by passing through the front emulsion and the base. In equation (7) the thickness of one layer of emulsion and of base are d_1 and d_2 respectively, and μ_1 and μ_2 are the corresponding absorption coefficients.

The geometric factor accounting for the oblique incidence of diffracted beams onto the film is given by

$$G = 1/\cos X \quad (8)$$

T , k , p , F^2 and P used in equation (2) are the standard powder camera temperature, scale, multiplicity, structure and polarization factors, respectively.⁽¹³⁾

For optimum quantitative use of the Guinier cameras, it is essential to use high density samples that are consistent in both weight and texture. The major factor involved in achieving optimal samples is the absorption correction factor, which contains much of the sample's effects on diffracted intensity, since it alone contains the sample's x-ray opacity (" μd " product), see equation (4).

We specify the problem by defining the sample's thickness as being the total powder weight per unit area of sample holder, divided by the resulting actual bulk density, i.e.,

$$d = \frac{W/A_s}{\rho'} \quad (9)$$

Next, by summing each phase's absorptivity (μ_1^n), adjusted for the weight fraction present, one obtains a total absorptivity

$$\mu = \sum_{n=1}^Q \left(\sum_{i=1}^E \mu_i \frac{w_i^n}{w_n} \right) \frac{w_n}{W} \quad (10)$$

In equation (10) Q and E are the total numbers of phases and elements, μ_i is the absorptivity of the i^{th} element, w_i^n is the actual weight of the i^{th} element in the n^{th} phase, and w_n is the total weight of the n^{th} phase.

Furthermore, the structure, multiplicity and Lorentz factors can be combined into a scattering coefficient per unit weight since these terms contribute to the diffracted intensity from any specimen. The number of effective electrons in the phase, which do the work of diffracting x-rays, is proportional to the weight of the phase in question. The structure factor counts these electrons and accounts for the interference the hkl beam encounters from the x-ray scattering of all the atoms in the unit cell. The multiplicity factor gives the number of equivalent planes which can cause a given reflection. Thus a 100 beam from a cubic crystal can be excited from [100], $[\bar{1}00]$, [010], $[0\bar{1}0]$, [001] and $[00\bar{1}]$ planes, so the multiplicity factor is 6. The Lorentz ("velocity") factor's value is controlled by the rate that the hkl node of the reciprocal lattice penetrates the Ewald sphere. Reference 14 gives a complete discussion.

Introducing the Bragg-angle-dependent structure and Lorentz factors, of course, limits our discussion to the diffracted intensity of a single line. We thus restrict θ to the value given by $\arcsin(\lambda/2d_{hkl})$, and we restrict the line with indices "hkl" to be the one whose variation of photographic density with weight of product phase will be the analytical basis of kinetics studies.

Thus the diffraction intensity is proportional to

$$I \propto \frac{\sigma_m^W hkl}{\mu d} \left[\exp\left(\frac{-\mu d}{\cos \psi}\right) - \exp\left(\frac{-\mu d}{\cos X}\right) \right], \quad (11)$$

for a mass scattering coefficient σ_m and a weight of material W_{hkl} properly oriented to diffract the hkl line. Note that the diffracted intensity now depends on the weight of diffracting material in a complex way (equation (9)). For a single phase sample, the intensity value is dominated by the μd product of the denominator, i.e., the difference of exponentials rises slowly for typical Bragg angles, while the graph of the whole function falls monotonically and approaches the opacity axis for large μd . Thus, there is no optimum sample weight for single phase samples.

For multiphase samples, the direct proportionality between intensity and W_{hkl} in equation (11) indicates that a sample of maximum total weight should be used. The limits on the total sample weight that may be used are placed by:

- 1) the fluffiness of the starting material or product.
- 2) the presence of highly absorbent elements (e.g., Pb, or Fe or Mn when using a Cu-target x-ray source) which would make a well-packed sample frame excessively absorbent.
- 3) A slightly overfull sample holder requires much more mixture handling than one slightly underfull. The amount of extra pushing of the powder may be quite variable, leading possibly to a different preferred orientation, especially if powder particles are flat or otherwise anisotropically shaped. In terms of equation (11), W_{hkl} may change as the amount of handling increases.

Thus the optimum quantitative sample is one with the maximum weight that can be easily and consistently handled, and whose x-ray opacity is unity or less. Note that for $\mu d = 1$, a single phase sample's absorption correction factor is approximately 1/3. Consequently, the optimal experimental sample will produce an intensity which is at the least one-third that of the reference sample which has zero absorption. If a sample exceeds the " $\mu d = 1$ " criterion it will inevitably require substantially

longer exposure times. Such exposure times may not be possible with the Guinier-Lenné camera. For the deWolff camera, much longer exposure times are possible. The ultimate limit is determined only by the time at which the background becomes darker than the hkl line image. Fluorescent radiation from the sample or from the partial vacuum (a typical vacuum is 10-50 millitorr) can contribute to the background, as can inelastic scattering from the sample.

In order to maintain optimal quantitative information from the x-ray films it is essential that a consistent method of storage and developing be maintained.

Method of Analysis

This section presents a general method for analyzing data obtained from Guinier-deWolff films. A schematic of this method is shown in Figure 3.

Figure 3a is a plot of film line density as a function of sample reaction time. Samples are fired at various temperatures and Guinier-deWolff films are made from these specimens. The exposure time for these films are the same as for the standard films in order to eliminate exposure time as a variable. The densitometer is used to obtain line density as a function of reaction time. Figure 3b shows a graph of the film's hkl line density as a function of weight fraction of product phase present in a material. This graph is obtained by making standards with known weight fractions of second phase present. Guinier-deWolff films are made by irradiating the standards for a fixed period of time at constant milliamperage and voltage. The microdensitometer is employed to determine the relative line densities of the films for the various weight fractions.

The graph in Figure 3c is obtained from one of the kinetic reaction models presented in the literature, as discussed above. The equations describing these models usually relate $K't$ to α , where K' is the reaction rate constant and α is the percent of reaction that has been completed. The tables relating $K't$, α

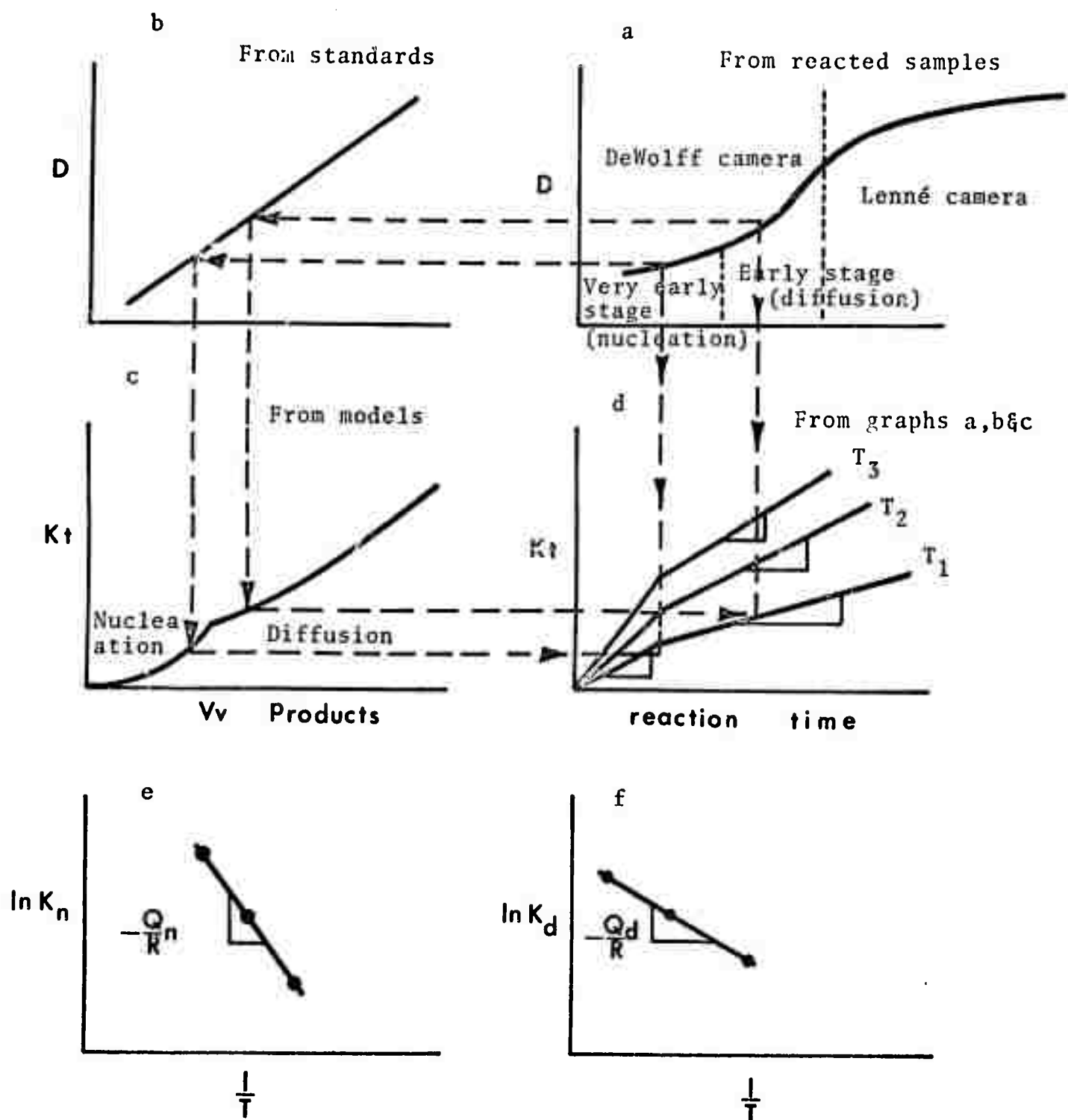


Figure 3. Analysis scheme for Guinier camera film-microdensitometer data.

and weight fraction values for various models are easily generated by computer.

The graph in Figure 3d is obtained from graphs a, b and c. The times for Figure 3d are taken directly from Figure 3a. The experimental photographic densities for the product phase are compared with those of the "standards" curve, Figure 3b. The weight fractions inferred are converted to $K't$ values in Figure 3c. These $K't$ values are used as the ordinate values in Figure 3d. For this procedure, we have been considering samples run at one temperature, for the times which are on the abscissa of Figures 3a and 3d. The additional lines in Figure 3d correspond to data obtained at the first and two additional temperatures. The slope of each line gives the reaction rate constant, K' , for the particular temperature.

Figures 3e and 3f are graphs of $\ln K'$ versus reciprocal temperature. Figure 3e will be applicable for the early stage reaction kinetics in which nucleation and surface diffusion may be rate controlling. Figure 3f is characteristic of analyses of later-stage reaction kinetics where diffusion is rate controlling. The respective activation energies are obtained from the slopes of these graphs.

The method outlined in Figure 3 can be used for analyzing the Guinier-Lenné films once the density values for the standards in this camera are obtained. The values of the line densities are plotted against the weight fraction of the second phase to obtain a standard curve. The densities of the hkl line for various reaction times from high temperature isothermal runs on unknowns are obtained in the same manner. The empirical correction for hkl line density as a function of sample temperature is then made as shown in the next section.

The zero time of reaction is found by tracing across a reactant line at various points near the beginning of the reaction. The point at which this line density becomes zero over background is the zero of reaction time. The Vernier scale on the densitometer allows the distance corresponding to a given reaction time to be accurately determined. By knowing the film

speed during the time of exposure and the distance the film has moved, the reaction time for a given density can be determined.

These methods have been used successfully to determine powder compact reaction kinetics of equimolar $\text{NiO-Al}_2\text{O}_3$ mixtures. The results will be published in a future paper.

High Temperature Modification of the Valensi-Carter Equation

A high temperature modification of the mass density of materials must be employed when the Valensi-Carter equation is used to express high temperature data collected in the Guinier-Lonné camera. Recall that the Valensi-Carter model pictures a sphere of one of the reactants being consumed by the product. Thus, the volume change on formation of product (the Δ factor) is the one which exists at the reaction temperature. Using room temperature values for density of reactants and products to calculate Δ is therefore inaccurate when using data from the Guinier-Lonné camera. This factor may be accommodated in the Valensi-Carter equation by considering that Δ is a function of temperature such that

$$\Delta_{ht} = \frac{\Delta_{rt} [1 + 3\alpha_B(T)(T^\circ\text{K} - 300^\circ\text{K})]}{[1 + 3\alpha_A(T)(T^\circ\text{K} - 300^\circ\text{K})]} \quad (14)$$

where Δ_{ht} = fractional volume change between reactant A and product B at the reaction temperature,

Δ_{rt} = fractional volume change between reactant A and product B at room temperature,

α_A = mean coefficient of thermal expansion for reactant A over the range 300°K to $T^\circ\text{K}$, and

α_B = same for the product phase.

Thus for an in-situ high temperature analysis equation (15) must be used.

$$K't = \frac{\Delta_{ht}}{\Delta_{ht}-1} - (1-\alpha)^{2/3} - \frac{1}{\Delta_{ht}-1} [1+(\Delta_{ht}-1)\alpha]^{2/3} \quad (15)$$

The potential error associated with the Δ_{ht} effect can be important when K' is evaluated at small percentages of reaction. Table I shows the dependence of the Δ_{ht} effect on percent completion and magnitude of Δ_{ht}/Δ_{rt} . The calculation of Table I was based on the formation of nickel aluminate from the component oxides where $\Delta_{rt} = 1.75$. This table applies, of course, for deviations from Δ_{ht} for any reason, including use of imprecise molecular weights and/or densities.

At 1200°C, for the above reaction, Δ_{ht} is 0.4% greater than Δ_{rt} , so the first column in the table applies. It is apparent that only a small effect is observed for the nickel aluminate system. For other reactions with approximately this Δ_{rt} value, thermal expansion may cause Δ_{ht} to be as much as 8% greater than Δ_{rt} . Several ranges of deviations, expressed as $\pm 100[(\Delta_{ht}/\Delta_{rt}) - 1]$, are the column heads of Table I, and five percentages of reaction completion are the row headings. The body of the table shows, in the upper left of each block, the percentage error from the true value of K' , and the corresponding percentage-of-full-scale error in the lower right. The tabulation shows that when the Δ_{ht} deviations become large, the error becomes quite noticeable at large percentages of reaction completion.

Comparison of Standard X-ray Techniques With the Guinier Camera

A comparison of the sensitivity of conventional quantitative x-ray techniques was performed using $\text{NiO-Al}_2\text{O}_3\text{-NiAl}_2\text{O}_4$ powder mixtures. The purpose of this experiment was to compare the limits of detection of various x-ray systems with those of the Guinier cameras. Standard mixes of NiAl_2O_4 in equimolar $\text{NiO-Al}_2\text{O}_3$ powders were used for these studies. The samples examined with an x-ray goniometer were prepared in the following manner: 0.2 gram standard mixes were spread evenly over the flat surface of a 1.5 cm diameter silicon wafer. The purpose of the wafer was to eliminate amorphous scattering from the sample holder that would add to background intensity and

Table I

Error in K't Values

"% of K't value/% of full scale"

due to deviation of Δ_{ht} from Δ_{rt}

for NiAl_2O_4 formation, $\Delta_{rt} = 1.75$

| % of Reaction | ± 0.4 | 1.0 | 2.0 | 4.0 | 8.0 | 15.0 | Nominal K't values |
|---------------|---------------|---------|----------|-----------|-----------|-----------|-----------------------|
| 3 | $\pm .39/0^*$ | .97/0* | 1.92/0* | 3.76/0* | 7.24/0* | 12.74/.01 | 1.76×10^{-4} |
| 10 | .37/0* | .92/0* | 1.81/.01 | 3.56/.02 | 6.85/.04 | 12.07/.07 | 1.97×10^{-3} |
| 40 | .29/.02 | .72/.06 | 1.42/.12 | 2.80/.24 | 5.39/.48 | 9.51/.89 | 3.38×10^{-2} |
| 70 | .22/.06 | .54/.16 | 1.07/.32 | 2.10/.64 | 4.07/1.26 | 7.19/2.30 | 1.19×10^{-1} |
| 97 | .14/.11 | .35/.27 | .69/.55 | 1.35/1.08 | 2.62/2.13 | 4.66/3.88 | 3.17×10^{-1} |

*0% means $< 5 \times 10^{-3}\%$.

Legend: A/B A = percentage error from true value of K't due to Δ_{ht} effect.
 B = percentage of full scale error due to Δ_{ht} effect.

thus make peaks from small weight percentages of NiAl_2O_4 difficult to detect. The 400 NiAl_2O_4 diffraction beam was used for the analysis of all diffraction studies. The scattering ability of this plane is approximately three-fourths that of the highest intensity scattering plane in NiAl_2O_4 which could not be used because it is covered by a NiO line. The second phase was considered detected when a peak 0.3 inch higher than the highest peak of the background appeared at the Bragg angle for the peak. For quantitative analysis an intensity approximately twice this value is desired.

A standard Philips diffractometer with a copper x-ray tube was the first technique to be investigated. This arrangement featured a graphite diffracted beam monochromator mounted in front of a proportional counter. The monochromator reduces the background and sample fluorescent intensity that reaches the detector. Using unfiltered white radiation, the smallest quantity of NiAl_2O_4 that could be detected was 1.0 weight percent, as shown in Table II. Using this same arrangement with a nickel filter mounted in front of the receiving slits, the detection limit was improved to 0.7 weight percent NiAl_2O_4 . Quantitative analysis was possible at 5-7 weight percent NiAl_2O_4 .

Another technique using a LiF main beam monochromator crystal to focus the copper radiation onto the sample was employed. This method also involved a goniometer arrangement. The focused x-ray beam should eliminate white radiation background and enhance the x-ray intensity reaching the sample and the argon proportional counter. As shown in Table II the limit of detection for this technique is no improvement over the other diffractometer methods.

The Debye-Scherrer method using a 57.3 mm (small) camera was investigated, also. Using a copper x-ray tube and nickel filter, the 400 diffraction line of NiAl_2O_4 from a 3.0 weight percent mixture was visible on the film after a 45-minute exposure. The same line for a 1.0 weight percent mixture was not visible after a 1.5-hour exposure. Longer exposure times were not feasible because background radiation from air

Table II
Detection Limits of Various X-ray Apparatus

| Apparatus | Features | Detection Limits | μd of NiAl ₂ O ₄ in Sample |
|------------------------|--|---|--|
| Debye-Scherrer Camera | Nickel main beam filter, 57.3 mm diameter. | 2+ wt.% of NiAl ₂ O ₄ in an equimolar mix of NiO-Al ₂ O ₃ | .01+ |
| Diffractometer | White radiation, graphite diffracted beam monochromator. | 1+ percent | .005+ |
| Diffractometer | Nickel diffracted beam filter, graphite diffracted beam monochromator. | 0.7 percent | .003 |
| Diffractometer | LiF main beam monochromator. | 0.8 percent | .004 |
| Guinier-Lenné Camera | Quartz main beam monochromator, one-half of diffraction path evacuated; high temperature furnace. | 0.30 percent | .0014 |
| Guinier-deWolff Camera | Quartz main beam monochromator, evacuated diffraction chamber, four samples simultaneously. | 0.030 percent | .00014 |

scattering darkened the film and covered the 400 diffraction line image.

Table II also shows the detection limits determined for the Guinier cameras. The criterion for "detection only" was visual detection of a faint line at the position where the 400 line appears. Illumination was with a soft, somewhat dimmed fluorescent lamp from behind the film. Line position was confirmed with the direct reader supplied with the camera. A sample of 42 mg/cm^2 , for a total x-ray opacity of 0.46, was used for all Guinier camera samples. The fluffiness of the Linde A Al_2O_3 powder prevented using more material. This sample density corresponds to 20 mg for the Lenné camera sample frame and 30 mg for the deWolff camera. Cu K_α x-radiation with Kodak No-Screen was used with operating conditions of 40 KV and 20 ma.

For quantitative analysis of second phases it is necessary to take a microdensitometer reading of the diffraction line. The sensitivity of the instrumental reading is less than that of the human eye and therefore the detection limits for semi-quantitative and quantitative analyses are a larger weight percent of second phase, as shown in Table III. The microdensitometer gave signal-to-noise amplitude ratios of less than approximately 1.5/1 for the Detect Only figures. The criterion for "Semiquantitative Analysis" was signal-to-noise ratios between 2-5. Films showing ratios of 5 or greater were judged suitable for quantitative analysis.

The results shown in Table III show that the Guinier-deWolff camera offers only a factor of about six improvement in detection level for quantitative analysis over the best diffractometer methods. However, over a factor of 30 increase in sensitivity for second phase detection without the use of the microdensitometer is obtained. Thus, the major attraction of the Guinier-deWolff camera is for qualitative detection of second phases. It is suitable for quantitative early-stage kinetic studies only with sufficient care in operation.

Table III

Resolution Times for the Guinier-deWolff Camera.
Kodak No-Screen Film; Cu K_{α} x-rays; 40 kv, 20 ma

| Function | Wt. % NiAl_2O_4 in $\text{NiO-Al}_2\text{O}_3$ Mix | | | | | |
|----------------------------|--|---------|---------|---------|--------|--------------|
| | .03 | .10 | .30 | 1. | 3. | 10 & greater |
| Detect Only | 18 hrs. | 12 hrs. | 8 hrs. | 6 hrs. | 1 hr. | <1 hr. |
| Semi-quantitative analysis | never | never | 36 hrs. | 12 hrs. | 3 hrs. | <1 hr. |
| Quantitative analysis | never | never | never | 24 hrs. | 6 hrs. | 1 hr. |

The Guinier-Lenné camera also exhibits a factor of two increase in sensitivity in second phase detection, in addition to its important advantage of in-situ reaction analysis. Analytical criteria for Guinier-Lenné camera films are the same as for Guinier-deWolff films.

Summary

It is demonstrated that conventional methods of analyzing kinetics data are inadequate for early-stage reactions. A method for graphical determination of reaction rate constants is proposed, from which experimental activation energies for both early-stage and later-stage reactions can be obtained. With the aid of a Guinier-deWolff camera, one can study the early-stage reactions (<3%) involving nucleation, surface diffusion and other phase boundary reactions.

The Guinier-Lenné camera is useful for performing in-situ analyses of solid state reactions when the high temperature modification of the Valensi-Carter equation is employed.

Thus, a complete and precise kinetics analysis is possible with the joint use of the Guinier-deWolff and Guinier-Lenné cameras.

References

1. F. S. Pettit, E. H. Randklev and E. J. Felten, "Formation of NiAl_2O_4 by Solid State Reaction," J. Amer. Ceram. Soc., 49 [4], 199-203 (1966).
2. R. E. Carter, "Mechanism of Solid State Reaction Between Magnesium Oxide and Aluminum Oxide and Between Magnesium Oxide and Ferric Oxide," J. Amer. Ceram. Soc., 44 [3], 116-210 (1961).
3. D. L. Branson, "Kinetics and Mechanism of the Reaction Between Zinc Oxide and Aluminum Oxide," J. Amer. Ceram. Soc., 48 [11], 591-595 (1965).
4. H. Kedesdy and A. Drukalsky, "X-ray Diffraction Studies of the Solid State Reaction in the NiO-ZnO System," J. Am. Chem. Soc., 76, 5941-5946 (1954).
5. M. Hirota, "X-ray Studies on the Reaction Product Formed in the Metallized Layer-Ceramic Interface of Metal-to-Ceramic Seal," Trans. JIM, 9 [4], 267-272 (1968).
6. J. F. Duncan, K. J. D. Mackenzie and P. K. Foster, "Kinetics and Mechanisms of High Temperature Reactions of Kaolinite Minerals," J. Amer. Ceram. Soc., 52 [2], 74-77 (1969).
7. W. Jander, "Reactions in Solid State at High Temperature, I," Z. Anorg. Allgem. Chem., 163 [1-2], 1-30 (1927).
8. G. Valensi, "Kinetics of the Oxidation of Metallic Spherules and Powders," Compt. Rend., 202 [4], 309-312 (1936).
9. R. E. Carter, "Kinetics Model for Solid State Reactions," J. Chem. Phys., 34 [6], 2010-2015 (1961).
10. F. J. Duncan and D. J. Stewart, "Kinetics and Mechanisms of Formation of Zinc Ferrite," Trans. Faraday Soc., 63 [4], 1031-1041 (1967).
11. P. M. deWolff, "Multiple Guinier Cameras," Acta Cryst., 1, 207-211 (1948).
12. Kodak X-ray Film Catalog, 1971 edition, Rochester, New York.
13. W. H. Sas and P. M. deWolff, "Intensity Corrections for the Guinier Camera," Acta Cryst., 21, 826-827 (1966).

B. A CORRELATION OF THE SHORT RANGE ORDER IN Ni_3Fe WITH CERTAIN PHYSICAL PROPERTIES OF THIS ALLOY (W. L. Wilson and R. W. Gould)

Introduction

The existence of atomic order in alloys near the composition Ni_3Fe was first proposed by Dahl (1936), in a study of the effects of cold work and heat treatment on Ni-Fe alloys. Later x-ray diffraction studies by Leech and Sykes (1939) confirmed the formation of an ordered structure of the Cu_3Au type upon annealing below 500°C . Several more recent investigations have shown a strong correlation between the amount of order present in the system and various physical properties. Examples of these studies are the calorimetric work by Iida (1952, 1954, 1955), the mechanical property studies by Vidoz, Lazaveric, and Cahn (1963), and the magnetic studies by Bozorth (1953). In each of these studies, a strong correlation between atomic order and physical properties has been shown.

While x-ray scattering measurements provide the most complete information concerning atomic order in an alloy, the x-ray data on this system have been quite sparse, especially during the early stages of the order reaction. This lack of data is mainly attributable to the extremely low levels of order-modulated intensity obtained from alloys of this system. The reason for these low intensity levels is found in the equation given by Cowley (1950), which may be written for the cubic case as:

$$I(h_1, h_2, h_3) = \sum_{\ell} \sum_m \sum_n N X_A X_B (f_A - f_B)^2 \alpha_{\ell mn} \cos 2\pi h_1 \ell \cos 2\pi h_2 m \cos 2\pi h_3 n \quad [1]$$

order

In this equation, X_A and X_B are the atomic fractions and f_A and f_B are the atomic scattering factors of A and B, respectively,

$k = 2\pi(S-S_0)/\lambda$, and ℓ , m , and n are related to the interatomic vector $R_{\ell mn} = \ell a_1/2 + m a_2/2 + n a_3/2$ (a_i = normal crystal axes). The quantities h_1 , h_2 , and h_3 are continuous variables in the reciprocal lattice. The term $\alpha_{\ell mn}$ is the short range order parameter, and is defined as:

$$\alpha_{\ell mn} = 1 - p_{\ell mn}^{BA}/X_B$$

where $p_{\ell mn}^{BA}$ is the conditional probability of finding an atom of Type B at a site $\vec{R}_{\ell mn}$ from an origin A atom. From Eq. 1, it can be seen that elements whose atomic scattering factors are similar will produce low levels of order modulated intensity since the term $(f_A - f_B)^2$ will be small. One means of overcoming this problem is the use of the anomalies in the scattering factors of Ni and Fe which occur when using CoK α . Using the values of the dispersion corrections for CoK α radiation for Ni and Fe given by Cooper (1963), the value of this term was found to be approximately double that found with copper radiation. An additional gain in intensity was obtained by using a pyrolytic graphite primary beam monochromator. Renninger (1954) has shown that a natural graphite monochromator could yield as much as a 600% increase in diffracted intensity over a LiF crystal, and later work by Gould, Bates, and Sparks (1968) showed that a flat crystal of pyrolytic graphite showed a 300% intensity increase over LiF in the same wavelength range. With the combination of the Co radiation and graphite monochromator, the intensity of the diffuse scattering was brought to a measureable level.

Experimental

The short range order α parameters were obtained by determining the distribution of diffuse x-ray intensity from a single crystal of Ni₃Fe and performing the Fourier transform of Eq. 1. In terms of the fcc Ni₃Fe structure this becomes:

$$\alpha_{\ell mn} = \frac{1}{\sum_{h_1=0}} \frac{1}{\sum_{h_2=0}} \frac{1}{\sum_{h_3=0}} \frac{I(h_1, h_2, h_3)}{N X_A X_B (f_A - f_B)^2} \cos 2\pi h_1 \ell \cos 2\pi h_2 m \cos 2\pi h_3 n \quad [2]$$

The mapping of the intensity distribution throughout the entire first cell of the reciprocal lattice would require enormous amounts of time. However, symmetry elements in the intensity distribution allow a much smaller volume to be measured, with the resultant intensities reflected to fill the first cell. The minimum volume of measurement necessary for the fcc case as given by Sparks and Borie (1965) is shown in Fig. 1.

The intensity distribution within this tetrahedral volume was obtained by using a General Electric Single Crystal Orienter in conjunction with a modified G.E. XRD-5 diffractometer. Since the equipment available allowed only one drive (2θ) to be automated, it was decided to collect data on a series of planar areas lying within the volume studied. This data was then extrapolated by digital computer methods onto a cubic subgrid of points within this volume.

Conversion of diffuse intensity into absolute units was done using polystyrene according to Sparks and Borie (1965)¹¹. In the final computer calculation, the corrected diffuse x-ray intensities, divided by the Laue monotonic unit $X_A X_B (f_A - f_B)^2$, were reflected through symmetry relationships to fill the first cell of the reciprocal lattice and Eq. 2 was integrated using a three-dimensional Simpson's rule method. These calculations resulted in the short range order α parameters characteristic of the state of order¹¹.

The reliability of the three-dimensional interpolation and intensity reflection routines was tested by calculating a series of α parameters from an assumed model of short range order and synthesizing intensity data at the points to be measured, using Eq. 1. This synthesized intensity data was then processed through the computer programs and the resulting α 's compared to the input values. This test resulted in the α 's agreeing within 3%, the major cause of error being the small number of input α 's and the rapidly forced termination of the intensity series.

The effects of temperature diffuse scattering were not included in the calculation of the α parameters in this study. The value of the diffuse intensity around the Bragg nodes, where the

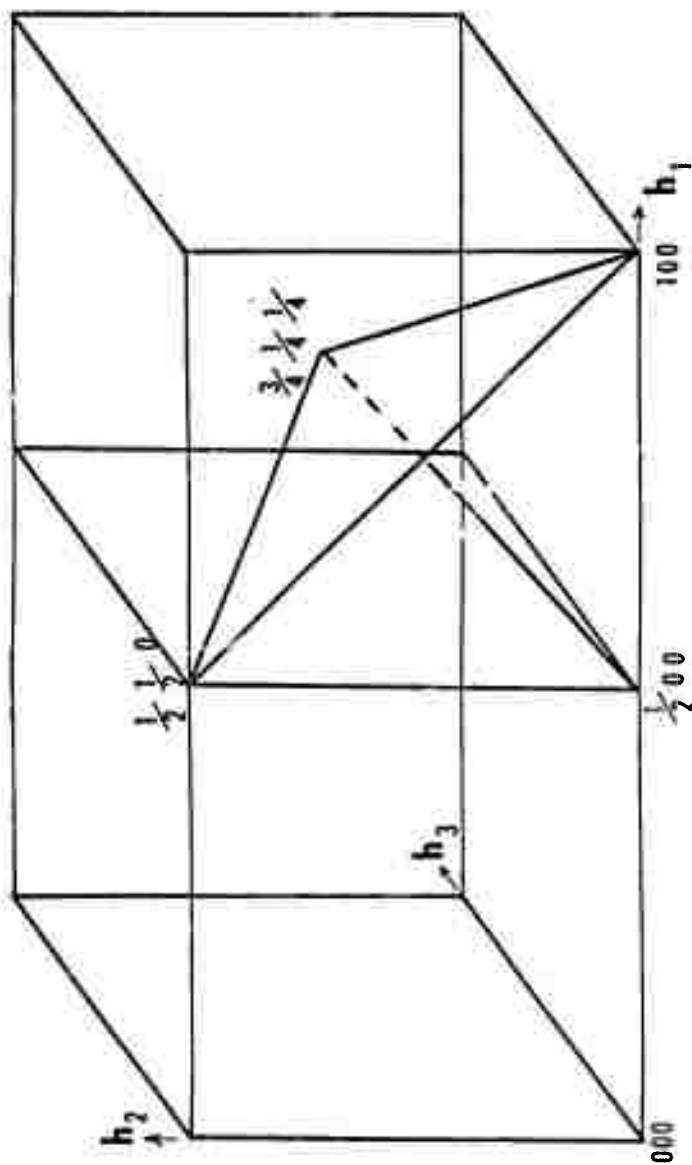


Fig. 1: The reciprocal lattice construction showing the tetrahedral volume bounded by the points $(h_1, h_2, h_3) = (1/2, 0, 0)$, $(1/2, 1/2, 0)$, $(3/4, 1/4, 1/4)$, and $(1, 0, 0)$, which contains the sufficient intensity data to obtain the S.R.O. α parameters.

TDS is concentrated, was extrapolated to zero at the nodes. The size effect including Huang scattering were also neglected. The similarity in atomic size and chemical behavior for Ni and Fe, along with the absence of a peak shift at the (100) and (110) positions, suggested that the size effect was minimal.

The x-ray measurements and diamond pyramid microhardness measurements were made on the same single crystal sample. This sample consisted of a disc approximately 1" diam. X 1/16" thick, cut to a (211) orientation. Analysis in our laboratory showed the composition to be 74/26 Ni/Fe. Measurements of the electrical resistivity and magnetic coercive force were performed on polycrystalline wires of composition 75.15% Ni, balance Fe. Both of these tests were performed by the standard methods for wire specimens at room temperature. For both the single crystal and polycrystalline samples, annealing was carried out in vacuo at a temperature of 480°C, approximately 10°C below the critical ordering temperature, for varying amounts of time.

Results and Discussion

Following the procedures outlined above, x-ray and microhardness data were taken for the single crystal sample as quenched from 1000°C and at annealing times of 20 min. to 40 hours at 480°C. The values of the α parameters for the first several co-ordination shells as a function of annealing time at 480°C are shown in Fig. 2, along with the values for the perfectly ordered structure.

In the present work, it was found that an error of less than one count per second in the measured background intensity could change the value of α_{000} from greater than 1.5 to 1.0, while the other α 's were scarcely effected.

Referring again to Fig. 2, one should note that for annealing times up to 8 hours at 480°C, there are several discrepancies in the signs of some of the α 's as compared to perfect order. This effect has been found by Cowley (1950) in his work on Cu_3Au , and has been discussed as showing the order relationships to hold for the most part only over nearest neighbor distances. The er-

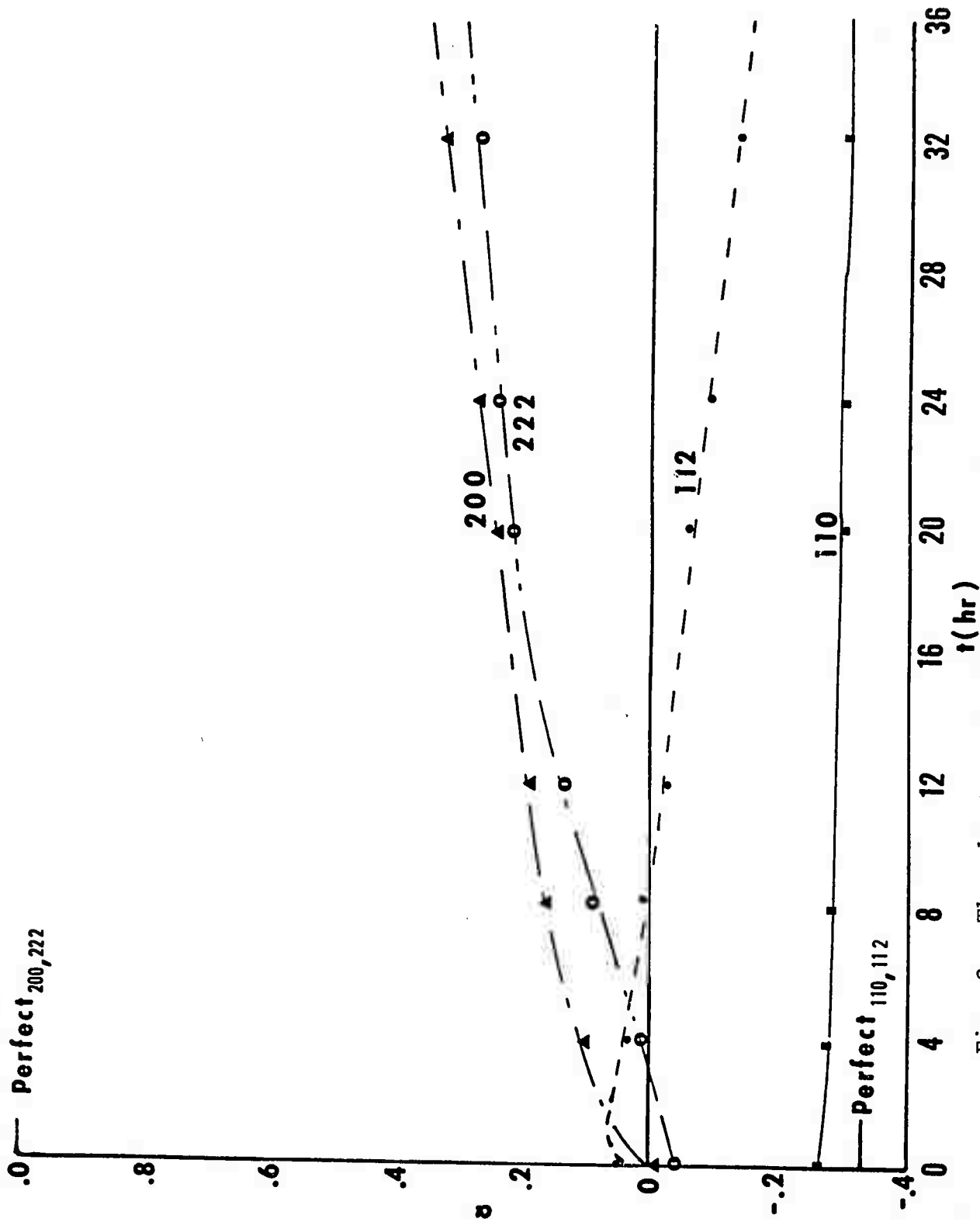


Fig. 2: The short range order α parameters for $\ell_{mn} = 110, 200, 112$, and 222 as a function of annealing time at 480°C . Note the "wrong" signs for α_{112} and α_{222} during the early stages of the annealing.

ror in sign stems from the tendency for each atom to surround itself by unlike nearest neighbors during the early stages of order, a pattern which is not entirely compatible with the fcc Cu_3Au type structure. At times greater than 12 hours, the signs of the α 's can be seen to progress toward those found in the long range ordered structure, although their magnitudes show that the arrangement is still far from perfect order.

The results of the microhardness, electrical resistivity, and coercive force measurements also show a change to take place at roughly 12 hours of annealing. This is shown in Fig. 3. The rate of change of hardness with time, although the least sensitive of the measurements performed, shows a definite break to occur between 10-14 hours of annealing. In a similar manner, the rate of change of resistivity with time shows a major change during this time period. The coercive force data show that the coercivity decreases with time upon annealing at 480°C for times up to 12 hours. After reaching a minimum value at this time, the coercivity then increases with further annealing.

The change in the ordered structure from one dominated by nearest neighbor interactions to one with longer range correlations shows an excellent correlation with the proposed sequence of ordering given by Iida (1955). Based upon his calorimetric data, he proposed that the period of annealing from the quenched state up to approximately 10 hours produced a short range ordered structure, with a small amount of long range order. The period lasting from 5-60 hours of annealing was proposed to include the formation of the long range ordered structure. This would seem to agree quite well with the explanation of the signs of the α 's given earlier.

Conclusions

Through the use of x-ray diffuse scattering methods, the local atomic arrangements during the early stages of the order reaction in Ni_3Fe have been quantitatively determined. These data have shown that for annealing periods less than 12 hours at

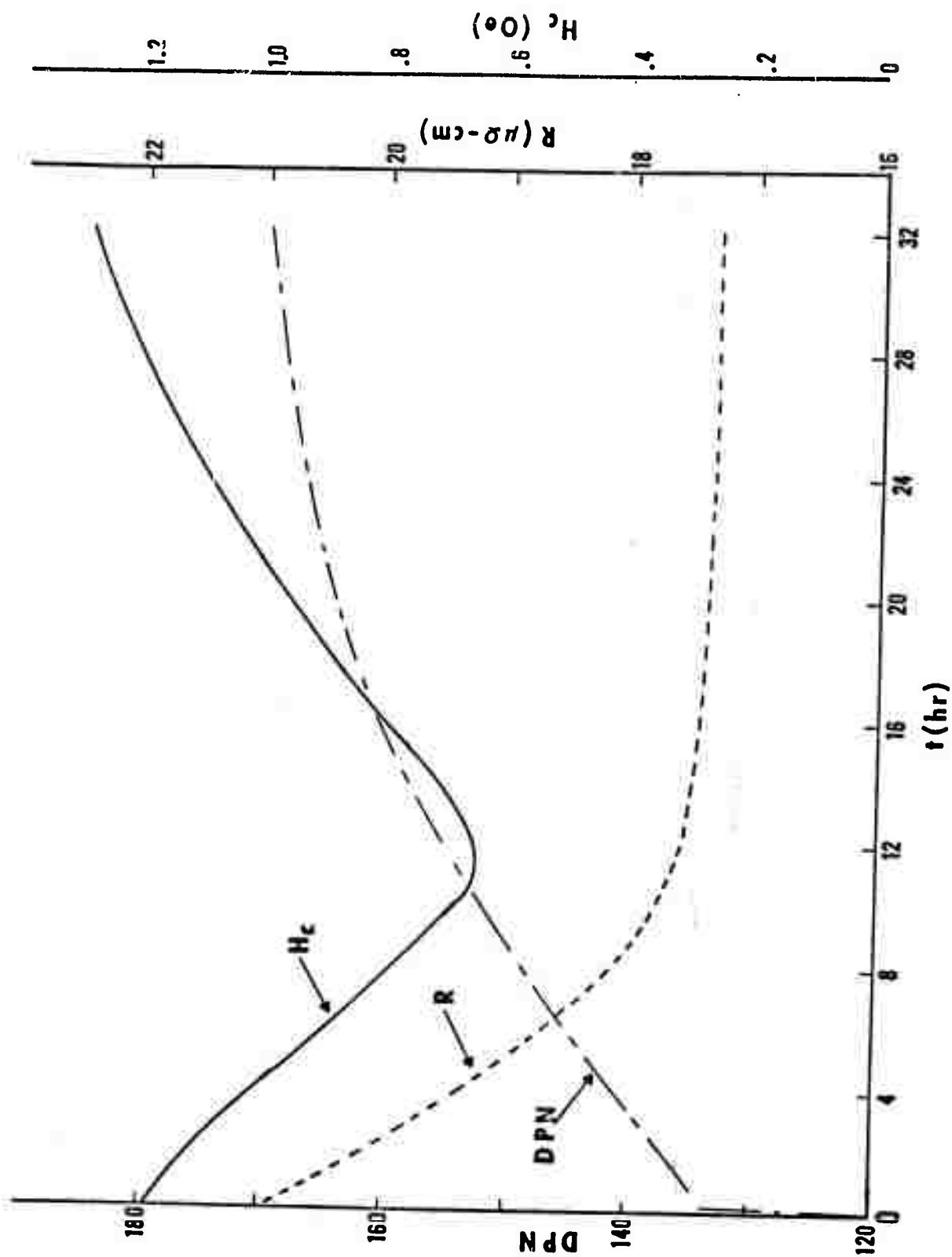


Fig. 3: The values of the microhardness, resistivity, and coercive force as a function of annealing time at 480°C.

480°C, the nearest-neighbor interactions dominate the distribution of the atoms on the lattice sites. For longer times of annealing, this gradually changes to a more cooperative interaction extending over longer distances and approaching the arrangement found in the fully ordered structure.

The changes in the hardness, resistivity, and coercive force which occur at or near 12 hours of annealing support the contention that a change in the type of atomic arrangement is taking place at this time.

REFERENCES

1. Bozorth, R. M., (1953), Rev. Mod. Phys., 25, 42.
2. Cooper, M. J., (1963), Acta. Cryst. 16, 1067.
3. Cowley, J. M., (1950), J. Appl. Phys., 21, 24.
4. Dahl, O., (1936), Z. fur Metall., 28, 133.
5. Gould, R. W., Bates, S. R. and Sparks, C. J., (1968), Appl. Spect., 22, 549.
6. Iida, S., (1952), J. Phys. Soc. Japan, 7, 373.
7. Iida, S., (1954), J. Phys. Soc. Japan, 9, 346.
8. Iida, S., (1955), J. Phys. Soc. Japan, 10, 9.
9. Leech, P. and Sykes, E., (1939), Phil. Mag., 27, 742.
10. Renninger, M., (1954), Acta. Cryst., 7, 677.
11. Sparks, C. J. and Borie, B., (1965), Local Atomic Arrangements Studied by X-Ray Diffraction, (Gordon and Breach Science Publishers, New York).
12. Vidoz, A. E., Lazaveric, D. P. and Cahn, R. S., (1963), Acta. Met., 11, 17.

IV. Discussion

The research of this ninth semi-annual period has provided technical findings that bear on problems of interest to the Department of Defense. Moreover, from this research have come foundations undergirding our future studies.

Two sections of this report (II-B and C) deal directly with devices for photodetection; a third section (II-D) deals with fundamental properties exhibited by germanium doped with nickel, which provides information of potential use in the design of photodetection and other devices which find wide employment in military applications. To place into perspective the properties of our new type of photodiode, we note that the fast response time, high responsivity, flat spectral response between 0.4 and 1.0 microns, and low noise performance reported here apply to a device whose design has yet to be optimized. Work toward optimization progresses, together with studies seeking a fuller understanding of the details of the observed behavior.

MOS transistors will likely form the heart of many military electronic systems of the future, and their current-voltage behavior and noise properties need to be understood for proper application. Here we have described certain aspects of their performance resulting from avalanche multiplication. Additional related studies are now in progress. One study seeks a more detailed understanding of the noise behavior attending avalanche multiplication in semiconductor devices. Another will describe the alteration in the noise performance of junction field-effect transistors after exposure to an irradiation environment.

Properties exhibited by amorphous semiconductors make them potentially useful in a variety of applications that may involve exposure to radiation. In this report we have described certain basic experiments that lend an understanding of the behavior of these materials. Our future effort will concentrate on determining the radiation sensitivity exhibited by amorphous semiconductors and on assessing the ultimate limitations and promise of these materials in device applications.